DOSIMETRY OF IRREGULAR FIELD SIZES IN ELECTRON BEAM THERAPY

by

Denise Lambert
Department of Medical Physics
McGill University, Montreal
May 2001

A Thesis submitted to the
Faculty of Graduate Studies and Research
in partial fulfillment of the requirements for the degree of
Master of Science

0-612-70446-7

ABSTRACT

Electron beams are used to treat superficial lesions in radiation oncology by taking advantage of the sharp dose fall-off and the limited range of the particles in tissue. The irregular shape of individual tumors, however, often requires custom made shielding in order to geometrically shape the radiation field to the target, while minimizing the dose to surrounding tissues. In many institutions, low melting alloy or lead cutouts are used for electron beam shaping. In this work, electron dosimetry beam parameters such as percentage depth dose (PDD), outputs, and beam profiles, were measured with ten different electron beams from two linear accelerators. The dependence of beam characteristics on field size and shape, particularly for small cutouts, was investigated. In addition, this project examined different methods for measuring electron PDDs, including film densitometry, ion chambers, and diode dosimetry.

The work presented here demonstrates that the depth dose effect is significant when one of the field dimensions of the cutout is less than R_p, the practical range of electrons. For these cutouts, it was observed that both PDD and outputs vary significantly due to the lack of lateral electronic equilibrium. As the cutout becomes smaller, the depth of dose maximum (d_{max}) shifts towards the surface, while the output at d_{max} decreases. Therefore, it is crucial that PDDs and outputs are either measured or calculated for small field electron cutouts used in the clinical setting.

RÉSUMÉ

Les faisceaux d'électrons sont utilisés pour traiter les lésions superficielles en radio-oncologie, puisqu'ils prennent avantage de la chute abrupte de la dose et de la portée limitée de ces particules dans le tissu humain. La forme irrégulière des tumeurs individuelles, par contre, nécessite souvent une délimitation de champ faite sur mesure afin de modeler géométriquement le champ d'irradiation à la tumeur, tout en minimisant la dose aux tissus voisins. Dans plusieurs institutions, le modelage du faisceau d'électrons est réalisé à l'aide de plaques fabriquées au plomb au à l'aide d'un alliage au faible point de fusion. Dans le cadre de ce travail, les paramètres de la dosimétrie des faisceaux d'électrons, tels que le rendement en profondeur (PDD), le débit de dose et le profil du faisceau, ont été mesurés pour dix faisceaux différents d'électrons, provenant de deux accélérateurs linéaires. La dépendance des caractéristiques du faisceau sur la taille et la forme du champ, particulièrement pour les petits découpages, a été étudiée. De plus, ce projet a examiné différentes méthodes pour mesurer les rendements en profondeur des électrons, incluant la densitométrie de films radiologiques, les chambres d'ionisation et la dosimétrie par diode.

Le travail présenté ici démontre que l'effet sur la dose en profondeur est significatif quand l'une des dimensions du champ découpé est inférieure à R_P, la portée pratique des électrons. Pour ces découpages, il a été observé que le rendement en profondeur ainsi que le débit de dose varient significativement, dû à l'absence d'équilibre électronique latéral. Au fur et à mesure que le découpage devient plus petit, la profondeur de dose maximale (d_{max}) se déplace vers la surface, alors que le débit de dose à d_{max} diminue. Ainsi, il est crucial que les rendements en profondeur et les débits de dose soient mesurés ou calculés pour les petits découpages de champs d'électrons utilisés en clinique.

ACKNOWLEDGEMENTS

I would like to thank Dr. Ervin Podgorsak for his understanding of my particular circumstance and for granting me financial support from McGill University. I would also like to extend my sincere gratitude to my supervisors, Michael D.C. Evans and Marina Olivares. Many thanks to Michael for his continuous encouragement, endless patience, and invaluable guidance. This thesis would not have been possible without Marina, who initiated this study and advised me on numerous occasions.

My appreciation to Marylene Brodeur for translating the abstract to French and Shoukry Aboulehaf for constructing the cerrobend cutouts. I would also like to thank Joe Larkin and Pierre Léger for their prompt assistance when the linac malfunctioned.

Finally, I would like to thank my family for their continuous love and support. This thesis is dedicated to my husband, Michael, who has always inspired and encouraged me, and was instrumental in its completion.

TABLE OF CONTENT

CHAPTER 1: INTRODUCTION TO MODERN RADIOTHERAPY

1.1 *Introduction to cancer treatment*

In 1997, cancer was the second leading cause of death in the United States, accounting for one quarter of all deaths[1]. Moreover, it was also the leading cause of death for Americans aged 45-74. Surgery, chemotherapy, and radiotherapy are the main modalities for treating cancer, and about 50% - 60% of cancer patients in the United States are either treated with radiation therapy alone, or with radiotherapy in conjunction with surgery[2]. Approximately half of all radiotherapy patients are treated with curative intent; whereas the other half are treated for palliation, which is the relief or prevention of specific symptoms[3]. There are two types of radiation therapy: brachytherapy and external beam therapy. Brachytherapy is a method of treatment whereby sealed radioactive sources are placed in close proximity to the tumor, either by interstitial, intracavitary, intraluminal or surface application[4]. On the other hand, external beam therapy delivers a dose of therapeutic radiation at a distance from the tumor, usually at 1 m. The most common devices used for external beam therapy are the Cobalt-60 unit and the linear accelerator (linac). The Cobalt- 60 machine is the only remaining radioisotope machine currently used routinely. Initially, ^{60}Co decays to $^{60}Ni^*$, then two γ-rays of energies 1.17 MeV and 1.33 MeV are emitted as $^{60}Ni^*$ decays to ^{60}Ni. Linacs are megavoltage radiotherapy machines that produce x-ray and electron beams of varying energies. The x-ray beam is produced by impinging the electron beam onto the x-ray target. The radiative losses (bremsstrahlung) in the target resulting from electron-nucleus interactions produce the high-energy photon beam. The forward peaked x-ray beam is not useful in radiotherapy, and must be made clinically acceptable using a flattening filter. On the other hand, a pencil electron beam is produced with the x-ray target and flattening filter removed. Clinical electron beams are produced from pencil electron beams by using one of two techniques: pencil beam scattering whereby a thin scattering foil of high *Z* material (such as copper) is placed into the path of the pencil beam, or pencil beam scanning whereby two computer-controlled magnets deflect the pencil beam in two orthogonal planes[5].

1.2 Uses of cutouts in electron beam therapy

The rapid dose fall-off and the limited range of an electron beam enables the treatment of lesions close to the surface, while sparing the underlying tissues. The irregular shapes of individual tumors, however, require the need for custom-made cutouts so as to conform the shape of the radiation field to that of the tumor, while sparing radiation to surrounding tissues. Because lateral equilibrium is not achieved when the electron beam field size is very small, beam parameters, specifically PDD and outputs must be measured every time a cutout is used. This process is both time and labor intensive, therefore the purpose of this work is to provide a comprehensive set of electron beam data obtained with cutouts of different sizes and shapes under relevant clinical conditions. In addition, the goal of this study is to investigate the correlation between cutouts of different sizes and electron beam characteristics. Finally, this work also examines the minimum field size where individual measurements other than the output are no longer needed.

1.3 Thesis Organization

Chapter 2 introduces the physics of electron beam dosimetry, including topics such as the interactions of electron with matter and methods of characterizing the energy of a clinical electron beam.

Chapter 3 describes the basic operation of a linear accelerator, as well as the clinically relevant dosimetric characteristics of an electron beam.

Chapter 4 deals with different dosimetric techniques and phantoms that are used for measuring clinical electron beam data.

Chapter 5 reviews the experimental set-up and results used to compare different dosimeters such as film, ion chamber, and diode. The methods for measuring electron beam depth doses, profiles and outputs for cutouts are also discussed.

Chapter 6 summarizes the measured electron beam cutout data obtained from Chapter 5, and a discussion of the results is also presented.

Chapter 7 presents conclusions based on this work, as well as suggestions for possible future work.

Finally, a complete set of electron beam depth doses measured with all the cutouts, and a representative set of profiles are presented in the appendix.

1.4 References

1. Bureau of Vital Statistics, http://www.hss.state.ak.us/dph/bvs/bvs_home.htm.
2. C.A. Perez & L.W. Brady, Principle and practice of radiation oncology, JP Liddicoat, Philadelphia, U.S.A. (1987).
3. L.R. Coia, G.E. Hanks, K. Martz, A. Steinfield, J.J. Diamond & S. Kramer, "Practice patterns of palliative care for the United States 1984-1985", Int. J. Radiat. Oncol. Biol. Phys. 14 (1), 261-1269 (1988).
4. F.M. Khan, The Physics of Radiation Therapy, 2nd edition, Williams & Wilkins, Baltimore, Maryland, U.S.A. (1994).
5. E.B. Podgorsak, P. Metcalfe & J. Van Dyk, in Chapter 11, "Medical Accelerators," in The Modern Technology of Radiation Oncology, ed. Jacob Van Dyk (Madison: Medical Physics Publishing, 1999), 351-381.

CHAPTER 2: INTRODUCTION TO THE PHYSICS OF ELECTRON BEAM DOSIMETRY

This chapter introduces the physics of electron beam dosimetry. Topics of discussion include the interactions of the electron with matter, methods of determining various energy parameters of an electron beam, and considerations in measuring dose such as polarity and displacement corrections.

2.1 Electron interactions with matter

Electrons interact with one another, or with the nuclei of other nearby atoms that are within their Coulomb electric force fields. As a result, they may lose energy and/or scatter. Although only a very small amount of the incident particle's kinetic energy is transferred, a 1 MeV charged particle will typically undergo about 10^5 interactions before losing all of its kinetic energy[1].

There are three types of charged-particle Coulomb-force interactions: (1) soft collisions, (2) hard collisions, and (3) bremsstrahlung. The probability of each interaction depends on the classical impact parameter b and the classical atomic radius a, as shown in Fig. 2.1.

2.1.1 Soft Collisions (b >> a)

When a charged particle passes an atom with an impact parameter much greater than the atomic radius, the whole atom is influenced by the particle's Coulomb force field. The atom is sometimes excited, or it can be ionized by the ejection of a valence shell electron. From this process, a minute amount of energy, on the order of a few eV, is transferred to the atom of the medium.

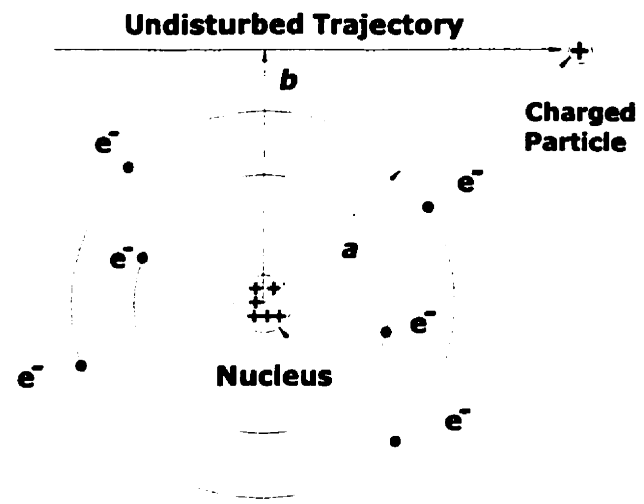

Figure 2.1: Important parameters in charged-particle collisions with atoms; *a* is the atomic radius and *b* is the impact parameter (redrawn from Attix[1]).

Soft collision is the most common type of interaction, and it accounts for about half of the energy transferred to the absorbing medium.

2.1.2 Hard collisions or "knock-on" collisions ($b \approx a$)

When the atomic radius and the impact parameter are of the same order, the incident particle will most likely interact with a single atomic electron. This atomic electron will be ejected from the atom, often with a significant amount of energy. The electron is therefore able to ionize other atoms on its own and is referred to as a delta ray. Although the number of such collisions are few compared to soft collisions, the fractions of the primary particle's energy that are spent by these two processes are generally comparable, since the energy transferred in one hard interaction is much larger than that of a soft collision.

2.1.3 Coulomb-force interactions with the external nuclear field ($b \ll a$)

The Coulomb force interaction takes place with the nucleus when the impact parameter is much smaller than the atomic radius. In about 98% of such interactions, the electron does not lose any energy by the emission of an x-ray photon or the excitation of the nucleus. Instead, it is scattered elastically, losing only its minimum energy in order to conserve momentum. The electron is deflected, although no energy is transferred. This explains the meandering path often followed by an electron, especially in a high Z media. In about 2% of the interactions, an x-ray photon is emitted by inelastic radiative interaction when the electron passes near the nucleus. The electron slows down as most of its kinetic energy (up to 100%) is transferred to the photon. These X rays are called "bremsstrahlung", from the German word for "braking radiation". Bremsstrahlung is proportional to the inverse square of the mass of the particle, and therefore it is only significant for lighter particles such as electrons.

2.2 Energy Determination

Electron energy must be determined for measurements taken with a dosimeter that requires conversion of ionization to dose (such as an ion chamber) since the stopping power is dependent on the electron energy. However, the determination of electron energy is not important for dosimeters that do not require any conversions, such as diodes. At the end of the accelerator guide, just before reaching the accelerator window, the intrinsic beam has a small spread in energy and angle. However, the spread increases quite significantly as the intrinsic electron beam passes through the exit window, scattering foil, monitor chamber, air and other materials prior to reaching the phantom surface (Fig. 2.2). Some of the important energy parameters include $E_{p,0}$, the most probable energy (kinetic) at the surface, $\bar{E}_o$, the mean energy of the electron beam at the surface of the phantom, and $\bar{E}_z$, the mean energy at a depth z in the phantom. From the central curve in Fig. 2.2, it is shown that $\bar{E}_o$, the mean energy of the electron beam at the surface of the phantom is smaller than $E_{p,0}$, the most probable energy (kinetic) at the surface. Clinically, an electron beam is usually characterized by $\bar{E}_o$. There are several methods to determine this energy: measurement of threshold energy for nuclear reactions, range measurements, and the measurement of Cerenkov radiation threshold[2]. Of these, the range method is the one most suited for a clinic due to its convenience and practicality.

2.2.1 Determination of $E_{p,0}$

$E_{p,0}$ (MeV) is related to the practical range, R_p (cm), in water by the following relationship (R_p is defined on pg. 23):

$$E_{p,0} = C_1 + C_2R_p + C_3R_p^2. \tag{2.1}$$

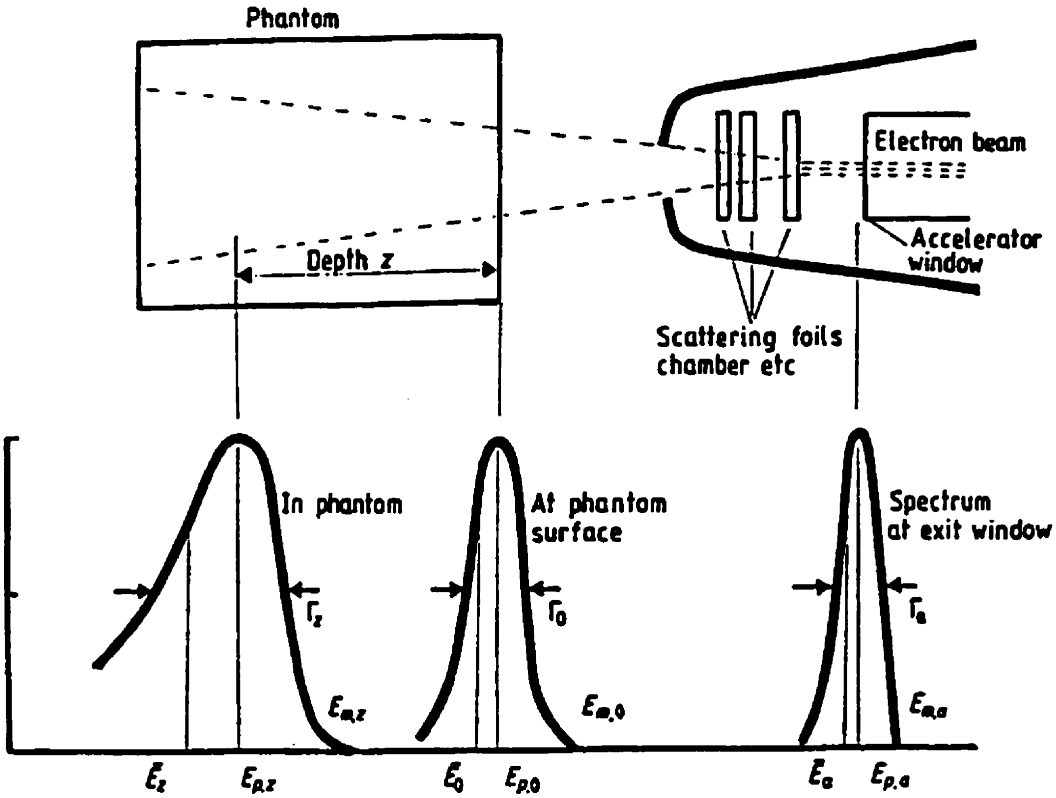

Figure 2.2: Electron beam energy parameters considered as the beam passes through the collimation system of the accelerator and the phantom[3].

According to the NACP[4] and ICRU 35[5], the constants are defined as $C_1 = 0.22$ MeV, $C_2 = 1.98$ MeV cm^{-1}, and $C_3 = 0.0025$ MeV cm^{-2}.

2.2.2 Determination of $\bar{E}_o$

Several dosimetry protocols such as TG-25[6] recommend the following relationship for determining the mean electron energy at the phantom surface:

$$\bar{E}_o = c_4 R_{50}, \tag{2.2}$$

where c_4 is a constant equal to 2.33 MeV/cm and R_{50} is the depth of the 50% depth dose curve. Alternatively, TG-25[6] also recommends the data presented in Fig. 2.3 for the determination of $\bar{E}_o$. R_{50} can also be determined from the measured value of I_{50} (the depth of 50% of the maximum ionization on the depth-ionization curve) using TG-51[7], the new protocol, whereby

$$R_{50} = 1.029\, I_{50} - 0.06 \text{ (cm)} \qquad (\text{for } 2 \le I_{50} \le 10 \text{ cm}), \qquad (2.3)$$

and

$$R_{50} = 1.059\, I_{50} - 0.37 \text{ (cm)} \qquad (\text{for } I_{50} > 10 \text{ cm}). \qquad (2.4)$$

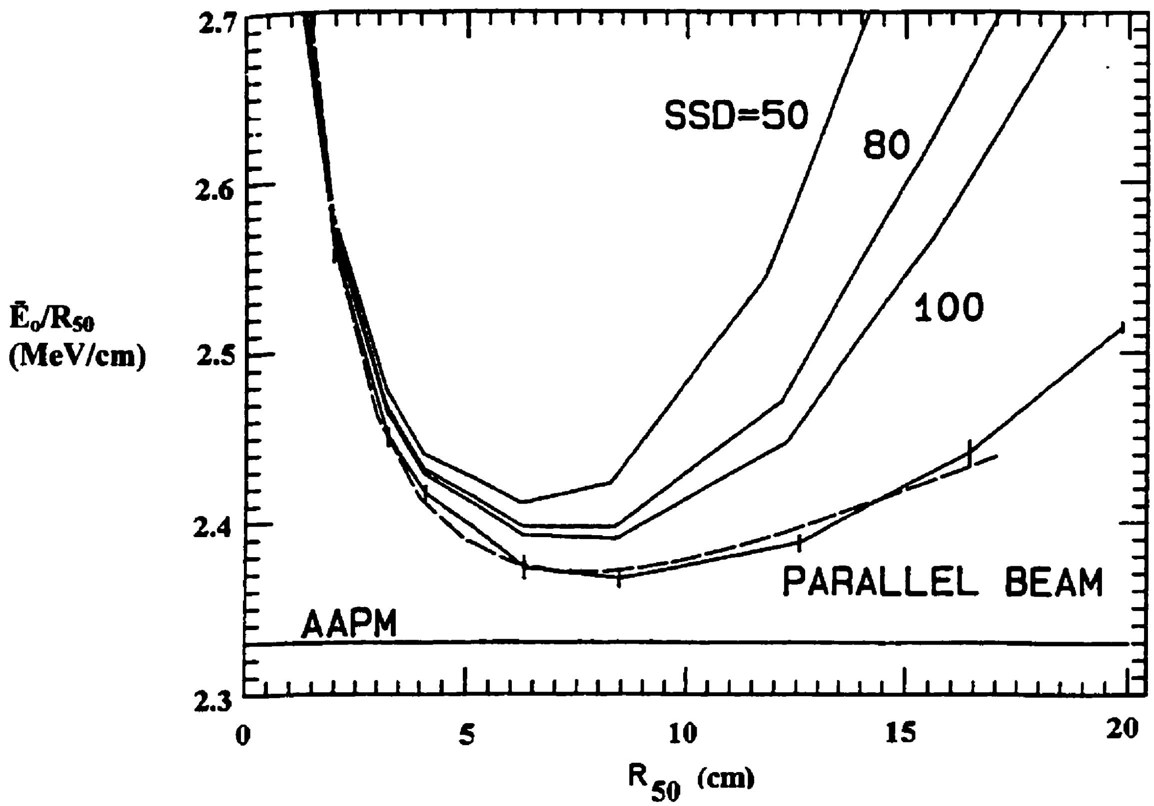

Figure 2.3: Values calculated by EGS4 for $\bar{E}_o/R_{50}$ as a function of R_{50} for various values of source-to-surface distance (in units of cm). The constant value recommended by the AAPM is also shown. The values for the parallel beam case predicted by Eq. (2) in Rogers[8] are shown as a dashed line[6].

2.2.3 Determination of $\bar{E}_z$

The mean electron energy, ($\bar{E}_z$) at depth z in phantom, is needed to determine the replacement correction of the ion chamber used for absorbed dose measurements[9]. As the electron beam penetrates the phantom, the mean electron energy at depth z decreases according to the following relationship:

$$\bar{E}_z = \bar{E}_o\,(1 - z / R_p). \qquad (2.5)$$

All of the energy parameters previously discussed ($E_{p,0}$, $\bar{E}_o$, and $\bar{E}_z$) as well as range parameters R_{50} and R_p are important in treatment planning, dosimetry, and energy specification. The above parameters can be obtained from a percentage depth ionization curve or a percentage depth dose (PDD) curve.

2.3 Stopping Power

When a photon or neutron interacts with matter, one of two events can occur. Either no interaction occurs, and hence no energy is lost, or it may lose all of its energy through single or several interactions. Conversely, charged particles such as electrons lose their energies through multiple interactions. Most interactions only transfer a small amount of energy, and therefore it can be assumed that they lose energy in a gradual manner, often referred to as the "continuous slowing-down approximation" (CSDA). Therefore, the electron beam loses energy slowly and continuously as it penetrates into the phantom, and one parameter to describe this energy loss is the stopping power. Stopping power is defined as "the expectation value of the rate of energy loss per unit of path length x by a charged particle of type Y and kinetic energy T, in a medium of atomic number Z, $(dT/dx)_{Y,T,Z}$"[1]. Stopping power is often expressed in units of MeV/cm. Mass stopping power can be calculated by dividing the stopping power by the density ρ of the absorbing medium, and it is typically expressed in MeV cm^2/g.

Stopping power can be subdivided into two categories: collisional stopping power (S_{col}) and radiative stopping power (S_{rad}). Collisional stopping power is the rate of energy loss due to soft and hard collisions, whereas the radiative stopping power is due to bremsstrahlung, or radiative collision (section 2.2.3).

The total stopping power (S_{tot}) is defined as:

$$(1/\rho)\, S_{tot} = (1/\rho)\, S_{col} + (1/\rho)\, S_{rad}\,. \tag{2.6}$$

Stopping power (S/ρ) increases significantly with depth since the incident electron beam loses energy as it penetrates into the phantom. The values of stopping power ratios of two media can be used to compare energy loss by the electron in one medium to another. In order to obtain a percentage depth dose curve in water for an electron beam, the ionization curve must be multiplied by $(\bar{L}/\rho)^{water}_{air}$, the restricted collision stopping power ratio of water to air at all depths. The restricted collision stopping power is used instead of the unrestricted collision stopping power, because the delta ray produced from hard collisions may be energetic enough to carry a significant amount of kinetic energy away. As a result, the dose in a small volume will be overestimated if the unrestricted collision stopping power is used. The restricted stopping power is defined as "that fraction of the collision stopping power that includes all the soft collisions plus those hard collisions resulting in δ rays with energies less than a cutoff value Δ" (Attix[1]). The stopping power ratio of the user's beam is selected by using the mean incident energy $\bar{E}_o$ as the electron beam energy. Tables of ratios of mean restricted collision mass stopping powers of water to air, $\left(\bar{L}/\rho\right)_{air}^{water}$, as a function of depth for various phantom materials are found in literature, and an example is shown in Table 2.1[9].

2.4 Dose measurements considerations

Some of the important considerations in dose measurements include the choice of phantom, measuring device, chamber polarity effect, and displacement correction. Various phantoms and dosimeters will be discussed in Chapter 4. Polarity and displacement corrections are reviewed below.

2.4.1 Chamber polarity effect

The ionization charges measured for both polarities may be significantly different, and this is known as the chamber polarity effect[10,11]. It has been found that the differences can be significant for both cylindrical chambers (about 10%) and plane parallel chambers (20%)[12]. The discrepancy is due to the energy distribution of the electron beam, and is more evident for lower electron energies. Therefore, measurements must be taken for both polarities, and the true ionization charge Q is given by the average of the positive and negative polarity readings: Q_+ and Q_- respectively, using the following equation[13]:

$$Q = \frac{(Q_+ - Q_-)}{2}. \tag{2.7}$$

TG-25[6] recommends that three ionization readings should be taken for each polarity. If the polarity effect is greater than 1%, then all readings must be corrected using Eq. 2.7.

	Electron Beam Energy (MeV)																			
Depth g/cm²	60	50	40	30	25	20	18	16	14	12	10	9	8	7	6	5	4	3	2	1
0.0	0.602	0.904	0.912	0.928	0.940	0.955	0.961	0.969	0.977	0.986	0.997	1.003	1.011	1.019	1.029	1.040	1.059	1.078	1.097	1.116
0.1	0.902	0.905	0.913	0.929	0.941	0.955	0.962	0.969	0.978	0.987	0.998	1.005	1.012	1.020	1.030	1.042	1.061	1.081	1.101	1.124
0.2	0.903	0.906	0.914	0.930	0.942	0.956	0.963	0.970	0.978	0.988	0.999	1.006	1.013	1.022	1.032	1.044	1.064	1.084	1.106	1.131
0.3	0.904	0.907	0.915	0.931	0.943	0.957	0.964	0.971	0.979	0.989	1.000	1.007	1.015	1.024	1.034	1.046	1.067	1.089	1.112	1.135
0.4	0.904	0.908	0.916	0.932	0.944	0.958	0.965	0.972	0.980	0.990	1.002	1.009	1.017	1.026	1.036	1.050	1.071	1.093	1.117	1.136
0.5	0.905	0.909	0.917	0.933	0.945	0.959	0.966	0.973	0.982	0.991	1.003	1.010	1.019	1.028	1.039	1.054	1.076	1.098	1.122	
0.6	0.906	0.909	0.918	0.934	0.946	0.960	0.967	0.974	0.983	0.993	1.005	1.012	1.021	1.031	1.043	1.058	1.080	1.103	1.126	
0.8	0.907	0.911	0.920	0.936	0.948	0.962	0.969	0.976	0.985	0.996	1.009	1.016	1.026	1.037	1.050	1.067	1.090	1.113	1.133	
1.0	0.908	0.913	0.922	0.938	0.950	0.964	0.971	0.979	0.988	0.999	1.013	1.021	1.031	1.043	1.058	1.076	1.099	1.121		
1.2	0.909	0.914	0.924	0.940	0.952	0.966	0.973	0.981	0.991	1.002	1.017	1.026	1.037	1.050	1.066	1.085	1.108	1.129		
1.4	0.910	0.916	0.925	0.942	0.954	0.968	0.976	0.984	0.994	1.006	1.022	1.032	1.044	1.058	1.075	1.095	1.117	1.133		
1.6	0.912	0.917	0.927	0.944	0.956	0.971	0.978	0.987	0.997	1.010	1.027	1.038	1.050	1.066	1.084	1.104	1.124			
1.8	0.913	0.918	0.929	0.945	0.957	0.973	0.981	0.990	1.001	1.014	1.032	1.044	1.057	1.074	1.093	1.112	1.130			
2.0	0.914	0.920	0.930	0.947	0.959	0.975	0.983	0.993	1.004	1.018	1.038	1.050	1.065	1.082	1.101	1.120	1.133			
2.5	0.917	0.923	0.934	0.952	0.964	0.981	0.990	1.000	1.013	1.030	1.053	1.067	1.083	1.102	1.120	1.131				
3.0	0.919	0.926	0.938	0.956	0.969	0.987	0.997	1.008	1.023	1.420	1.069	1.084	1.102	1.199	1.129					
3.5	0.922	0.929	0.941	0.960	0.974	0.994	1.004	1.017	1.034	1.056	1.085	1.102	1.118	1.128						
4.0	0.924	0.932	0.944	0.964	0.979	1.001	1.012	1.027	1.046	1.071	1.101	1.116	1.126							
4.5	0.927	0.935	0.948	0.969	0.985	1.008	1.021	1.037	1.059	1.086	1.115	1.125	1.127							
5.0	0.929	0.938	0.951	0.973	0.990	1.016	1.030	1.049	1.072	1.101	1.123	1.126								
5.5	0.931	0.940	0.954	0.978	0.996	1.024	1.040	1.061	1.086	1.113	1.125									
6.0	0.934	0.943	0.958	0.983	1.002	1.033	1.051	1.074	1.100	1.121										
7.0	0.938	0.948	0.965	0.993	1.017	1.054	1.075	1.099	1.118	1.122										
8.0	0.943	0.954	0.972	1.005	1.032	1.076	1.098	1.116	1.120											
9.0	0.947	0.960	0.981	1.018	1.049	1.098	1.114	1.118												
10.0	0.952	0.966	0.990	1.032	1.068	1.112	1.116													
12.0	0.962	0.980	1.009	1.062	1.103															
14.0	0.973	0.996	1.031	1.095	1.107															
16.0	0.986	1.013	1.056	1.103																
18.0	1.000	1.031	1.060																	
20.0	1.016	1.051	1.094																	
22.0	1.032	1.070																		
24.0	1.048	1.082																		
26.0	1.062	1.085																		
28.0	1.071																			
30.0	1.075																			

Table 2.1: Mean restricted collision mass stopping power ratio of water to air $\left(\bar{L}/\rho\right)_{air}^{water}$ ($\Delta = 10$ keV).

2.4.2 Displacement Correction

The displacement correction is necessary because the point of measurement is not always at the center of the chamber. For a thin parallel plate chamber, the effective point of measurement is taken to be at the inside surface of the chamber window (Fig. 2.4). However, for a cylindrical chamber, the effective point of measurement should be displaced by the distance equivalent to half of the radius of the sensitive volume towards the source from the center of the chamber (Fig. 2.5), and this applies for all depths and for all energies.

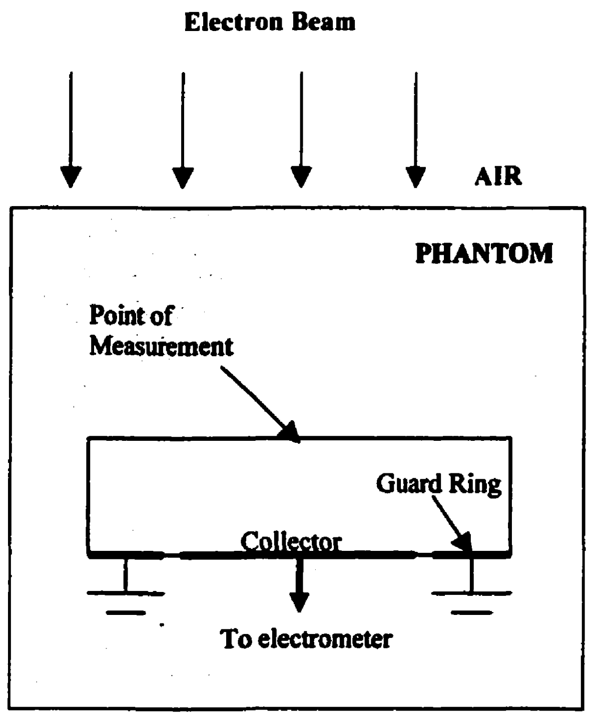

$$d = d_{\text{inside surface of chamber window}} \tag{2.8}$$

Figure 2.4: Diagram showing the point of measurement for a plane parallel chamber.

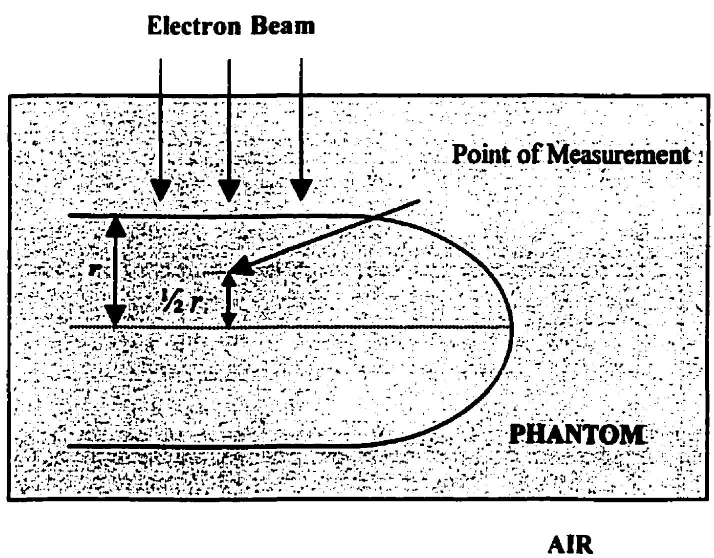

$$d = d_{center} - 0.5\, r \tag{2.9}$$

Figure 2.5: Diagram showing the point of measurement for a cylindrical chamber.

2.5 Summary

This chapter has discussed some of the important aspects related to the physics of electron beam dosimetry. The main types of electron interactions with matter including soft collisions, hard collisions, and bremsstrahlung have been reviewed. Various electron energy parameters can be determined through relationships with a depth dose curve. We have observed that the electron beam decreases in energy gradually as it penetrates into the phantom. Finally, some important considerations in measuring dose such as the polarity effect and displacement correction have been described.

2.6 References

1. F.H. Attix, Introduction to Radiological Physics and Radiation Dosimetry, John Wiley and Sons, Inc., New York, U.S.A. (1986).
2. International Commission on Radiation Units and Measurements (ICRU), Radiation Dosimetry: Electrons with Initial Energies Between 1 and 50 MeV, ICRU Report 21, Bethesda, Maryland (1972).
3. S.C. Klevenhagen, Physics and Dosimetry of Therapy Electron Beams, Medical Physics Publishing, Madison, Wisconsin, U.S.A. (1993).
4. Nordic Association of Clinical Physics (NACP), "Electron beams with mean energies at the phantom surface below 15 MeV", Acta Radiol. Oncol. Rad. Phys. 20, 402-415 (1981).
5. International Commission on Radiation Units and Measurements (ICRU), Radiation Dosimetry: Electron Beams with Energies Between 1 and 50 MeV, ICRU Report 35, Bethesda, Maryland (1984).
6. F.M. Kahn, K.P. Doppke, K.R. Hogstrom, G.J. Kutcher, R. Nath, S.C. Prasad, J.A. Purdy, M. Rozenfield & B.L. Werner, "Clinical electron-beam dosimetry: Report of AAPM Radiation Therapy Committee Task Group No. 25," Med Phys. 18, 73-109 (1991).
7. P.R. Almond, P.J. Biggs, B.M. Coursey, W.F. Hanson, M.S. Huq, R. Nath & D.W.O Rogers, "AAPM's TG-51 protocol for clinical reference dosimetry of high-energy photon and electron beams", Med. Phys. 26 (9), 1847-1870 (1999).

8. D.W.O. Rogers & A.F. Bielajew, "Differences in electron depth-dose curves calculated with EGS and ETRAN and improved energy-range relationships", Med. Phys. 13, 687-691 (1986).
9. American Association of Physicists in Medicine (AAPM), RTC Task Group 21, "A protocol for the determination of absorbed dose from high energy photon and electron beams", Med. Phys. 10, 741-771 (1983).
10. L.O. Mattsson, K.A. Johansson & H. Svensson, "Calibration and use of plane-parallel ionization chambers for the determination of absorbed dose in electron beams", Acta Radiol. Oncol. 20, 385-399 (1981).
11. B.J. Gerbi & F.M. Khan, "The polarity effect for commercially available plane-parallel ionization chambers", Med. Phys. 14, 210-215 (1987).
12. H. Aget & J. Rosenwald, "Polarity effect for various ionization chambers with multiple irradiation conditions in electron beams", Med. Phys. 18 (1), 67-72 (1991).
13. J.S. Pruitt, Calibration of beta-particle-emitting ophthalmic applicators, Natl. Bur. Stand. (U.S.), Spec. Publ. 250-9, U.S. Government Printing Office, Washington, D.C. (1987)

CHAPTER 3: INTRODUCTION TO MEDICAL PHYSICS

In this chapter, an overview of the operation of a linear accelerator will be presented, and several beam characteristics will be discussed. They include percentage depth dose (PDD), dose profiles and output.

PDD describes the dose along the central axis parallel to the incident beam, whereas dose profiles specify the dose along the plane perpendicular to the beam at the same depth. Output is defined as the absolute dose at a specific point, usually at the depth of dose maximum (d_{max}).

3.1 Linear Accelerators

The microwave-powered electron linear accelerator, commonly referred to as the linac, has gradually replaced the traditional radiotherapy machines such as the Cobalt unit, x-ray machine and the Van de Graff generator. As of 1984, linacs constituted over one-half of all megavoltage treatment units in service and about 90% of newly installed units in the U.S.[1]

Linacs are able to provide low and high energy x-ray, as well as a wide range of electron beam energies. As a result, one can utilize the optimal modality and energy for a specific tumor type and location.

3.1.1 Basic operation of linear accelerators

In order to accelerate particles, the following two conditions must be met: the particle must be charged, and an electric field must be present in the direction of propagation of the particle[2]. Linacs are cyclic accelerators, whereby electrons are cycled through the same, small potential difference many times. Electrons are accelerated to kinetic energies from 4 to 25 MeV using non-conservative microwave RF (radiofrequency) fields in the frequency range from 10^3 MHz (L band) to 10^4 MHz (X band), the most common being the S band, at 2856 MHz. The high power RF fields are produced either in the magnetron or klystron, through the process of decelerating electrons in retarding potentials. The electrons are accelerated in a straight manner in an evacuated waveguide. As derived in Podgorsak *et al.*[2], the velocity of the electric field pattern, or the phase velocity of the wave, v_{ph} is greater than c, the speed of light, ie. $v_{ph} > c$. Since particle velocity, v_{part} must equal v_{ph} for particle acceleration in a linac, and the particle velocity cannot exceed c, the particle cannot follow; and therefore, the uniform waveguide is not suitable for particle acceleration. In order to resolve this, v_{ph} must be slowed down below c so that the electrons can follow the electric field pattern, and this can be achieved by adding obstacles into the waveguide. A series of discs (irises) with circular holes in the center are placed periodically in a uniform waveguide, slowing down v_{ph} and dividing the waveguide into cylindrical cavities. This design of waveguide is referred to as "disk-loaded" or "iris loaded".

3.1.2 Clinac 18 and Clinac 2300 C/D electron linear accelerators

The linacs used for measurements in this study are a Clinac 18 and a Clinac 2300 C/D (Varian, Palo Alto, CA). The Clinac 18 provides a photon beam with a nominal energy of 10 MV, and electron energies of 9, 12, 15, and 18 MeV. The Clinac 2300 C/D provides dual photon energies of 6 MV and 18 MV, as well as electron energies of 6, 9, 12, 15, 18 and 22 MeV. Both linacs are isocentrically mounted with an SAD (source-axis distance) of 100 cm. The dose rate supplied by the Clinac 2300 C/D varies from 100 to 600 MU/min, in increments of 100 MU/min; while the dose rate available on the Clinac 18 ranges from 100 to 500 MU/min, also in increments of 100 MU/min. For electron treatments, cones must be used to further collimate the beam. The electron cones available for the Clinac 2300 C/D are 6x6 cm^2, 10x10 cm^2, 15x15 cm^2, 20x20 cm^2, and 25x25 cm^2, and the cones for the Clinac 18 are 4x4 cm^2, 6x6 cm^2, 8x8 cm^2, 10x10 cm^2, 15x15 cm^2 and 25x25 cm^2.

3.1.3 *Basic components of a linear accelerator*

A medical linac typically consists of 5 major components, comprising the injection system, the RF system, the auxiliary system, the beam transport system, and the linac head. These components are described below and shown in Fig. 3.1.

3.1.4 *Injection system*

The injection system consists of an electron gun, which supplies the electrons. There are two types of electron guns: diode and triode, and both contain a heated cathode and a perforated anode, but the triode also has a grid. Electrons are emitted thermionically from the heated cathode, while a curved focusing electrode focuses the electrons into a pencil beam. The electrons accelerate through the perforated anode and enter the waveguide. The linacs used for this thesis each has a triode gun. Its operation is similar to the diode's, with the exception of the grid, which is placed between the cathode and the anode. Normally, the grid is negative with respect to the cathode, and there is no current to the anode. However, voltage pulses, which are synchronized with the pulses from the microwave generator, are applied to the grid. When the voltage is positive with respect to the cathode, the electrons will travel through the anode and into the waveguide.

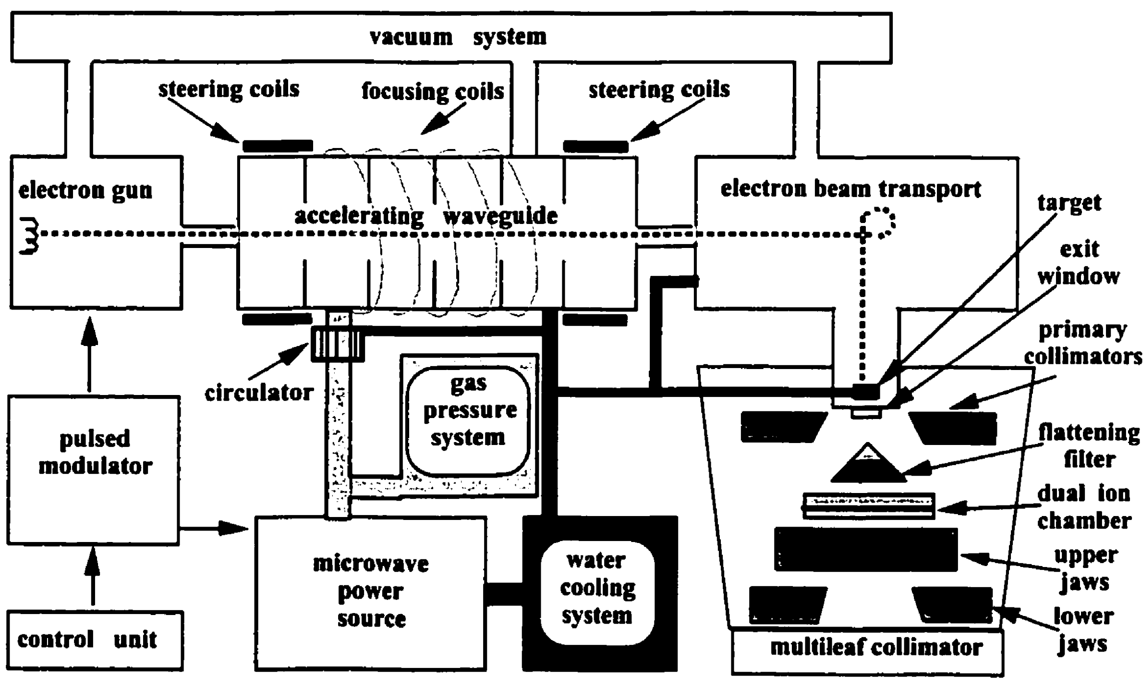

Figure 3.1: Schematic diagram for a typical linac[2].

3.1.5 RF system

The RF system consists of many components, including the RF power source, a modulator, a control unit, an accelerating waveguide, and a circulator.

The RF power source is either a magnetron or a klystron. Magnetrons are sources of high power RF and are often used for low energy linacs. On the other hand, klystrons are RF power amplifiers that amplify the low power RF from RF oscillators. The circulator ensures the RF power propagates in one direction only – from the source to the waveguide, thus sparing damage to the gun. As shown in Fig. 3.1, the pulsed modulator provides the high power and short duration pulses, which are sent to the electron gun and the RF power generating system (either the klystron or magnetron). The control unit synchronizes the timing of these pulses.

The electrons supplied by the electron gun accelerate in the waveguide. Waveguide cavities are typically about 10 cm in diameter and from 2.5 cm to 5 cm in length. They couple and distribute microwave power in the waveguide, and provide an electric field for particle acceleration. There are two types of waveguides: standing wave and travelling wave. Early designs of linacs use travelling waveguides, where one in four cavities is used for particle acceleration. The electrons enter and leave the waveguide in opposite ends; and the residual microwave power is absorbed into the load at the exiting end. The linacs used for this work employ the standing wave design, whereby only one in two cavities is used for acceleration. Contrary to the travelling waveguide, the waves are reflected at both ends. The resultant field is the sum of the forward and backward components, and every other cavity has a zero field always. This can be achieved in two ways, either the waves in both directions equal zero, or the waves cancel each other by having the same amplitude in opposite directions. These zero field cavities only propagate microwave power, but do not participate in particle acceleration. Hence, they can be moved off axis, in a staggered manner, resulting in a shorter waveguide.

3.1.6 Auxiliary system

The auxiliary system consists of a vacuum pumping system, a water cooling system, a gas pressure system for pneumatics, a gas dielectric system for transmission of microwaves from the RF generator to the accelerating waveguide, and shielding against leakage radiation.

3.1.7 Beam transport system

The main goal of the beam transport system is to direct the electron beam from the waveguide to the target or scattering foil, depending on the modality chosen. The isocentric linacs of straight-ahead beam design which produce low x-ray energies of 4 or 6 MV do not require the use of magnets. However, higher energy linacs require a beam transport system to steer the electron beam to the target or scattering foil, and this can be achieved by using a 90° magnet, a 270° magnet, or a slalom system. A 90° bending magnet is not achromatic. Therefore, beams of different energies are bent differently, similar to a mass spectrometer, resulting in a large focal spot. The linacs used in this work employ the 270° bending magnet which is achromatic, where all the beams are bent in the same manner and converge on a single focal point.

Two remaining components that are pertinent in a beam transport system are the steering coils and the focusing coils (both of which are installed on the waveguide). The steering coils keep the electron beam close to the central axis while undergoing acceleration in the waveguide. They also steer the beam towards the beam transport system or onto the x-ray target for straight through linacs. The focusing coils focus the pencil beam to minimize divergence, as there is a small repulsion between electrons.

3.1.8 Treatment head

The treatment head is responsible for the production, shaping, localizing, and monitoring of the clinical photon and electron beams. Some of the components found inside a linac head include the retractable x-ray targets, flattening filters and electron scattering foils, primary and adjustable secondary collimators, dual transmission ionization chambers, a field defining light, a range finder, and possibly retractable wedges and multi-leaf collimator (MLC). Most of these components are common in the production of electron and photon beams, but some of them are specific to the beam modality.

Clinical photon beams are produced by allowing the pencil electron beam to strike an x-ray target. The electrons are decelerated due to the interactions with the positively charged nuclei of the x-ray target. The radiative losses (bremsstrahlung) in the target from this interaction produce the high energy photon beam. A 10 MeV electron beam striking a thick target will give a heterogeneous photon spectrum of energies up to 10 MV. There will be a few photons with 10 MeV energy, but none with higher energies[3]. A flattening filter is used to preferentially attenuate the photon beam at the central axis, as it is mostly forward peaked at high energy. One can then obtain a flat beam that is useful for radiotherapy. The x-ray target and the flattening filter are both made of copper on the linacs used in this work.

On the other hand, electron beams are produced by retracting the target and flattening filter from the beam's path, and replacing them with a scattering foil, to spread the pencil beam in order to cover the field size needed for treatment. The flattening filters and scattering foils are often placed on a carousel or a drawer for easy manipulation. Electron applicators are mounted onto the accessory plate for further collimation, and they normally extend up to 4 or 5 cm above the nominal SAD of 100 cm.

The dual ion chambers monitor the beam output and symmetry continuously during treatment. After a pre-determined number of monitor units has been delivered to the patient, the beam will automatically shut off. The dual chambers run independently; so that if one fails, the other will terminate the treatment after 25 MU or +10%, whichever is lower. In the unlikely event that both chambers fail, the linac timer will shut down the machine with minimal extra dose to the patient.

3.2 Percentage Depth Dose

Percentage depth dose (PDD) is measured in water or water-equivalent solid material, along the central axis of the beam. PDD is a function which depends on *d*, the depth in water; *f*, the source to surface distance; *A*, the field size area at the phantom surface; and *E*, the effective energy of the beam. PDD is defined as:

$$PDD(d,A,f,E)=100\left(\frac{D_Q}{D_P}\right), \tag{3.1}$$

where D_Q is the dose at depth d (point Q), and D_P is the dose at depth of dose maximum, d_{max} (point P), as shown in Fig. 3.2[2]. For an electron beam, PDD initially increases with depth from a surface dose of about 80%-90% to a maximum of 100%, then decreases quite rapidly with depth, as illustrated in Fig. 3.3[4].

In this thesis, the relationships of PDD with energies and different field sizes, particularly small ones, are investigated. The field sizes range from rectangular cutouts of size 10 x 1 cm^2 to 10 x 4 cm^2, circular cutouts of sizes 1 cm to 6 cm in diameter, and square field sizes up to the largest available cone of 25 x 25 cm^2. The energies range from 9 to 18 MeV on a CL 18; and from 6 to 22 MeV on a CL 2300 C/D.

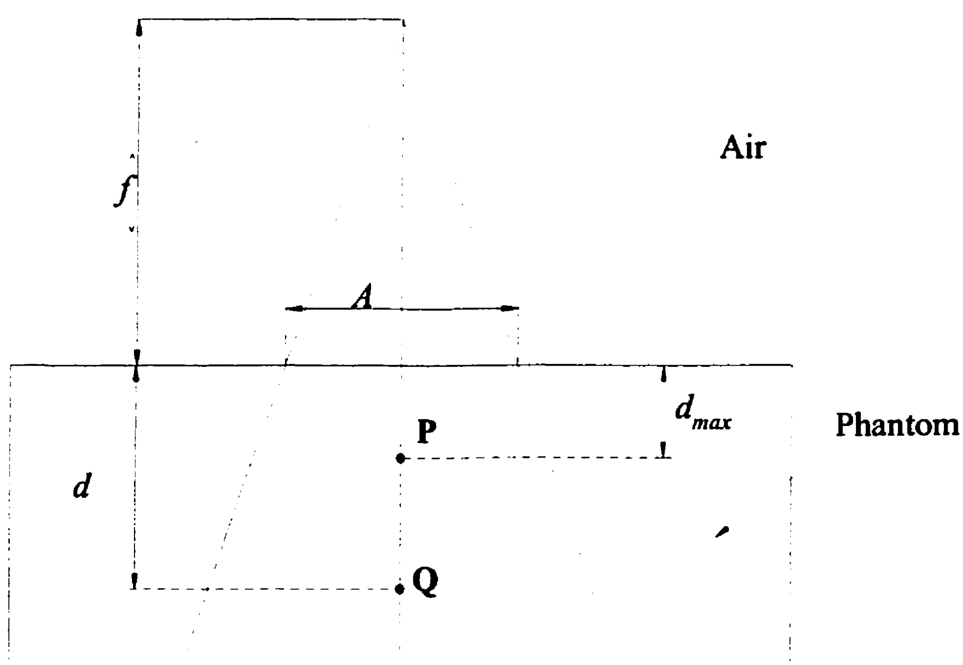

Figure 3.2: Diagram showing the set up for PDD measurements: D_P is the dose at point P (d_{max}), D_Q is the dose at point Q (arbitrary depth), f is the source to surface distance, and A is the field size at the phantom surface.

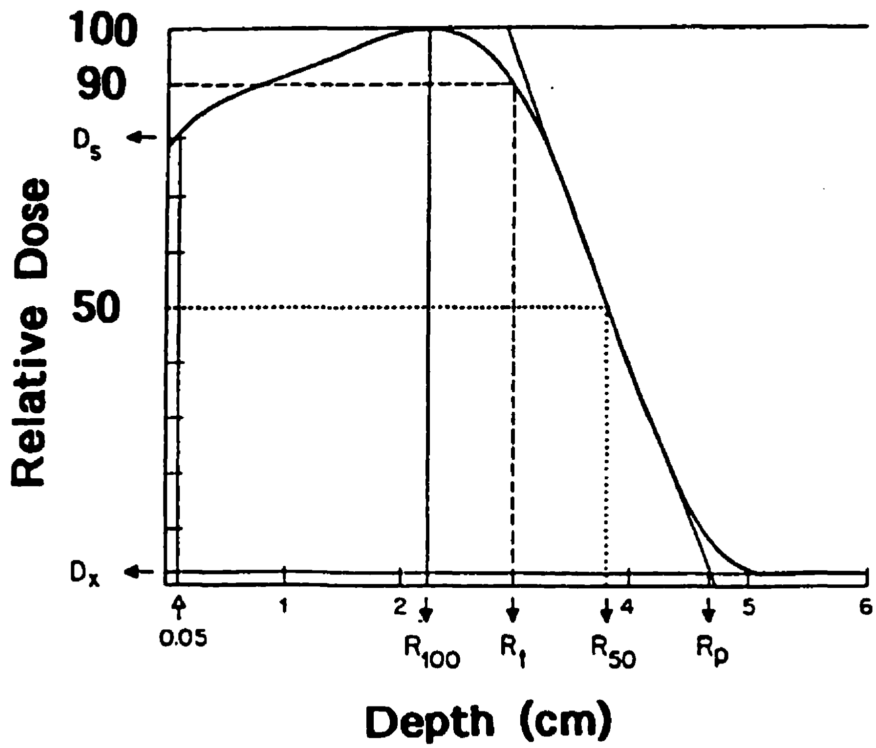

Figure 3.3: A typical electron PDD curve[4].

Since electron beams have a sharp drop-off in dose past the therapeutic depth (depth of 80% or 90% of maximum dose), electron beams are often the modality of choice in treating superficial tumors. The main parameters that describe a PDD curve include the surface dose, the depth of maximum dose, the therapeutic depth, the depth of 50% of the maximum dose, the practical range, and the bremsstrahlung dose.

The relative surface dose D_s is defined at a depth of 0.5 mm. This depth is chosen to avoid errors at the air-phantom interface, and also because the sensitive layers of the epidermis are at this depth. D_s increases with energy, as shown in Fig. 3.4.

R_{100} (or d_{max}) is the depth of maximum dose. Fig. 3.4 shows a series of PDD curves with energies ranging from 6 to 22 MeV. D_{max} initially increases with energy, then decreases, and it also broadens with increased energy. However, d_{max} also varies with field size, and this project will investigate the relationship of d_{max} with field sizes smaller than 6 cm^2.

R_t is the therapeutic depth and describes the clinically useful portion of the PDD curve. It is usually defined as either the depth at 90% (d_{90}) or 80% dose (d_{80}). TG-25[4] recommends the depth of 90% as the therapeutic depth. It also increases with increasing energy of the beam. Similarly, R_{50} (or d_{50}) is defined as the depth of the 50% dose level.

R_p is the practical range, and it is determined from the PDD curve as the depth where the tangent of the fall-off portion of the curve meets with the bremsstrahlung tail.

Finally, the relative dose due to x-ray contamination, or bremsstrahlung, D_x is due to the interaction of the electron beam with the scattering foil, electron cone, air, and patient. It is extrapolated from the PDD curve beyond the maximum range of electrons. The bremsstrahlung dose increases with the energy of the electron beam.

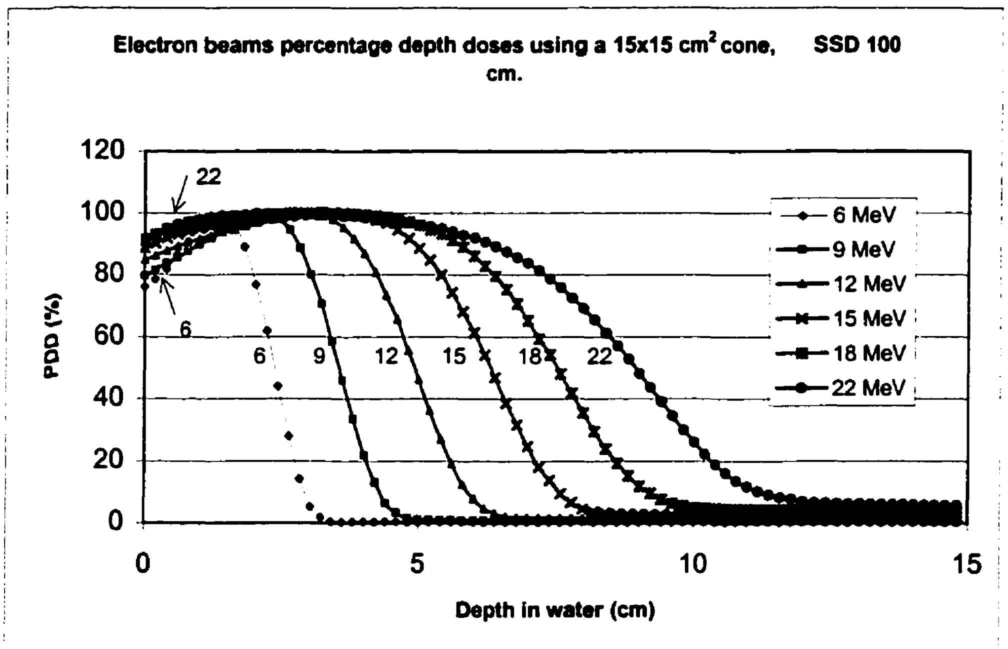

Figure 3.4: Energy dependence of PDD on a CL 2300 C/D. Curves from left to right: 6 MeV, 9 MeV, 12 MeV, 15 MeV, 18 MeV, 22 MeV.

3.3 Dose profiles

Beam profiles are measured in water or water-equivalent solid material, along the beam axes that are perpendicular to the beam. Often, profiles are measured at various depths, since the off-axis dose must be known for proper treatment planning. In this thesis, profiles are measured at six depths: $d_{surface}$, d_{max} ,d_{90}, d_{80}, d_{50}, d_{20}. The dose at surface is measured at 0.05 cm, in order to avoid possible errors at air-water interface as mentioned previously.

Beam profiles must agree with the specifications outlined in the AAPM TG-25[4]. TG-25[4] recommends that the plane of measurement be at the 95% dose depth, and that "the variation in dose normalized to the central-axis value should not exceed ±5% (optimally within ±3%) over an area confined within lines 2 cm inside the geometric edge of fields equal to or larger than 10 x 10 cm^2". For field sizes smaller than 10 x 10 cm^2, the specified area is defined as 1.5 cm within the geometric edge of field. In addition to the flatness requirement, there are also guidelines with respect to beam symmetry. TG-25[4] recommends that "the cross beam dose profile in the plane of reference should not differ more than 2% at any pair of points situated symmetrically with respect to the central ray".

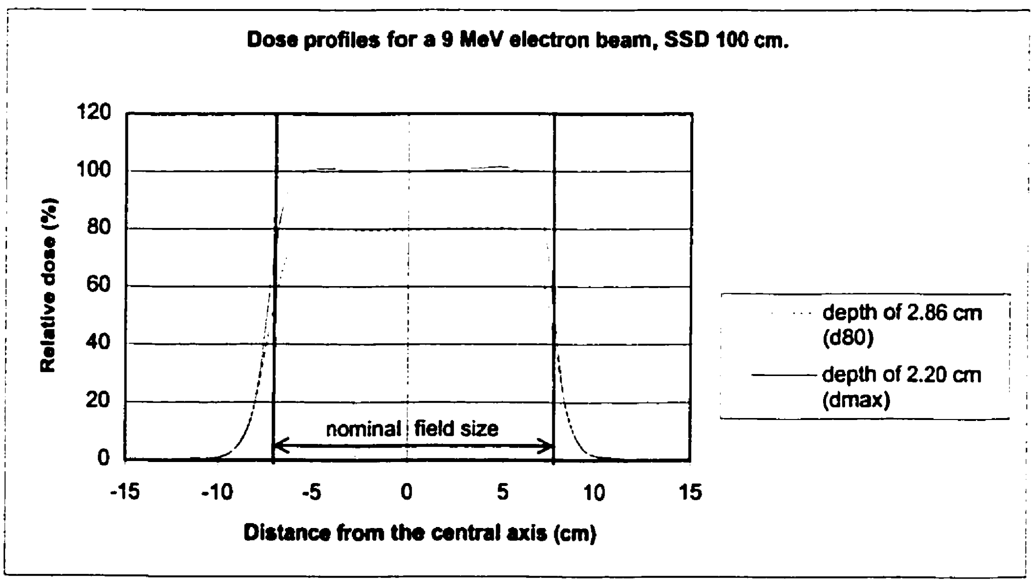

Figure 3.5: Profiles of a 9 MeV beam from a 2300 C/D, for a 15 x 15 cm^2 cone at 2 different depths.

3.4 *Output factors*

The relative output factor is defined as the ratio of the maximum dose per 100 MU along the central axis of the field of interest to that of the reference or calibrated field size[5]. The output or absolute dose rate in cGy/100MU of an electron beam is heavily influenced by the field size, and this has implications for clinical dosimetry with irregular or small field sizes.

3.5 *Summary*

In this chapter, the basic operation of a linear accelerator (linac) was introduced. In addition, several beam characteristics that are relevant to this study were discussed, including the percentage depth dose (PDD), dose profiles, and output factor.

3.6 *References*

1. C.J. Karzmark, "Advances in linear accelerator design for radiotherapy," Med. Phys. 11, 105 (1984).
2. E.B. Podgorsak, P. Metcalfe & J. Van Dyk, in Chapter 11, "Medical Accelerators," in The Modern Technology of Radiation Oncology, ed. Jacob Van Dyk (Madison: Medical Physics Publishing, 1999), 351-381.
3. H.E. Johns & J.R. Cunningham, The Physics of Radiology, 4th edition, Charles C. Thomas, Springfield, Illinois, U.S.A. (1983).
4. F.M. Kahn, K.P. Doppke, K.R. Hogstrom, G.J. Kutcher, R. Nath, S.C. Prasad, J.A. Purdy, M. Rozenfield & B.L. Werner, "Clinical electron-beam dosimetry: Report of AAPM Radiation Therapy Committee Task Group No. 25," Med Phys. 18, 73-109 (1991).
5. M.D. Mills, K.R. Hogstrom & R.S. Fields, "Determination of electron beam output factors for a 20 MeV linear accelerator," Med. Phys. 12, 473 (1985).

CHAPTER 4: DOSIMETERS AND PHANTOMS

This chapter discusses the differences between relative and absolute dose measurements. Absolute dosimetry methods include calorimetry, Fricke dosimetry, and standard ionization chamber, whereas relative dosimetry techniques include diode, TLD (thermoluminescence dosimetry), film, and Farmer-type ionization chamber. In this work, relative dosimetry techniques are used, and they will be discussed in detail. Finally, a comparison between different phantom types is presented.

4.1 Absolute Dosimetry

Absolute dosimetry techniques are used to measure the absorbed dose at a specific point in a phantom. Absorbed dose, *D*, expressed in Gray (1 Gy = J/kg), has been defined "to describe the quantity of radiation for all types of ionizing radiation, including charged and uncharged particles, all materials, and all energies. Absorbed dose is a measure of the biologically significant effects produced by ionizing radiation"[1]. It is given by

$$D\,(Gy) = \frac{dE}{dm}, \tag{4.1}$$

where dE (joules) is the mean energy imparted by ionizing radiation to material of mass dm (kg)[1].

Absolute dosimetry is a crucial step in the proper tumor dose delivery for palliation or cure. Of the three methods available, calorimetry is often recognized as the most absolute. However, due to logistical considerations, it is rarely used in a clinical setting, and therefore Fricke dosimetry and standard ionization chamber techniques are more common.

4.1.1 Calorimetry

Calorimetry uses the principle that the energy absorbed in a medium from radiation appears ultimately as heat energy. The heat energy manifests itself as a small increase in temperature of the absorbing medium, which is related to the energy absorbed per unit mass or the absorbed dose. However, a small amount of the energy absorbed, often negligible, may appear in the form of a chemical change, referred to as heat defect.

The absorbed dose D is given by:

$$D = \frac{dE_h}{dm} + \frac{dE_s}{dm}, \tag{4.2}$$

where dE_h is the energy given off as heat in the absorber of mass dm and dE_s is the energy absorbed or produced as a result of a chemical change. One Gray (Gy) of dose is defined as:

$$1\,Gy = 1\,J\,kg^{-1} = \left(\frac{1}{4.18}\right) cal\,kg^{-1}, \tag{4.3}$$

where 4.18 is the mechanical equivalent of heat (4.18 J of energy = 1 calorie of heat). Since the specific heat of water is 1 cal/g/°C or 10^3 cal/kg/°C, the rise in temperature of water (ignoring heat defect) by the absorption of 1 Gy of dose is calculated as:

$$\Delta T = \frac{1}{4.18}\left(cal\ kg^{-1}\right) \cdot \frac{1}{10^3}\,(kg\ cal^{-1}\ {}^{\circ}C)$$

$$= 2.39 \times 10^{-4}\,{}^{\circ}\mathrm{C} \tag{4.4}$$

The temperature rise is very small, and therefore accurate measurements cannot be taken for small doses. In order to obtain the absorbed dose, one must measure the temperature rise using thermistors, which are semiconductor devices that display a large change (about ± 5%) in electrical resistance with a small change in temperature (± 1%)[1]. In turn, the resistance is measured by an apparatus known as the Wheatstone bridge. An extensive review of calorimetry is discussed in Laughlin and Genna[2], and Gunn[3-5].

4.1.2 Chemical Dosimetry

Chemical Dosimetry is based on the principle that the energy absorbed from ionizing radiation may produce a chemical change, which in turn can be used to measure absorbed dose. The most common type is the Fricke dosimeter, also known as the ferrous sulphate dosimeter. It is made of 1 mmol/l ferrous sulphate (or ferrous ammonium sulphate), 1 mmol/l NaCl and 0.4 mmol/l sulphuric acid. The purpose of NaCl is to counteract the effects of organic impurities that might be present. After the solution is irradiated, the ferrous ions, Fe^{2+} are oxidized by radiation to ferric ions, Fe^{3+}.

$$Fe^{2+} \rightarrow Fe^{3+}, \tag{4.5}$$

A spectrophotometer is used to determine the ferric ion concentration. Spectrophotometry of the dosimeter solution displays absorption peaks in the ultraviolet region, at wavelengths of 224 nm and 304 nm. The absorbed dose (Gy), *D*, is defined as:

$$D = \frac{\Delta M}{\rho\, G} \times 9.64 \times 10^{6} (Gy), \tag{4.6}$$

where ΔM is defined as the concentration of ferric ions produced (moles/l), ρ is the density of the solution in kg/l, and G is defined as the number of molecules produced per 100 eV of energy absorbed. A constant G value of 15.7 ± 0.6 molecules/100 eV is recommended for electrons in the energy range of 1 to 30 MeV for 0.4 mol/liter of H_2SO_4 dosimeter solution[6]. TG-21[7] has described some of the advantages and disadvantages associated with Fricke dosimetry. The composition of the solution is similar to water, hence the dose to the solution can be approximated as equal to the dose to water (and by extension, tissue). The response and dose rate are independent and no calibration is required at a standards lab, however, as a consequence, there is also a lack of consistency among centers. In addition, cleanliness and care must be taken at the working lab and a UV spectrophotometer is also required. The uncertainty of the G value is about ±3%, hence Fricke dosimetry is not as precise as calorimetry. Compared to an ion chamber, Fricke dosimetry requires more time for dose measurements, and large doses, about 1000 cGy are required for accurate results.

4.1.3 Bragg-Gray cavity theory

The dose in a medium can be calculated from ion chamber measurements using the Bragg-Gray cavity theory. In other words, the Bragg-Gray relationship converts the ionization in a small, gas-filled cavity to energy absorbed in the medium surrounding the cavity[7].

The dose in the medium is calculated using the following equation[7]:

$$D_{med} = M \cdot N_{gas} \cdot \left(\bar{L} / \rho\right)_{air}^{med} \cdot P_{ion} \cdot P_{repl}, \tag{4.7}$$

where D_{med} is the absorbed dose to the phantom medium at the position of the chamber center. M is the ionization charge reading corrected for temperature and pressure, and N_{gas} is the dose to cavity air per unit ionization charge or reading. $(\bar{L} / \rho)_{air}^{med}$ is defined as the ratio of the mean restricted mass collision stopping power of medium to that of air. Finally, P_{ion} is the ion-recombination correction, and P_{repl} is the perturbation or replacement correction factor.

If the measurements are not taken in a water phantom, then D_{med} must be converted to D_w (dose to water) using the following relationship:

$$D_w = D_{med} \cdot \left(\bar{S} / \rho\right)_{med}^{W} \Phi_{med}^{W}, \tag{4.8}$$

where $(\bar{S} / \rho)_{med}^{W}$ is the ratio of mean non-restricted collision stopping power of water to that in the medium, and Φ_{med}^{W} is the ratio of electron fluence in water to that in the medium.

The formula for N_{gas} is found in equation 6 of TG-21[7]. N_{gas} depends on the value W, which is the average energy expended to produce an ion pair by the electronic charge. Measurements taken with a standard ionization chamber are not as absolute as the ones measured with calorimetry because the value of W changes over time, with the most recent value equal to 33.97 J/C[1].

4.2 Relative Dosimetry

Relative dosimetry techniques are used to measure isodoses, profiles and PDD, and all of the measurements taken for this work were relative measurements. Some relative dosimeters such as TLD must be calibrated in a known radiation field, however, this is not necessary for most dosimeters such as ion chambers and diodes, which are predominately used for PDD measurements. Unlike absolute dosimeters which give the absolute dose at a specific point, relative dosimeters are only capable of giving the ratio of the dose at one point in the phantom to the dose at another point. In this work, several dosimeters are used, and they include film, solid state diodes, and the Farmer-type ionization chamber.

There are some important considerations regarding the measurements of electron PDDs with an ionization-type chamber. The electrons set in motion in the medium by a photon beam (through photoelectric effect, Compton effect, and pair/ triplet production) have basically the same average energy at all depths. Therefore, energy dependent parameters which relate ionization to dose are constant with depth in the medium. PDD is given simply by the ratio of charge at depth to the charge at d_{max}. On the other hand, electrons lose energy in a gradual and continuous manner with depth (pg. 9); therefore, energy dependent parameters relating ionization to dose, such as the stopping power, changes with depth in the medium. The PDD is then defined as[8]

$$PDD = \left(\frac{\{M \times (\bar{L}/\rho)_{air}^{water} \times (\Phi)_{med}^{water} \times P_{repl}\}_d}{\{M \times (\bar{L}/\rho)_{air}^{water} \times (\Phi)_{med}^{water} \times P_{repl}\}_{d_{max}}} \right) \times 100, \tag{4.9}$$

where all the variables have been defined on pg. 29.

The factors in the numerator are taken at depth in the phantom, whereas the factors in the denominator are taken at d_{max}. It can be assumed that Φ_{med}^{water} and P_{repl} are constant with depth, therefore Eq. 4.9 can be simplified to Eq. 4.10, and this is the equation that is applied to the ionization measurements obtained with an ion chamber in this thesis.

$$PDD = \left(\frac{\{M \times (\bar{L}/\rho)_{air}^{water}\}_d}{\{M \times (\bar{L}/\rho)_{air}^{water}\}_{d_{max}}} \right) \times 100 . \qquad (4.10)$$

4.2.1 Silicon Diode

Silicon diodes are only used for relative measurements because the actual collecting volume (depletion region) is not well known[6]. Hence data that was obtained with diodes should always be verified with data measured with an ion chamber. Compared to an ion chamber, a diode is smaller and its sensitivity is thousands of times higher than that of an air ion chamber[8]. In addition, since there is no bias voltage, it does not require polarity corrections. Finally, the silicon to water stopping power ratio varies minimally with electron energy (about 5% between 1 and 20 MeV) and hence stopping power correction is not usually applied for depth dose measurements. A major drawback of diode is that its dose rate dependence can change with time due to accumulation of radiation damage. High energy electrons, photons, and neutrons can displace atoms in the crystal lattice, creating imperfections that serve as traps. As a result, the sensitivity of the diode is reduced[8].

4.2.2 Film dosimetry

Films are also only used for relative measurements because the optical density depends on many variables such as inter-film emulsion differences, changes in processing conditions, magnitude of absorbed dose and some measurement conditions. These factors can give rise to major artifacts. Regardless, film is often used, particularly for beam profiles, isodose curves, and determination of practical range. It is convenient, rapid and provides a permanent record. Its sensitivity independence on energy and depth, good spatial resolution and commercial availability make film a popular choice among relative dosimeters[8]. However, one major disadvantage is the requirement for wet chemical processing. Although the processing conditions do not greatly affect the shape of a sensitometric curve, the optical density value depends heavily on the processing temperature and developing time. A variation of 0.1°C in the bath temperature or 2-3 seconds in developing time can result in a variation of 1% in optical density[6]. Similar to the diode, the ratio of collision stopping powers between emulsion and water vary slowly with electron energy, and stopping power corrections are not necessary[1].

A radiographic film consists of a transparent film base made of cellulose acetate or polyester resin, which is coated with an emulsion containing very small crystals of silver bromide. A latent image is formed after the film is exposed to ionizing radiation or light. When the film is developed, the affected crystals are reduced to small grains of metallic silver, which in turn cause the darkening of the film. Therefore, the radiation energy absorbed depends on the amount of silver deposited, which is consequently related to the blackening of the film. A film densitometer (Model WP 102, Wellhöfer Dosimetrie) was used to determine the degree of darkening by measuring the optical density. It consists of a light source, a tiny aperture and a light detector (photocell) which measures the light intensity transmitted through the film. The optical density (*OD*) is defined as

$$OD = \log \frac{I_o}{I_t}, \tag{4.11}$$

where I_o is the amount of light collected without the film and I_t is the amount of light transmitted through the film. The net *OD* is obtained by subtracting the base fog, defined as the *OD* of an unexposed processed film, from the measured *OD* reading. A plot of the net *OD* vs. radiation exposure or dose gives the sensitometric curve or the H-D curve (Hurter and Driffield, 1890).

4.2.3 Ion chambers

There are two main types of ion chambers: thimble chambers and parallel plate chambers. They are readily available, portable, easy to use, and their results are highly reproducible. Also, since they must be calibrated against a national primary standard, there is a consistency maintained among different centers. In Canada, the institutional standard (also called the secondary standard) is sent to NRCC (National Research Council of Canada) in Ottawa. However, ionization to dose conversion factors such as stopping power ratios depend on energy and depth; therefore, all points on a depth ionization curve must be corrected with Eq. 4.10 to obtain a depth dose curve.

4.2.4 Thimble chamber

A cross-section of a thimble chamber or Farmer-type chamber, named after F.T. Farmer[9], is shown in Fig. 4.1. It has a cylindrical wall, often referred to as the outer electrode, which is made of graphite, and an inner surface coated by a special electrically conductive material, and contains an unsealed air cavity volume of about 0.6 cm^3. In the center of the cavity, there is a collecting electrode, which is a rod of low Z material, often aluminum. The thimble consists of both electrodes and the air cavity, and a high potential (usually ± 300V) is applied between the two electrodes via the outer braid of the triaxial cable. The positive charges produced in the air cavity migrate towards the negative electrode; whereas the negative charges migrate towards the positive electrode. The charge liberated by the radiation can thus be collected and measured by the electrometer through the central conductor of the triaxial cable. The exposure, X is then defined as

$$X = M \cdot N_x , \tag{4.12}$$

where N_x is the $^{Co}60$ exposure calibration factor (R/C or R/scale division) and M (C or scale division) is the electrometer reading for the dosimeter, corrected for temperature and pressure, and uncorrected for ionization recombination[7].

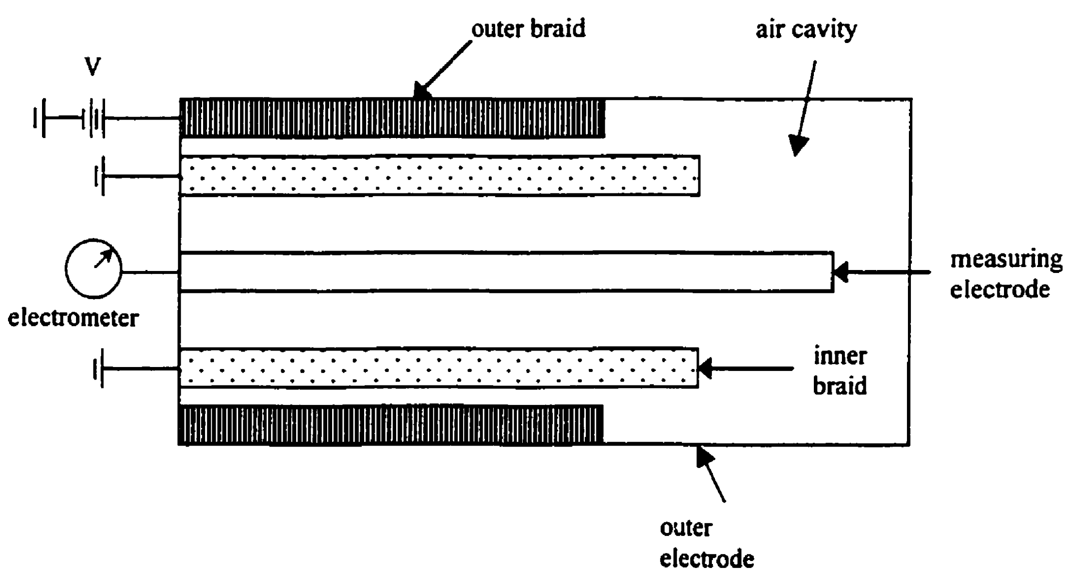

Figure 4.1: Schematic diagram of a Farmer-type chamber.[10]

4.2.5 Parallel Plate Chamber

A cross-section of a parallel plate chamber is shown in Fig. 2.4. It consists of parallel electrodes and an air cavity in the shape of a circular disk. Facing the source is the upper electrode, which is made of a thin plastic foil, coated with carbon. An electrometer is connected to the lower electrode (or collecting electrode), which is small and circular in shape, surrounded by a guard ring, and the electrode spacing is small (about 2 mm). The guard ring not only provides a uniform electric field, but it also prevents the measurement of leakage current, which originates from the high voltage electrode[11]. A very thin wall or window on the upper electrode (about 0.01 mm to 0.03 mm thick), usually made of foils of Mylar, polystyrene or mica, allows measurements to be taken without significant wall attenuation. The parallel plate chamber is used especially for surface and build-up dose measurements because the cylindrical chamber is too large.

4.3 Phantoms

Water is recommended as a standard phantom material because it closely approximates the radiation absorption and scattering properties of tissues and muscles. Another important advantage of using water as a phantom is that it is universally available with reproducible radiation properties. However, water poses a problem for film and non-waterproof chamber measurements. One solution is to use solid water (Radiation Measurements, Inc., Middleton, WI), developed by Constantinou et al.[12], which is an epoxy resin-based mixture that resembles water, but in a solid form. Other alternatives include encapsulating the chamber with a water equivalent, thin, plastic sleeve before submersion, or using waterproof chambers.

In electron dosimetry, for a phantom to be water equivalent, it must have both the same linear stopping power and linear angular scattering power as water. This can be achieved if the electron density (number of electrons per cm^3), effective atomic number, and mass density are the same. Since Compton effect is the primary mode of interaction of photon beams in the clinical energy range, the only condition that must be fulfilled is electron density equivalence. As indicated in Table 4.1, of all the phantoms available, electron solid water resembles water most closely, followed by polystyrene.

Material	***Mass density (g/cm³)***	***Electron Density Relative to Water***
Water	1	1
Polystyrene (clear)	1.045	1.012
Polystyrene (high impact, white)	1.054	1.018
Acrylic	1.18	1.147
Electron solid water (model 457)[13]	1.035	1.00

Table 4.1: Comparison of properties between different phantom materials[8].

4.4 Summary

Calorimetry, Fricke dosimetry, and standard ionization chamber are methods to determine the dose at a specific point in a phantom.

Relative dosimetry techniques only give the ratio of dose at one point in the phantom to the dose at another point. In addition, some of them, such as TLD, must be calibrated against a known radiation field. Some of the more common relative dosimeters available include film, TLD, solid state diodes and ion chambers.

Finally, the requirements of a phantom were discussed, and different types of phantom materials such as electron solid water, polystyrene and acrylic were presented. It can be shown from Table 4.1 that electron solid water best approximates water in mass density and electron density.

4.5 References

1. F.M. Khan, The Physics of Radiation Therapy, 2nd edition, Williams & Wilkins, Baltimore, Maryland, U.S.A. (1994).
2. J.S. Laughlin & S. Genna, "Calorimetry," in Radiation Dosimetry, ed. F.H. Attix & W.C. Roesch (New York: Academic Press, 1967), Vol. II, p. 389.
3. S.R. Gunn, "Radiometric calorimetry: a review," Nucl. Inst. Methods 20, 1 (1964).
4. S.R. Gunn, "Radiometric calorimetry: a review," Nucl. Inst. Methods 85, 285 (1970).
5. S.R. Gunn, "Radiometric calorimetry: a review," Nucl. Inst. Methods 135, 251 (1976).
6. International Commission on Radiation Units and Measurements (ICRU),

Radiation Dosimetry: Electron Beams with Energies Between 1 and 50 MeV, ICRU Report 35, Bethesda, Maryland (1984).

7. AAPM, RTC Task Group 21, "A protocol for the determination of absorbed dose from high energy photon and electron beams," Med. Phys. 10, 741-771 (1983).
8. F.M. Khan et al., "Clinical electron-beam dosimetry: Report of AAPM Radiation Therapy Committee Task Group No. 25," Med. Phys. 18, 73-109 (1991).
9. F.T. Farmer, "A substandard x-ray dose-meter," Br. J. Radiol. 28, 304 (1955).
10. D. Gelinas, Commissioning a dynamic multileaf collimator on a linear accelerator, M.Sc. Thesis, McGill University, Montreal, Canada, 1999.
11. F.H. Attix, Introduction to Radiological Physics and Radiation Dosimetry, John Wiley and Sons, Inc., New York, U.S.A. (1986).
12. C. Constantinou, F.H. Attix & B.R. Paliwal, "A solid phantom material for radiotherapy x-ray and γ-ray beam calibrations," Med. Phys. 9, 436 (1982).
13. C. Constantinou, private communication.

CHAPTER 5: METHODS AND MATERIALS

This chapter explains the methods by which data was collected, and the equipment utilized throughout the study. PDD measurements can be made using various dosimeters. The cylindrical ion chamber has been used for most part of this work, and other detectors such as diode, Attix plane-parallel ionization chamber, and film were used as well. All four of these methods were tested and inter-compared, and the procedures by which beam characteristics (PDD, profiles and outputs) were measured are discussed. Both large and small field sizes were studied, although the focus of this research is on the beam parameters of small field sizes.

5.1 PDD measurements using various dosimeters

Measurements were performed on the Clinac 18 with a source-surface distance (SSD) of 100 cm. Various dosimeters were used to compare the PDDs of electron beams with nominal energies of 9, 12, 15 and 18 MeV, for a 15x15 cm^2 cone. Measurements were taken with both positive and negative polarities when using the cylindrical ion chamber and the Attix parallel-plate chamber.

5.1.1 Ion chamber

The measuring device used was a waterproof ion chamber (0.03 cm^3, IC-04, Wellhöfer Dosimetrie), and a reference chamber (IC-10, Wellhöfer Dosimetrie) was used to compensate for the fluctuations of a linac's output over time. The ionization reading was given as the ratio of the two signals. TG-25[1] recommends that the effective point of measurement of a cylindrical ionization chamber should be at a distance equal to half the radius of the sensitive volume upstream for all depths and energies. Since the radius of the chamber is 2 mm, the point of measurement was shifted 1 mm towards the source from the center of the chamber. A high potential (typically 300 V) was applied between the chamber electrodes, and a 3D water phantom was used (WP 700, Wellhöfer Dosimetrie, Schwarzenbruk, Germany). The location of the ion chamber can be determined precisely in the 50 x 50 x 50 cm^3 water phantom. The ion chamber was scanned vertically along the central axis of the electron beam, collecting measurements at 0.1 cm intervals. Data was initially collected as ionization readings, and was consequently converted to dose by multiplying the raw ionization data by the corresponding stopping power values for the specific energy and depth, as shown in Eq. 4.10.

5.1.2 Diode

A p-type silicon diode (Scanditronix, Uppsala, Sweden) was used to measure PDD in the 3D water phantom. From the manufacturer specifications, the effective point of measurement is displaced from the detector front surface by 0.45 ± 0.1 mm. However, according to TG-25[1], the depth dose results from a diode should be forced to agree with the PDD results obtained with an ion chamber. Hence, following TG-25[1] protocol's recommendations, the diode PDD curve was shifted accordingly in order to match the ion chamber PDD curve. The setup of this experiment was similar to the setup with the ion chamber.

5.1.3 Attix plane-parallel ionization chamber

The third method of measuring PDD was using an Attix plane-parallel ionization chamber (Model 449, Gammex/RMI, Middleton, WI), embedded in solid water (Radiation Measurements, Inc., Middleton, WI). Loose sheets of solid water of thicknesses varying from 2 mm to 6 cm were used to vary the depth. Measurements were taken every 2 mm in the buildup and d_{max} regions, and every 5 mm elsewhere.

5.1.4 Film Calibration

Therapy verification film (XV2, Eastman Kodak Company, Rochester, NY) used for measurements must be calibrated prior to use. Films were placed in a solid water phantom, perpendicular to the central axis at the respective d_{max}. For each nominal electron beam energy, films were irradiated to 10, 30, 50, 75 and 100 cGy. The films were developed by an automatic processor (Kodak RP X-OMAT, M6B) at the same time to minimize the variations in optical density readings due to different processing conditions. An unexposed film was also processed to serve as the background (base plus fog) signal. The net density of each film (given by the difference in optical densities of the exposed and unexposed films) was read using the densitometer, which is able to read optical densities with signals up to 4.0. The densitometer light source is a pulsed light beam in the infrared region, with a wavelength of 950 nm, and the diameter of the light aperture is 0.8 mm. In addition, a light detector, formed by 4 diodes, measures the light intensity transmitted through the film[2]. Finally, a calibration curve given by the optical density vs. dose was plotted. A typical calibration curve is shown below in Fig. 5.1. The optical density of the film is proportional to the dose for doses equal to or less than 30 cGy for all energies under investigation. Therefore, the films were irradiated for only

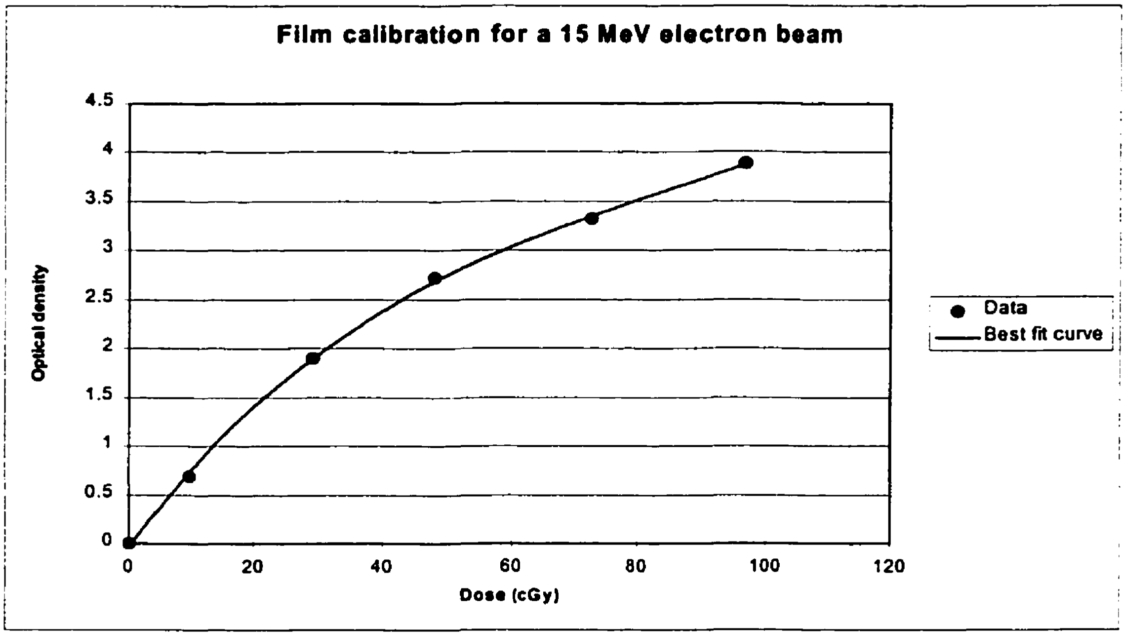

20 cGy when taking PDD measurements in order to be in the linear region of the film.

Figure 5.1: Film calibration (XV-2) curve for a 15 MeV electron beam.

5.1.5 Film measurements

Measurements of PDD with film were carried out by removing the film from the film envelope in the dark room, sandwiching it between two slabs of solid water, with the edges sealed using black vinyl tape. The film was placed parallel to the electron beam, as shown in Fig. 5.2, and additional solid water was added on both sides until there was at least 5 cm of excess phantom on each side of the field. Finally, the film was aligned to the surface of the phantom and the entire assembly was tightened with a clamp to prevent artifacts which might arise due to air pockets between the film and the phantom[3,4]. For each energy, the films were irradiated to 20 cGy, and were batch processed. The densitometer was used to scan the film along the central axis, and data was collected at 0.1 cm intervals.

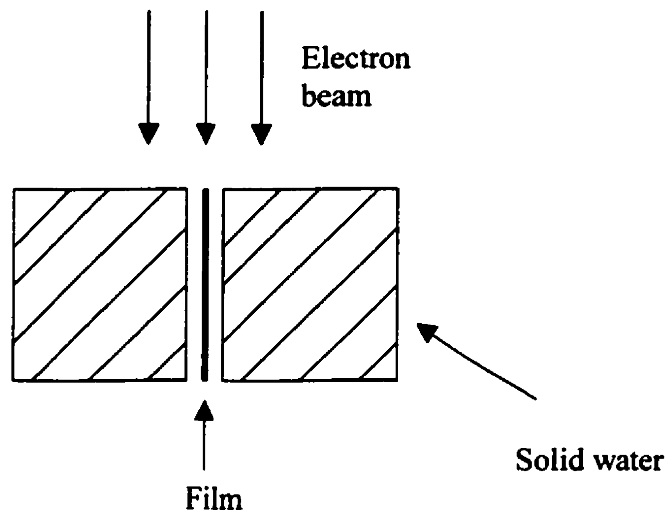

Figure 5.2: PDD measurement setup with film and solid water.

5.2 *Comparison of PDD results using different dosimeters*

The PDD curves obtained with ion chamber, diode, Attix parallel plate chamber, and film are shown in Fig. 5.3 to Fig. 5.6. Even though the measurements with the ion chamber and diode were performed in water, and the Attix chamber and film were measured with solid water, depth-scaling corrections are not necessary[1]. The physical characteristics of solid water materials are equivalent to water, with the recommended effective densities of both equal to 1.00. For all energies, the data obtained with the ion chamber and diode agree very well. However, the results with the Attix chamber are often shifted slightly to the right, whereas the results with the film are shifted to the left. While most of the dosimeters correlate quite well at the buildup and d_{max} regions, the correlation decreases at greater depths. At d_{50}, the disagreements between film and ion chamber/diode are 0.2 cm, 0.1 cm, 0.2 cm, 0.25 cm. (For nominal energies of 9 MeV, 12 MeV, 15 MeV, 18 MeV respectively). Similarly, the disagreements between Attix and ion chamber/diode are 0.06 cm, 0.08 cm, 0.1 cm, 0.1 cm. Thus, if the ion chamber measurement is considered the standard, then the maximum deviation for the Attix chamber is 0.1 cm.

This deviation is acceptable within experimental error; however, the film's maximum deviation is 0.25 cm, which is not acceptable even considering experimental error. Another method of comparing PDD data is to compare the slope steepness or the dose fall-off. It is defined as the increment between 2 isodose levels (for example, 20%-70%) divided by the distance (in mm) between them[4]. For the 9 MeV electron beam, the dose fall-off for the ion chamber, diode, Attix chamber, and film are 58.8, 58.8, 59.5, and 58.8 %/mm respectively. Similarly, for the 12 MeV electron beam, the dose fall off are 4.5, 4.3, 4.3, and 4.5 %/mm. For the 15 MeV electron beam, all the dosimeters measure the same gradient of 3.6 %/mm. Finally, for the 18 MeV electron beam, they measure 2.9, 2.7, 2.8, and 3.0 %/mm respectively.

The experimental error in PDD is determined by the difference between the ionization results obtained with both positive and negative polarities. Since they agree within 1%, the error in PDD can be estimated to be equal to ± 0.5 %. The limited accuracy in positioning the dosimeter at a known depth contributes error in depth, and it can be estimated to be equal to about ± 0.5 mm.

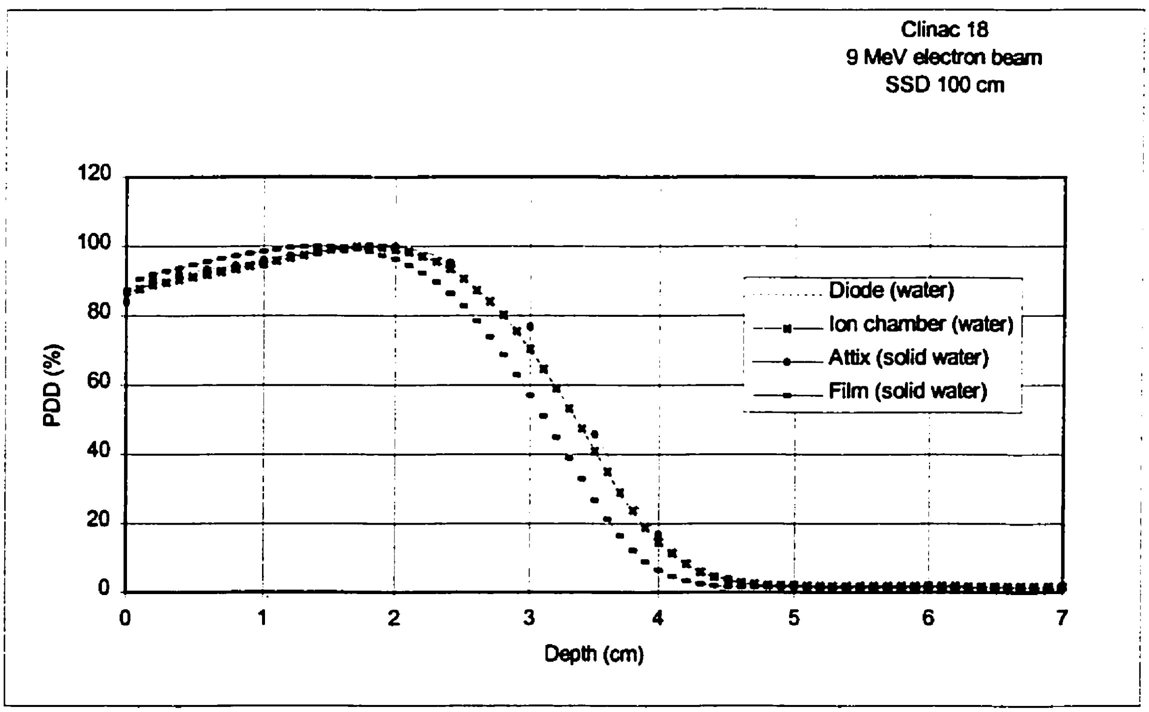

Figure 5.3: PDD measurements using different dosimeters for a CL 18 (9 MeV) electron beam with a 15x15 cm^2 cone.

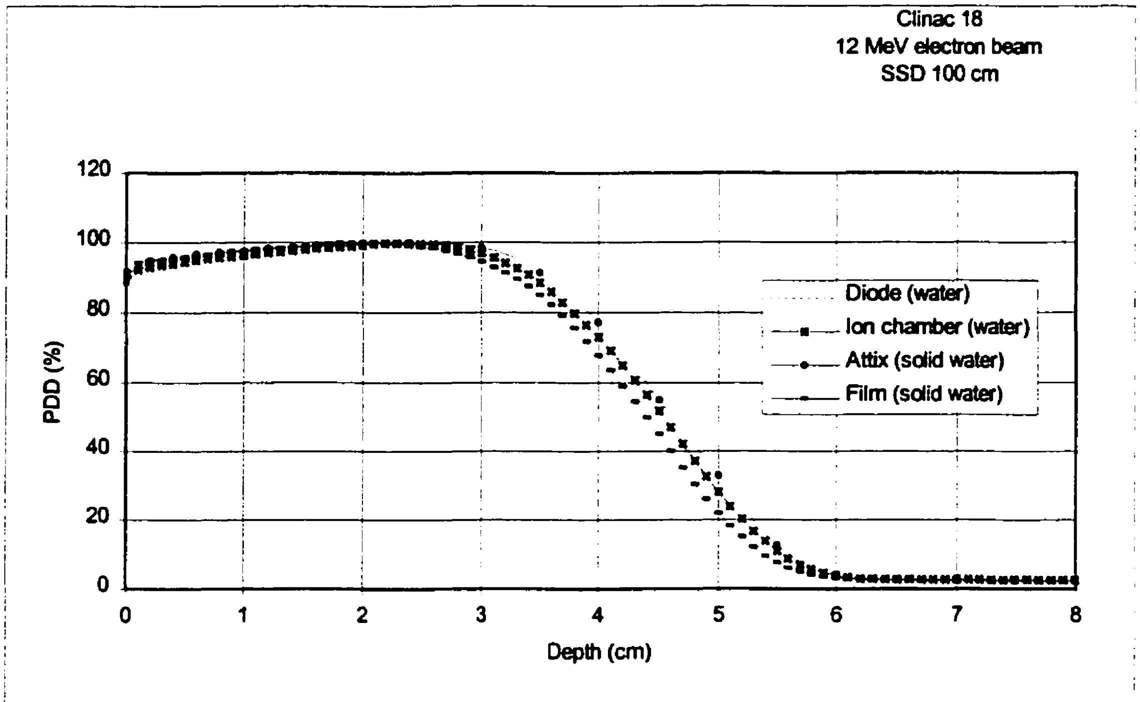

Figure 5.4: PDD measurements using different dosimeters for a CL 18 (12 MeV) electron beam with a $15x15\ cm^2$ cone.

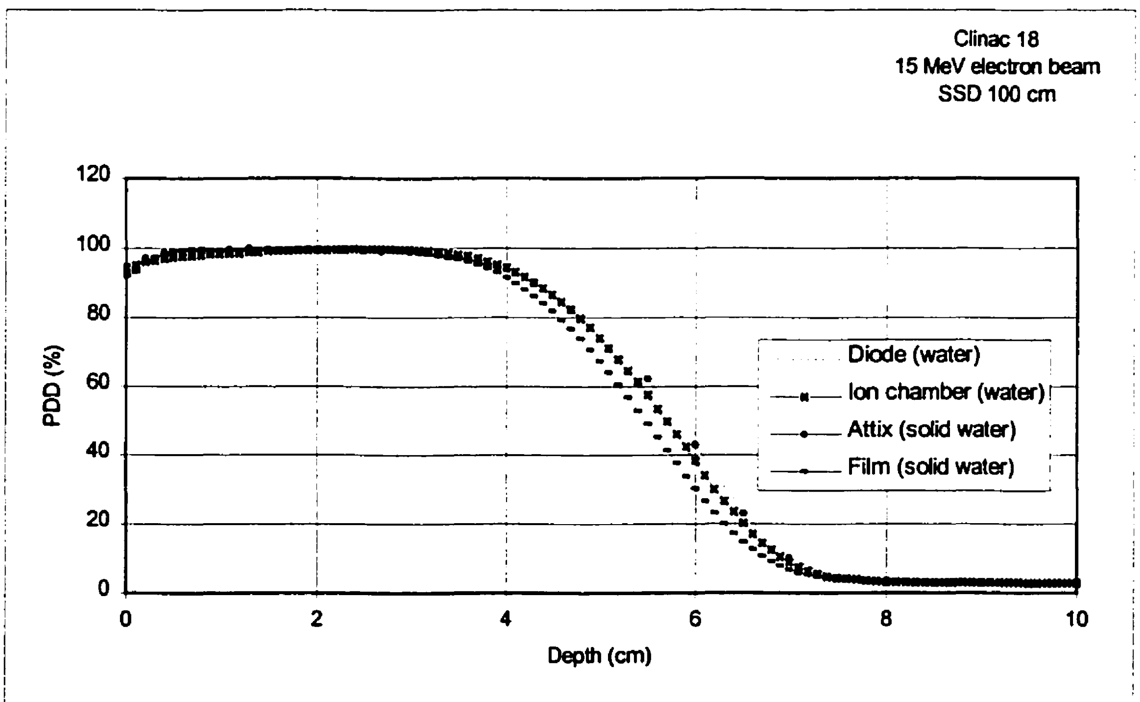

Figure 5.5: PDD measurements using different dosimeters for a CL 18 (15 MeV) electron beam with a $15x15\ cm^2$ cone.

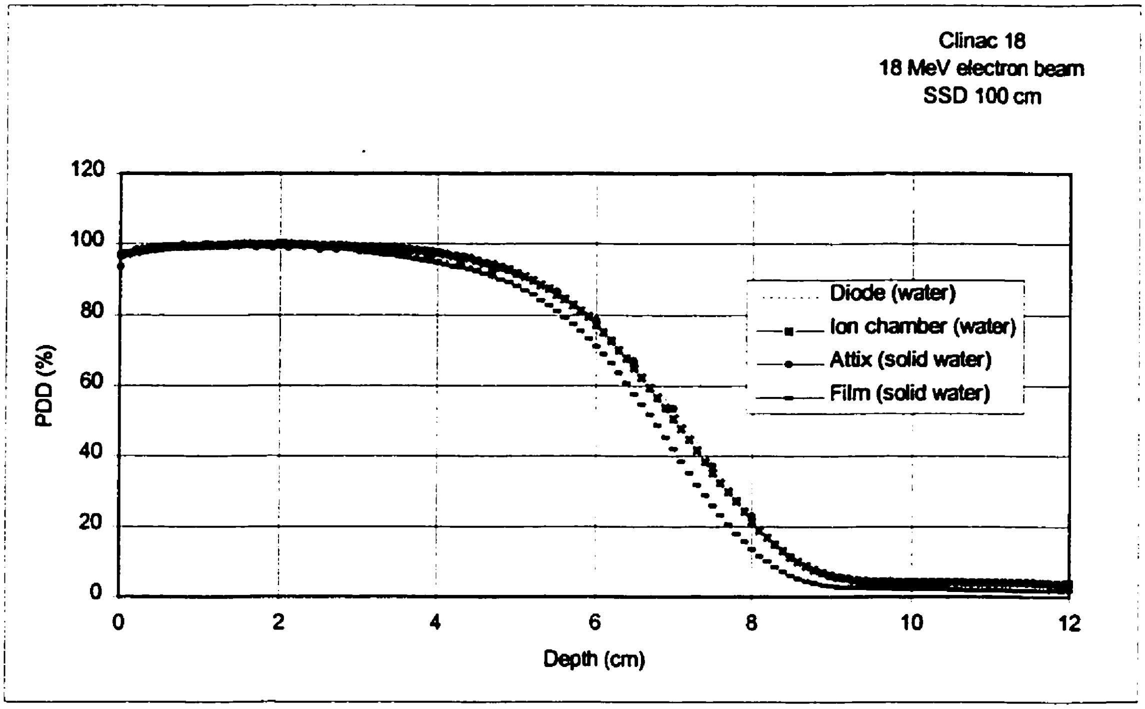

Figure 5.6: PDD measurements using different dosimeters for a CL 18 (18 MeV) electron beam with a 15x15 cm^2 cone.

5.3 Electron cutouts

Cutouts are used to shape the radiation field to the tumor, hence minimizing the dose to the surrounding tissues. The cutouts used in this work are made of cerrobend, which is a low melting temperature alloy containing bismuth, lead, tin and cadmium (50.0%, 26.7%, 13.3% and 10.0% by weight respectively), and are placed at the end of the applicator. The required shielding thickness of the cutouts should be approximately equal to the maximum range of the highest electron energy beam available in cerrobend. Therefore, each has a thickness of 1.6 cm, which will reduce the transmitted dose to a practical minimum (<10%). The cutouts also vary in shapes and sizes, the circular cutouts range from 1 cm to 6 cm in diameter, in increments of 1 cm, and the rectangular cutouts measure 10x1 cm^2, 10x2 cm^2, 10x3 cm^2, and 10x4 cm^2. Finally, for the CL 2300 C/D, a 4x4 cm^2 cutout is also used.

5.4 Beam parameters measured with cutouts

Most of the measurements of beam parameters were taken with an ion chamber as the dosimeter, although some profiles for very small fields were measured with film, due to limitations imposed by the dimensions of the ion chamber. The phantom used was the Wellhöfer water phantom. The beam characteristics under investigation include PDD, profiles and outputs, and they were determined for various field sizes (regular electron cones and small cutouts).

The method for measuring PDD has already been discussed in section 5.2.1. The ion chamber was scanned vertically along the central axis in water, collecting data at 0.1 cm intervals. The curve obtained was smoothed and normalized to 100%. The ionization curve was converted to depth dose curve, and shifted by a distance equal to half the radius of the sensitive volume upstream, to account for the displacement of the point of measurement[1].

The setup for measuring profiles was similar to the one used for PDD measurements. However, the ion chamber was scanned perpendicularly to the electron beam. A profile was obtained at 6 different depths for each field size: $d_{surface}$ (0.05 cm), d_{max} ,d_{90}, d_{80}, d_{50} and d_{20}. The depths were determined from the PDD curve obtained previously. Also, for each depth, data was taken for both directions, ie. in-plane and cross-plane.

Finally, the relative output factor was measured by placing the ion chamber at the specific d_{max} of the field size and energy under investigation. The charge accumulated during 100 MU of irradiation was multiplied by the stopping power at the given depth and energy, and normalized to the result obtained with the 10x10 cm^2 electron cone using the same technique. Hence, the relative output factor (*ROF*) is defined as

$$ROF(F) = \frac{Dose/100MU\,[F, d_{\max}(F)]}{Dose/100MU\,[10x10, d_{\max}(10x10)]}, \tag{5.1}$$

where *F* is the field size under investigation[1].

5.5 Summary

This chapter described the procedures involved in comparing the PDDs measured with 4 different dosimeters: ion chamber, diode, Attix plane-parallel chamber, and film. This chapter also discussed the setup involved for measuring various beam characteristics, such as PDD, profiles and relative output measurements with various field sizes. This thesis focuses on the correlation of such characteristics with cutouts, and the presentation of results and interpretation will be covered in chapter 6.

5.6 References

1. F.M. Kahn, K.P. Doppke, K.R. Hogstrom, G.J. Kutcher, R. Nath, S.C. Prasad, J.A. Purdy, M. Rozenfield & B.L. Werner, "Clinical electron-beam dosimetry: Report of AAPM Radiation Therapy Committee Task Group No. 25," Med Phys. 18, 73-109 (1991).
2. Film Densitometer WP 102 Operating Instructions, 1992, Wellhöfer Dosimetrie, Schwarzenbruk, Germany.
3. J. Dutreix & A. Dutreix, "Film dosimetry of high energy electrons," Ann. N.Y. Acad. Sci. 161, 33-43 (1969).
4. S.C. Klevenhagen, Physics and Dosimetry of Therapy Electron Beams, Medical Physics Publishing, Madison, Wisconsin, U.S.A. (1993).

CHAPTER 6: RESULTS AND DISCUSSION

The methods for measuring PDDs, profiles and outputs have been discussed in chapter 5. Beam parameters for both large and small field sizes have been measured, however, the focus of this research is on the effects of small field sizes on clinically relevant dosimetric parameters. Selected results with interpretation of the most representative data are presented and discussed in this chapter.

6.1 Percent depth dose

PDDs were measured using cutouts having rectangular, circular, and square shapes. The dimensions of the rectangular cutouts were 10x1, 10x2, 10x3, and 10x4 cm^2. The diameters of the circular cutouts were 1, 2, 3, 4, 5, and 6 cm, and a square cutout of 4x4 cm^2 was also used. The PDDs were measured for electron energies ranging from 9 to 18 MeV on the Clinac 18, and from 6 to 22 MeV on the Clinac 2300 C/D.

6.1.1 PDD dependence on energy

Fig. 6.1 shows a series of PDD curves obtained using the 4 cm diameter cutout, for electron beam energies ranging from 6 to 22 MeV. The shapes of the PDD curves are characteristic of clinical electron beams. Each PDD displays a high surface dose, a build up region, a broad dose maximum, a sharp dose fall-off, and a bremsstrahlung tail. Similar results were obtained when data with a 10x2 cm^2 cutout was measured using the CL 18 linear accelerator. These results are illustrated in Fig. 6.2. Based on these data sets, the following conclusions can be made. First of all, the surface dose increases with the energy of the electron beam. In particular, the surface dose increases from approximately 80% to 90% with energy for circular cutouts, whereas it increases from approximately 90% to 95% with energy for rectangular cutouts. Moreover, the therapeutic depth (d_{90}) also increases with energy. D_{90} increases from approximately 2 to

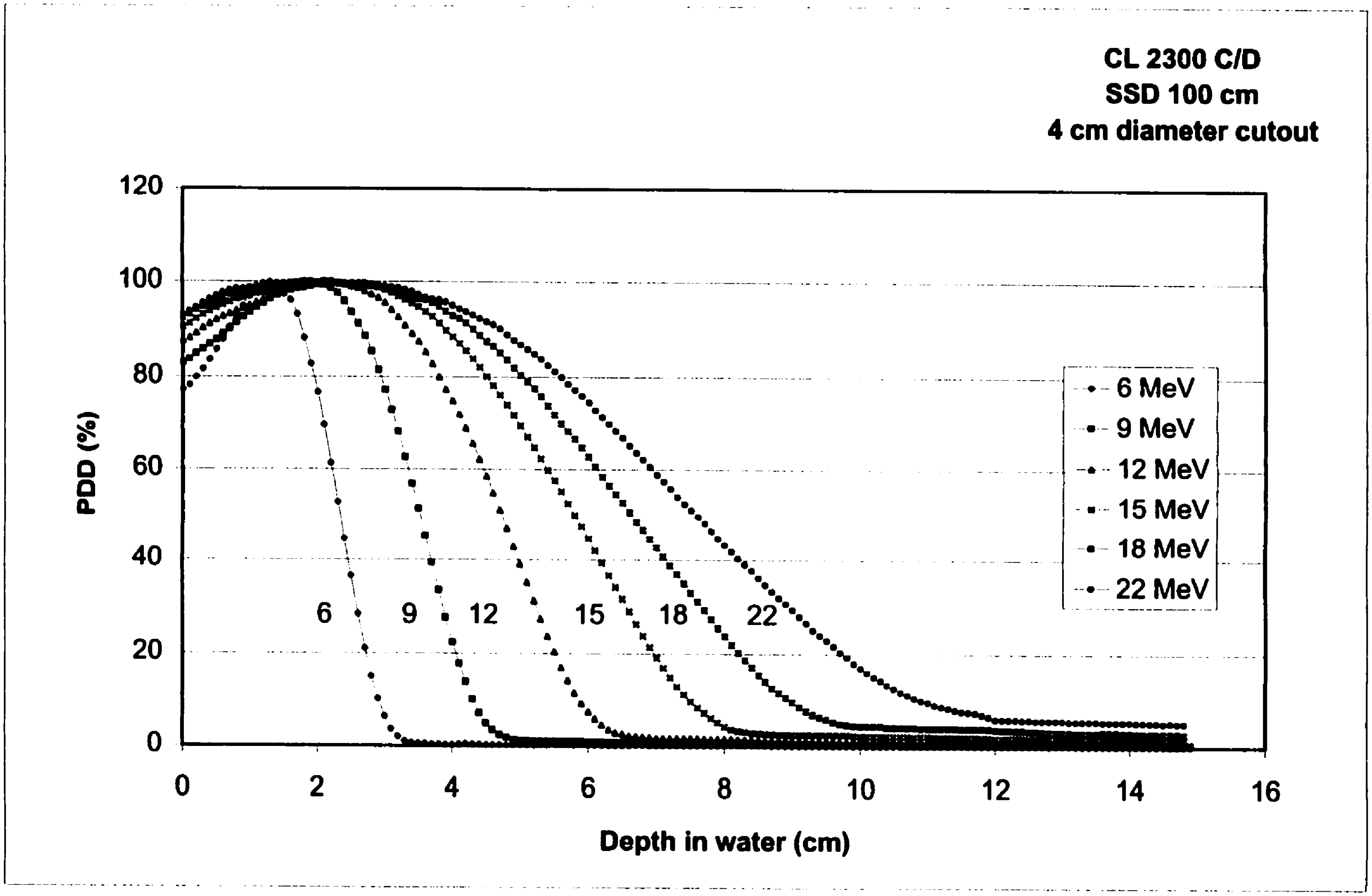

Figure 6.1: PDDs measured with a 4 cm diameter circular cutout for various electron energy beams on a CL 2300 C/D.

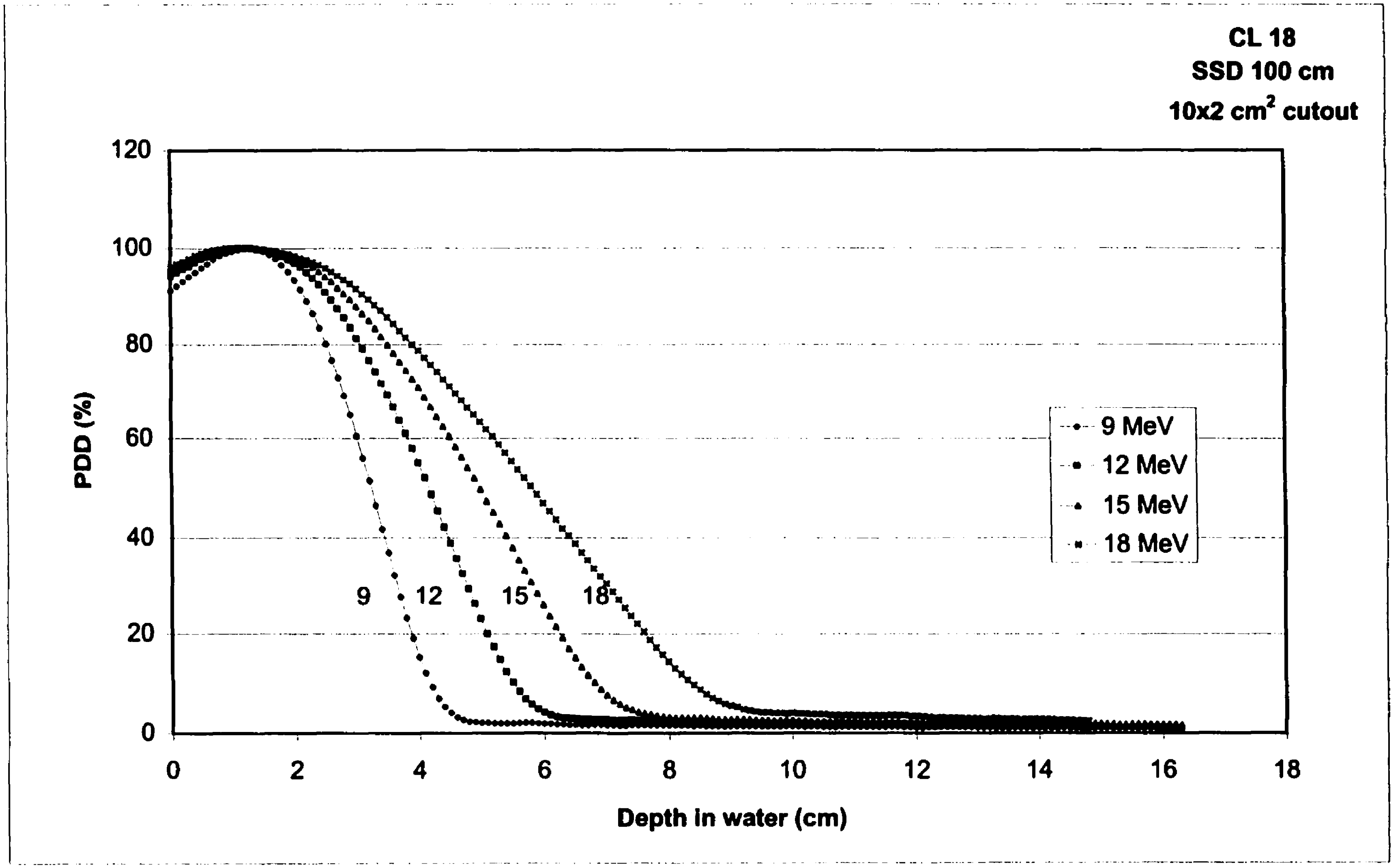

Figure 6.2: PDDs measured with a 10x2 cm^2 rectangular cutout for various electron energy beams on a CL 18.

5 cm with energy for circular cutouts, whereas it increases from 2 to 3.5 cm for rectangular cutouts. Finally, the bremsstrahlung dose increases from about 1% for a low energy beam to about 5% for a high energy beam. These trends are in agreement with TG-25[1].

6.1.2 PDD dependence on field size

Fig. 6.3 through Fig. 6.8 display a series of PDDs obtained using the CL 2300 C/D for circular cutouts of diameters 1, 2, 3, 4, 5, and 6 cm. For all energies, it was found that as the field size decreases, the surface dose increases from 80% to 100% for low energy beams, and from 90% to 95% for high energy beams. In addition, decreasing field size also resulted in the shifting of d_{max} and d_{80} towards the surface. Finally, the practical range of the electron beam (R_p) remains constant, as it is a function of the beam energy and photon contamination. These trends are consistent for all electron beams investigated during this study, and they are also in agreement with various publications such as McGhee et al.[2], who reported a "compression" of central axis depth dose when cutouts are used. Similar trends were also reported for different types of linear accelerators (Siemens Mevatron XX[3], Siemens KD2[4], Siemens MD2[5], Siemens Mevatron 80[5], Therac 20/Saturne[6]) and other detectors used (diode, ion chamber, film[2,3,5-7]).

An understanding of the relationship between PDD and field size can be achieved with the introduction of the concept of side-scatter equilibrium. Fig. 6.9a shows that the electrons passing through an area of ΔA will undergo scatter and miss the target ΔB[8]. However, the number of electrons that reach the target is not greatly reduced since for each electron that scatters away from the target area, there is another incident electron that will scatter into ΔB following a similar path (Fig. 6.9b). When an electron beam field size is large enough, such that more than 99% of the electrons reach the point of interest, side scatter equilibrium is achieved.

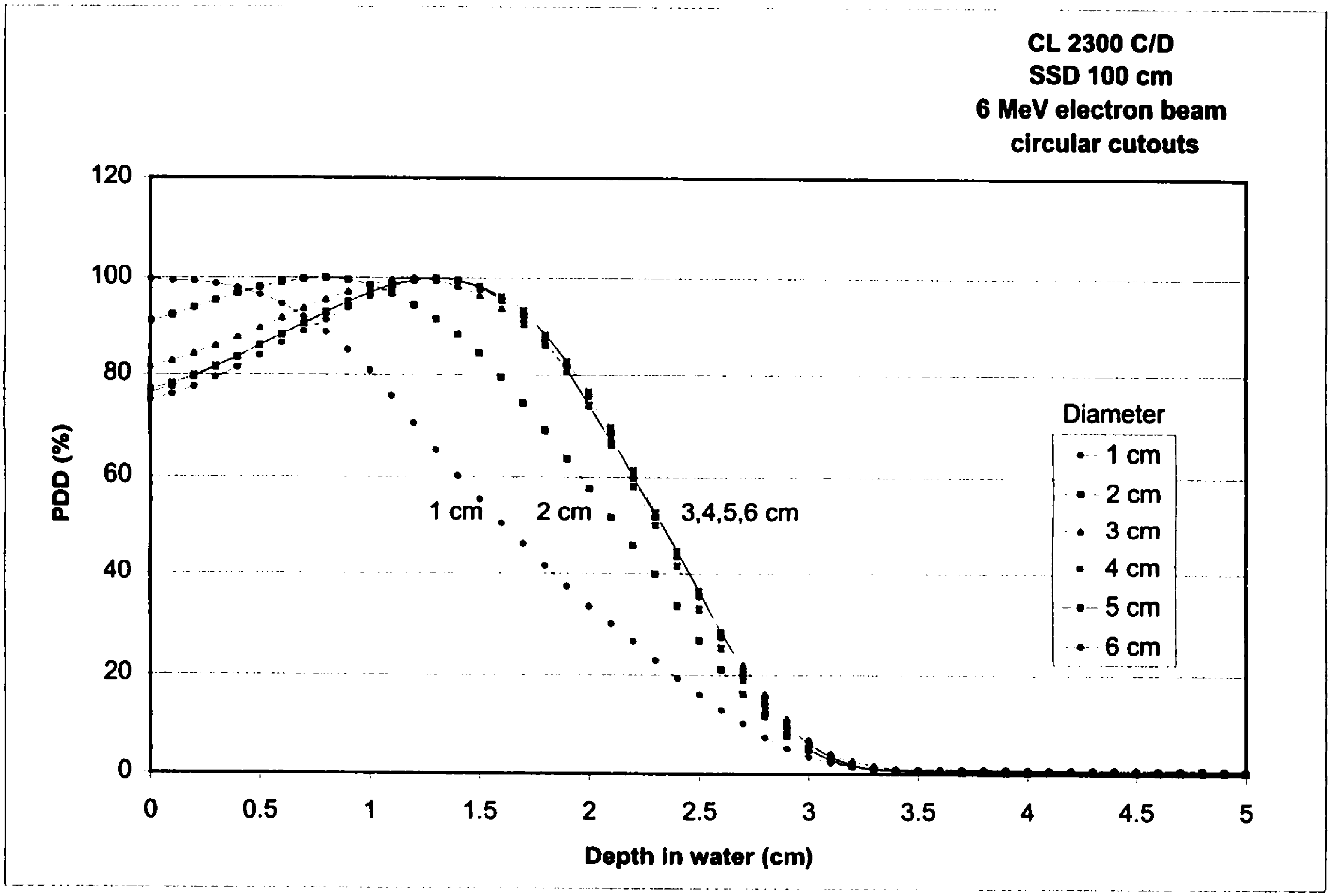

Figure 6.3: PDDs measured with circular cutouts of various diameters for a 6 MeV electron beam on a CL 2300 C/D.

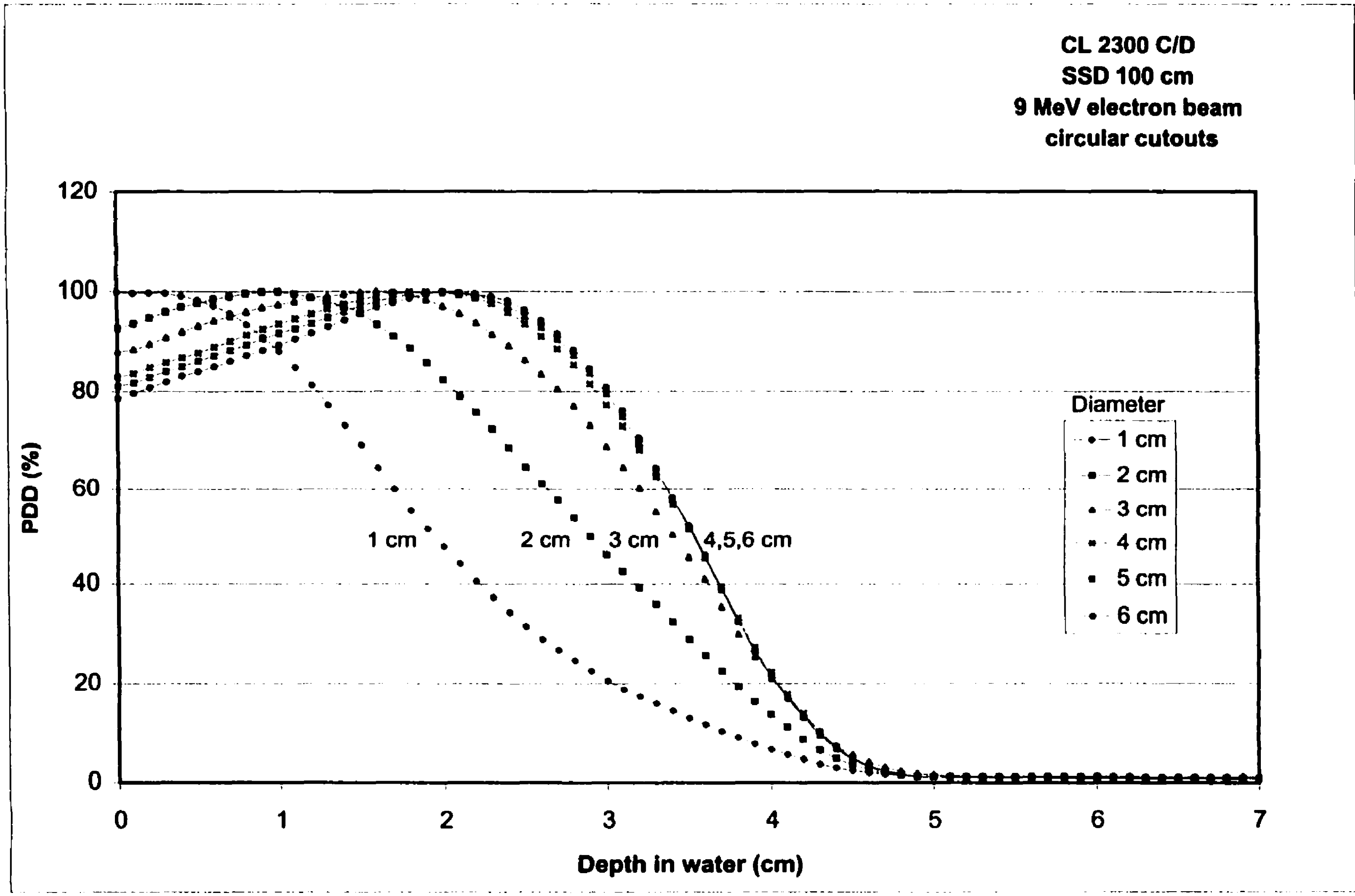

Figure 6.4: PDDs measured with circular cutouts of various diameters for a 9 MeV electron beam on a CL 2300 C/D.

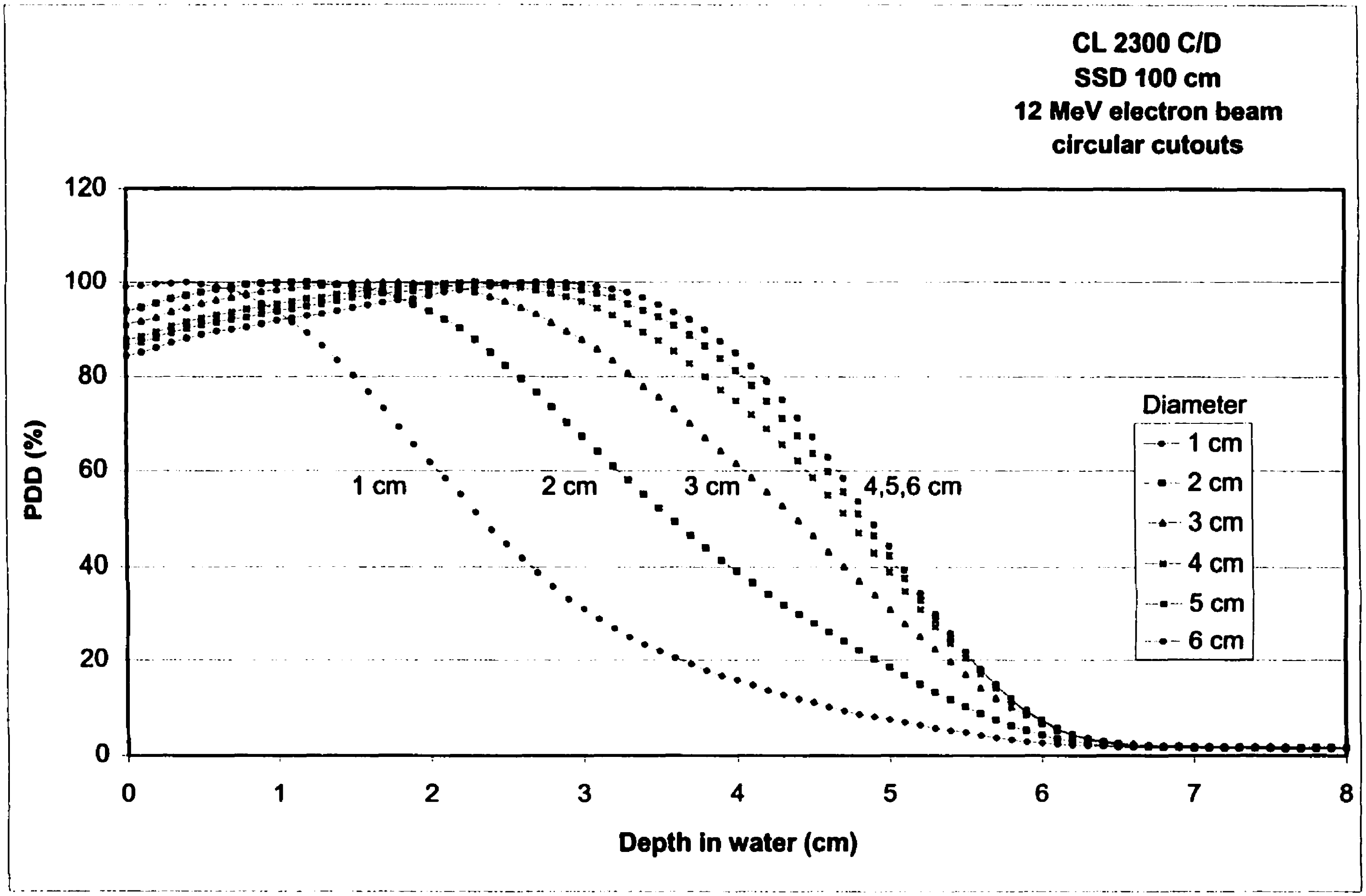

Figure 6.5: PDDs measured with circular cutouts of various diameters for a 12 MeV electron beam on a CL 2300 C/D.

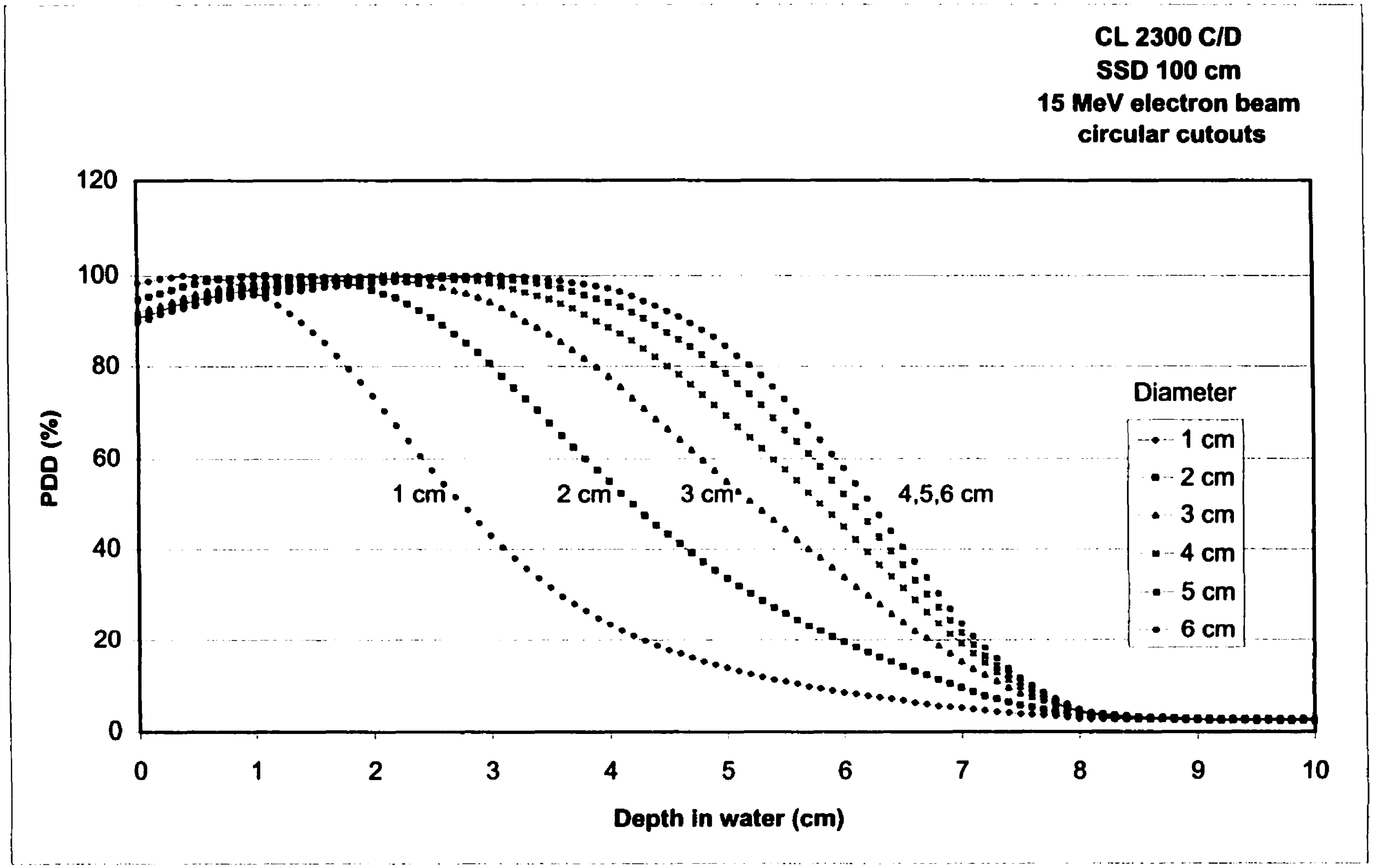

Figure 6.6: PDDs measured with circular cutouts of various diameters for a 15 MeV electron beam on a CL 2300 C/D.

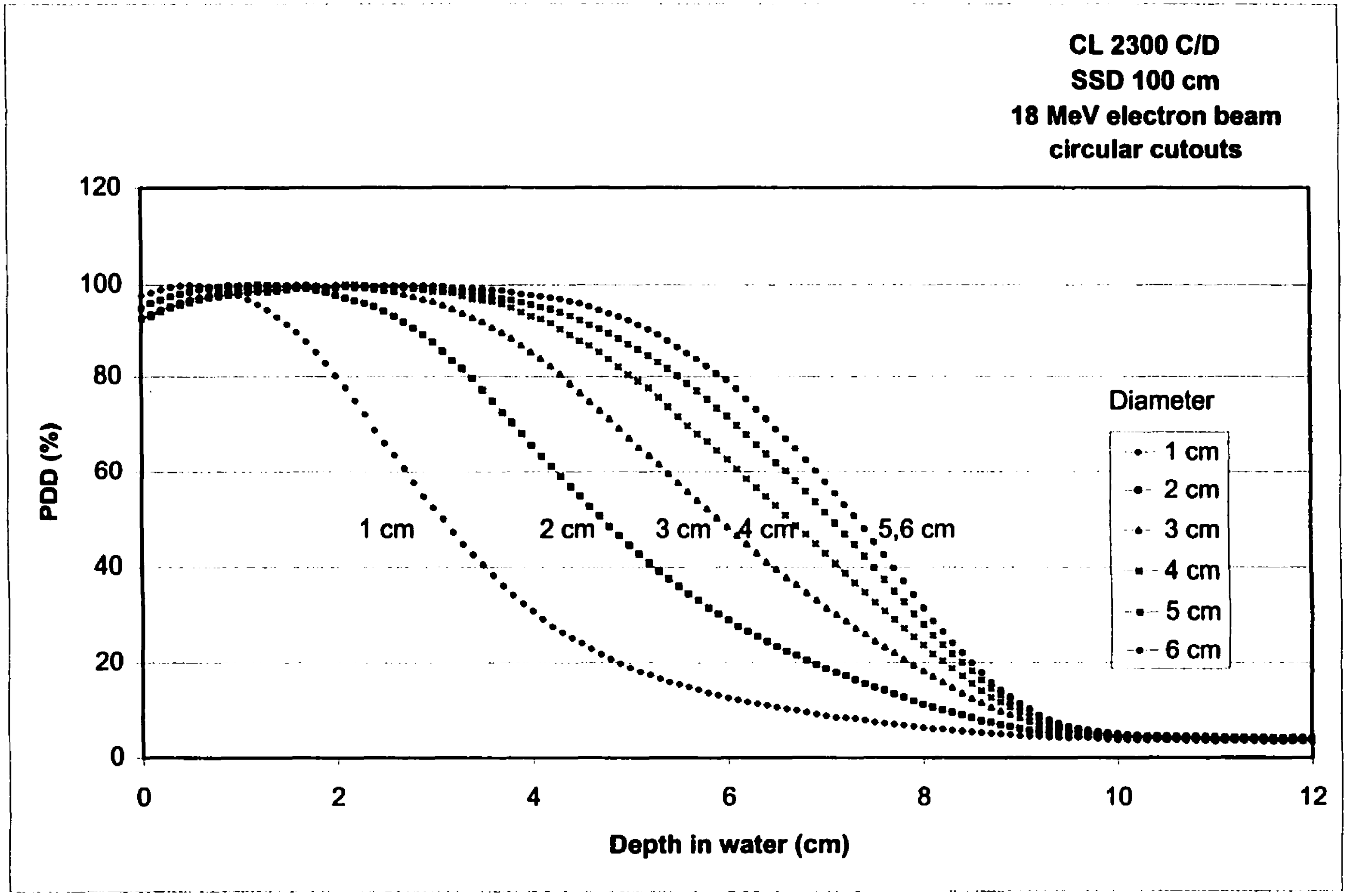

Figure 6.7: PDDs measured with circular cutouts of various diameters for a 18 MeV electron beam on a CL 2300 C/D.

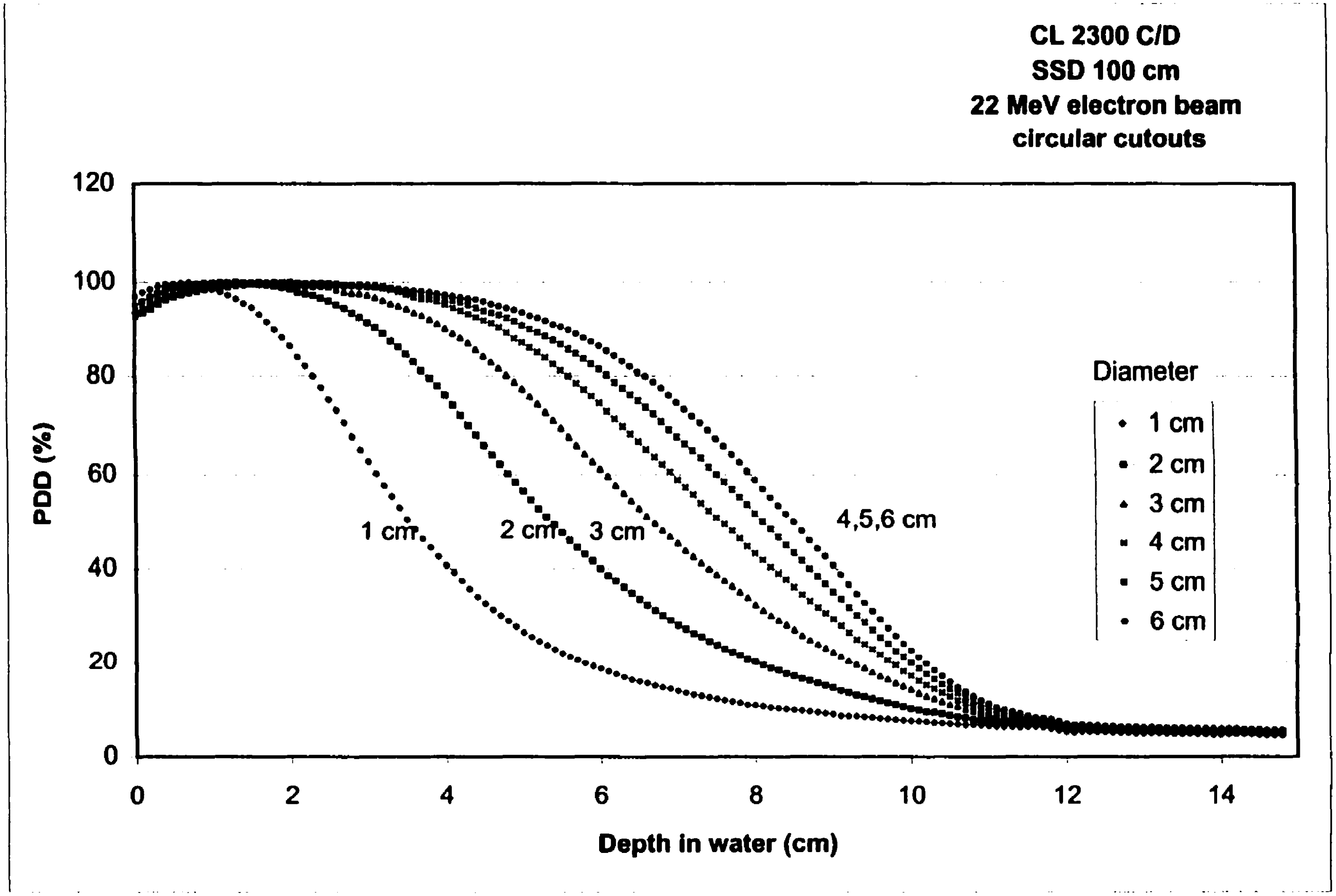

Figure 6.8: PDDs measured with circular cutouts of various diameters for a 22 MeV electron beam on a CL 2300 C/D.

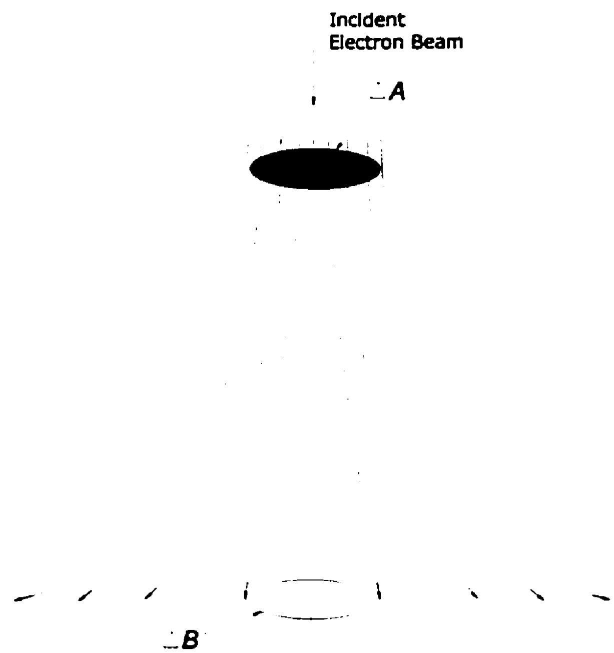

Figure 6.9a: Diagram demonstrating outscatter.

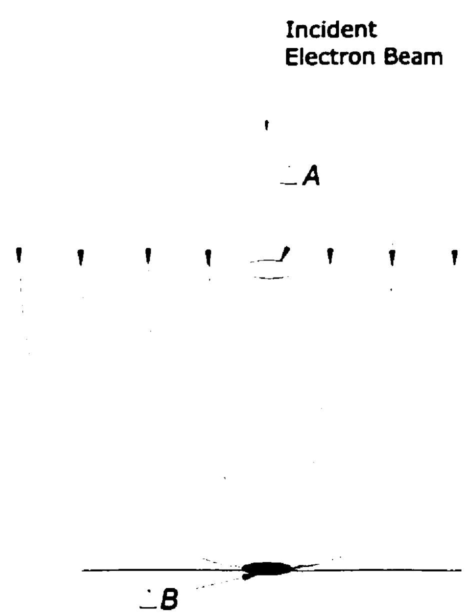

Figure 6.9b: Diagram demonstrating inscatter.

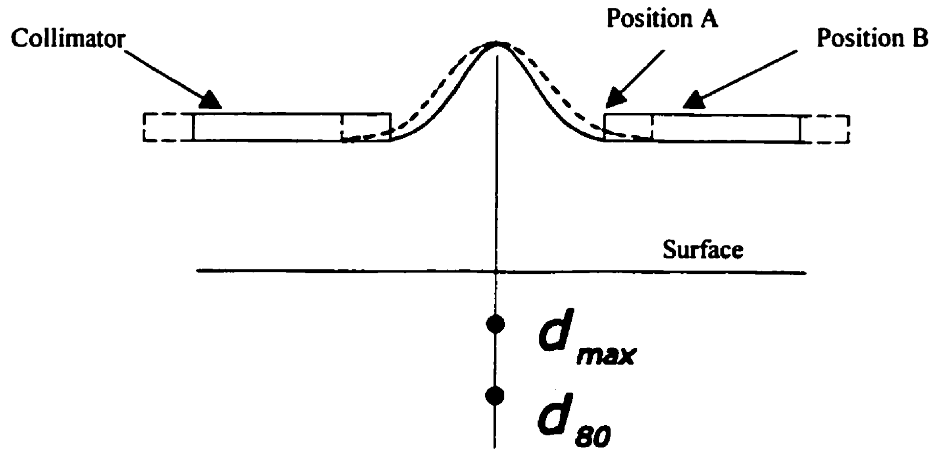

Figure 6.10: Probability functions of electrons at the level of the collimator that will reach the points of d_{max} and d_{80}.

The solid and dashed curves in Fig. 6.10 represent the probability distributions of electrons at the level of the collimator that will reach the points of d_{max} and d_{80} respectively. The functions are Gaussian in shape, and they result from the scattering of electrons in both the air and in the phantom. For the reference geometry (standard field size and SSD), when the collimator is at the position indicated by the solid line (position A), all electrons are able to reach the point of d_{max}. The dashed curve represents the distribution of electrons reaching the point of d_{80} when the collimator is opened until it is at the dotted position shown in the diagram (position B). The curve is broader due to additional Coulomb scattering in the phantom. As the collimator closes, the point d_{80} is affected first because it is at a greater depth. It will lose its side-scatter equilibrium, resulting in a decrease in depth dose and a shift of d_{80}, followed by d_{max}, toward the surface. Thus, the PDD at a specific depth will decrease as the field size decreases.

Since lateral equilibrium is not achieved with small field sizes as explained earlier, PDD must be predicted or measured on an individual basis. Another objective of this study is to investigate a rule of thumb for the clinic which estimates the limiting field size, above which individual measurements are not necessary. ICRU 21[9] states that the central-axis depth-dose curve does not significantly change if the field dimension (or diameter) is greater than the electron practical range (R_p), which is approximately one half the nominal energy of the electron beam. Therefore, a 6 MeV electron beam will have an R_p

value of about 3 cm. We would expect the depth dose to be independent of field size for a diameter or field dimension greater than 3 cm. The data presented in Fig. 6.3 to Fig. 6.8 confirms this notion. For example, when using a 6 MeV beam, we would expect the PDDs to be consistent for diameters larger than 3 cm, based on the expected relationship, and this is confirmed by the data shown in Fig. 6.3. The value of d_{80} of a 6 MeV electron beam, according to Fig. 6.11, remains constant at approximately 1.93 cm for cutouts with diameters larger than 3 cm. The value of d_{80} deviates by more than 2% from the equilibrium value when the diameter of the cutout is less than about 3 cm. Similarly for the 9 MeV electron beam, where R_p has a value of about 4.5 cm, d_{80} has a constant value of 3 cm for cutouts with diameters greater than 4 cm (Fig. 6.11). It has a deviation of more than 2% when the diameter of the cutout is less than 4 cm. Similar conclusions can be drawn from the measurements taken with the CL 18. For the 9 MeV electron beam, d_{80} deviates from the equilibrium value of 2.9 cm by more than 2% when the diameter of the cutout is less than 4.4 cm. These results agree with the guideline given by ICRU 21. It is also evident from Fig. 6.3 to Fig. 6.8 that the dependence of PDD on field size is greater when higher energy beams are used. Accordingly, the various PDDs for different cutout sizes become more distinct with higher energy beams.

6.1.3 D_{max} dependence on field size

It was found that the depth of d_{max} decreases as the field size is decreased. The depth of d_{max} increases with field size, until it reaches a constant value when side-scatter equilibrium is achieved. Beyond this point, the field size no longer has any influence on d_{max}. Fig. 6.12 illustrates the relationship between d_{max} and cutout size for various electron beams on a CL 2300 C/D. For the 9 MeV electron beam, d_{max} increases from approximately 0.3 cm for a 1 cm diameter cutout, to approximately 2 cm for cutouts of 5 and 6 cm diameter. The error associated with d_{max} can be substantial (up to ± 1 cm), and it is governed by the precision in determining d_{max} from a PDD curve. For lower energy beams, the d_{max} is often sharply peaked and easy to determine, and therefore have smaller errors. However, the PDD is almost flat near the d_{max} region for higher energy beams, resulting in larger errors. Therefore, we will investigate the dependence of d_{80} and d_{50} on field size instead.

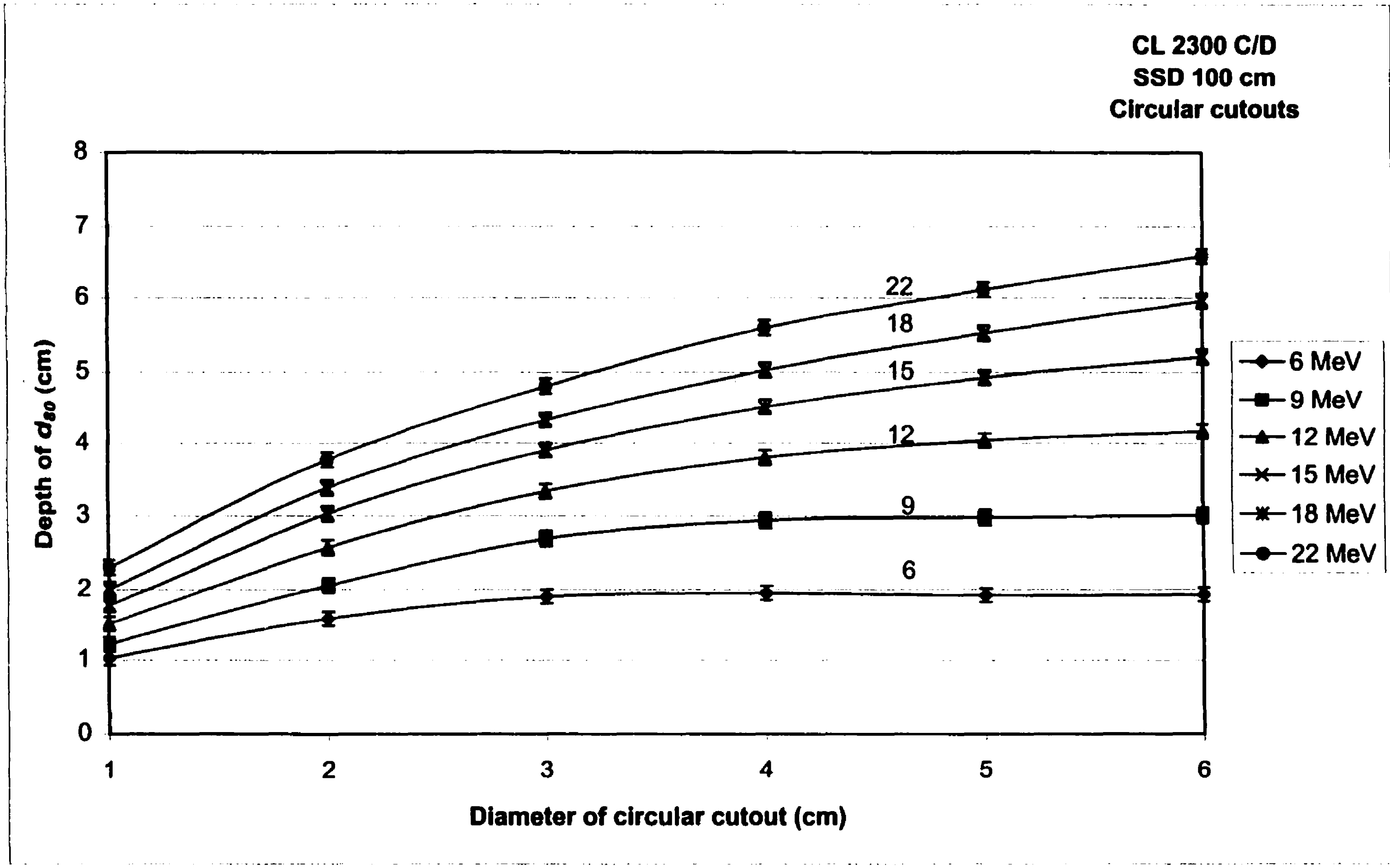

Figure 6.11: The relationship between d_{80} and field size for various electron energy beams on a CL 2300 C/D.

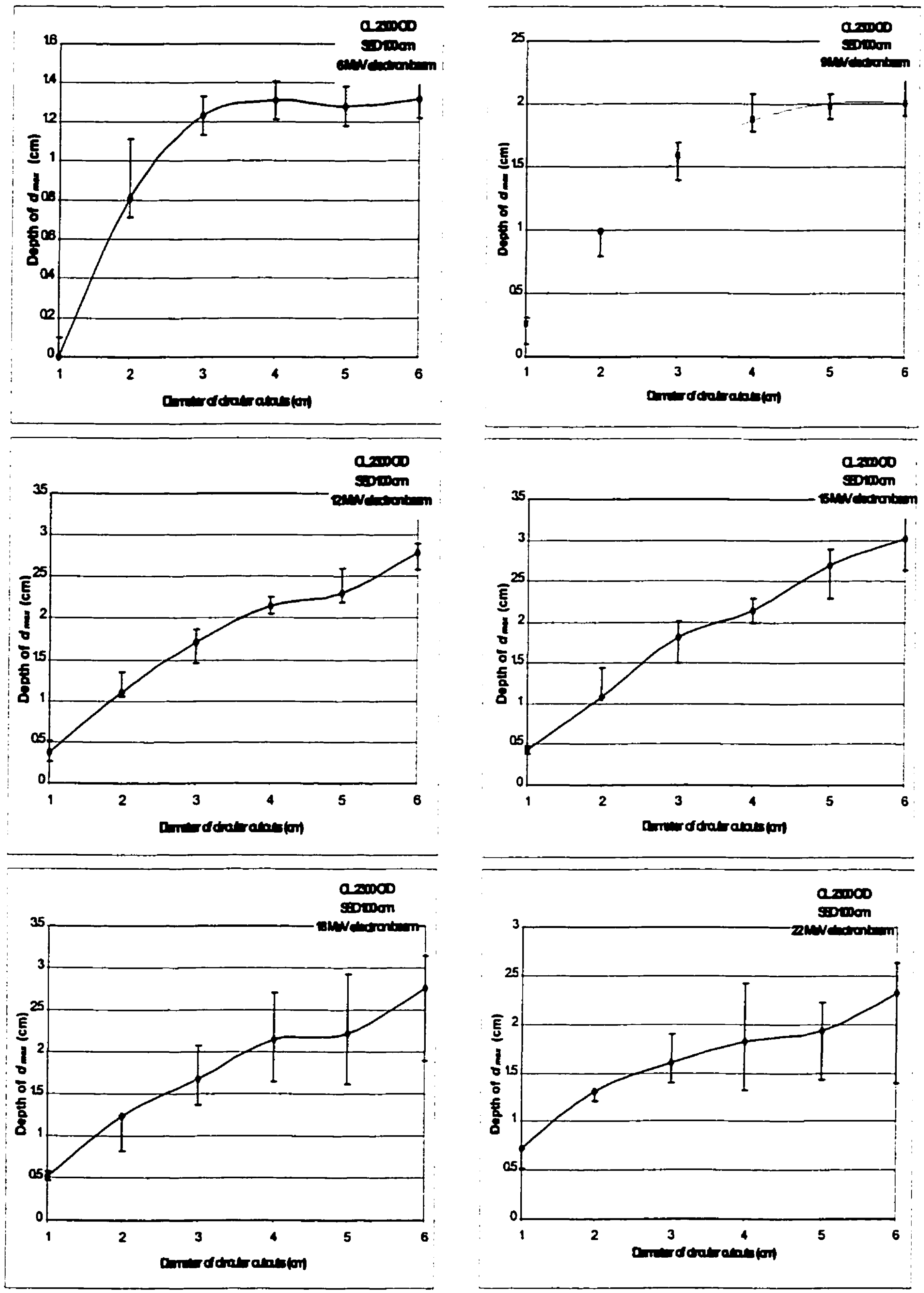

Figure 6.12: The relationship between d_{max} and field size for various electron beams on a CL 2300 C/D.

6.1.4 D_{80} dependence on field size

The depth of d_{80} is important in the choice of electron beam energy because it is often the treatment depth. This value can be approximated as one-third of the nominal energy of the beam. The correlation between d_{80} and field size, as shown in Fig. 6.11, is similar to that illustrated by d_{max}, as previously illustrated in Fig. 6.12. For small fields, d_{80} ranges from 1 to 2.3 cm, depending on the energy of the beam, and it increases to about 2 to 6.5 cm for larger fields. As was the case for d_{max}, d_{80} reaches a constant value above a certain field size for most energies, however, the side-scatter equilibrium value is achieved faster for low energy beams.

6.1.5 D_{50} dependence on field size

The correlation between d_{50} and field size of a CL 18 is shown in Fig. 6.13 and it is similar to that of d_{max} and d_{80}. The d_{50} value ranges from about 2 to 3 cm for small fields, depending on the energy of the beam, and increases to anywhere from 3.5 to 7 cm for larger fields. Again, as was the case for d_{max} and d_{80}, d_{50} achieves a state of equilibrium more rapidly for low energy beams, than for high energy beams.

6.2 Relative output factor

As discussed in section 5.5, the relative output factor is defined as the ratio of the dose at the central axis measured at d_{max} specific to the field size and energy to the dose obtained with the 10x10 cm^2 reference field size. Fig. 6.14 displays a set of relative output factors measured with rectangular cutouts on the CL 2300 C/D. The rectangular cutouts used were 10x1, 10x2, 10x3 and 10x4 cm^2. For all electron beam energies measured, the relative outputs increase as field size increases. For example, in the case of a 6 MeV beam, the relative output increases from about 0.52 to 1, whereas in the case of the 22 MeV beam, relative output increases from about 0.94 to 1. It is apparent that the increase is more severe for low energy beams, than for high energy beams. Similar results were obtained when circular cutouts (1 cm to 6 cm diameter in size) were used on the CL 2300 C/D, as shown in Fig. 6.15. For the 6 MeV beam, the relative output increases from about 0.43 to 1, whereas relative output increases from about 0.88 to 1 for the 22 MeV

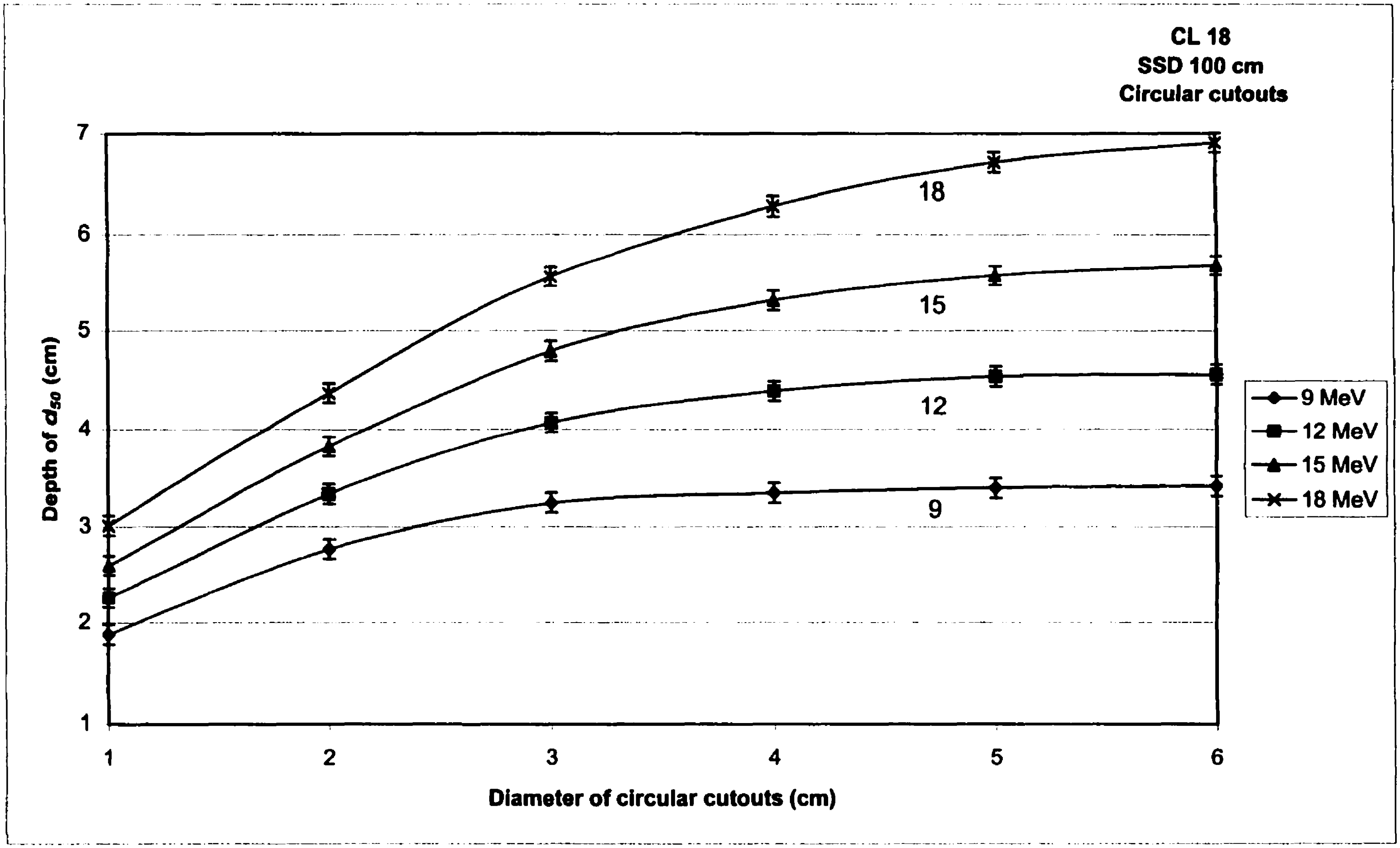

Figure 6.13: The relationship between d_{50} and field size for various electron energy beams on a CL 18.

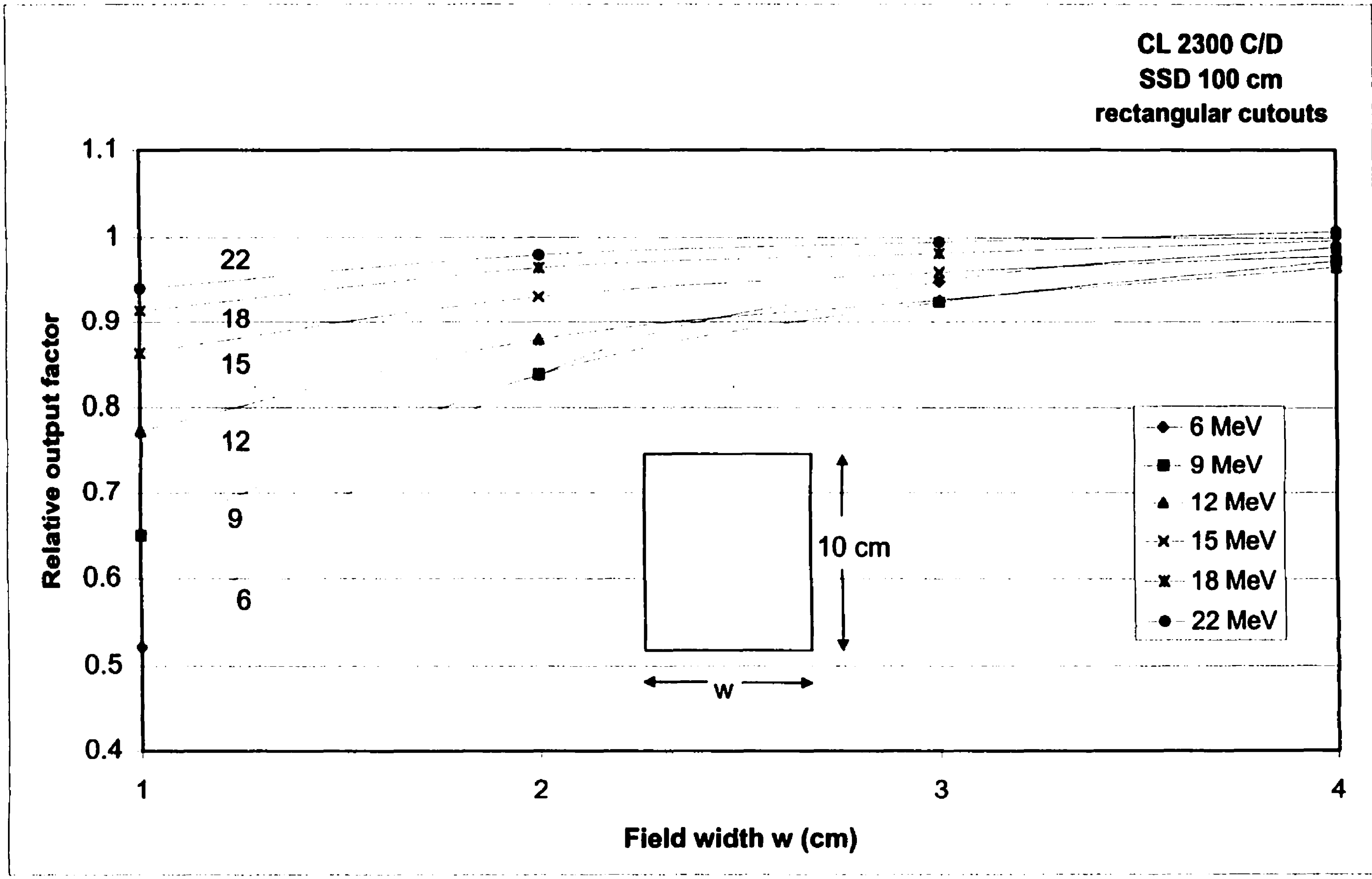

Figure 6.14: The relationship between the relative output factor and rectangular cutouts of different sizes on a CL 2300 C/D.

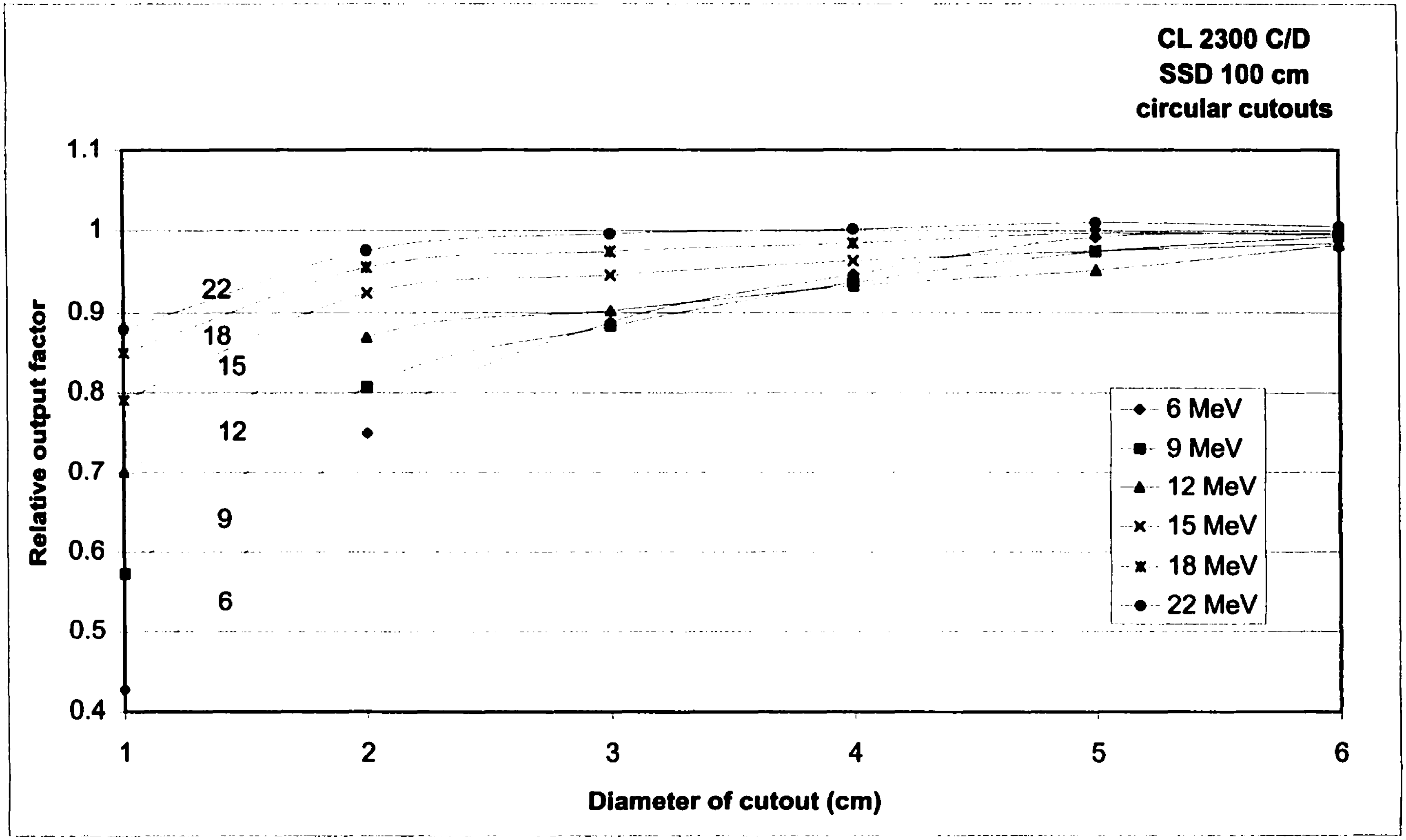

Figure 6.15: The relationship between the relative output factor and circular cutouts of different sizes on a CL 2300 C/D.

beam. Again, the increase is more severe for a low energy beam than for a high energy beam.

Fig. 6.16 illustrates the relative outputs measured with rectangular cutouts on a CL 18. Relative output increases with field size, for a 9 MeV electron beam, relative output increases from about 0.77 for a 10x1 cm^2 cutout to 0.97 for a 10x4 cm^2 cutout. Likewise, it increases from about 0.88 to 0.96 for the 18 MeV beam. Similar results were found with circular cutouts of various sizes, and they are shown graphically in Fig. 6.17. The relative output increases from 0.64 to 0.98 with cutout size for the 9 MeV beam, whereas it increases from 0.84 to 0.97 with cutout size for the 18 MeV beam. The relationship between the relative output factor and field size for the 15 and 18 MeV electron beams is illustrated more clearly by fitting the data to a best-fit curve (trendline). Finally, the relative output trends measured with both linacs agree, as shown in Fig. 6.14 to Fig. 6.17.

In conclusion, relative output increases as the size of the field increases. Also, the influence of field size on relative output is larger when lower energy beams are used. This relationship agrees with those found in literature. For example, Zhang et al.[10] measured relative output factors for square cutouts ranging from 2x2 to 9x9 cm^2 in size, whereby the relative output of a 6 MeV beam increased from 0.75 to 1 with cutout size, and the relative output increased from 0.85 to 1 for the 13 MeV beam. Moreover, Mills et al.[11] measured relative output factors with an ion chamber for 4x4, 5x5, and 6x6 cm^2 field sizes, and found that for the 6 MeV beam, the relative output increased from 0.76 to 0.89, whereas it increased from 0.96 to 0.98 for the 17 MeV beam. Other authors have observed similar trends[3,6,12-15]. In order to understand the dependence of relative outputs on field size, the concept of side scatter equilibrium is again applied using Fig. 6.18. For a reference geometry (when the collimator is at position A, indicated by the dotted lines), all the electrons are able to reach the point of d_{max}. However, when the collimator is sufficiently closed (position B, indicated by the solid lines), some of the electrons that could potentially have reached the point of d_{max} will strike the collimator instead. Therefore, side scatter equilibrium is not achieved, and a decrease in the output factor is observed with decreasing field size.

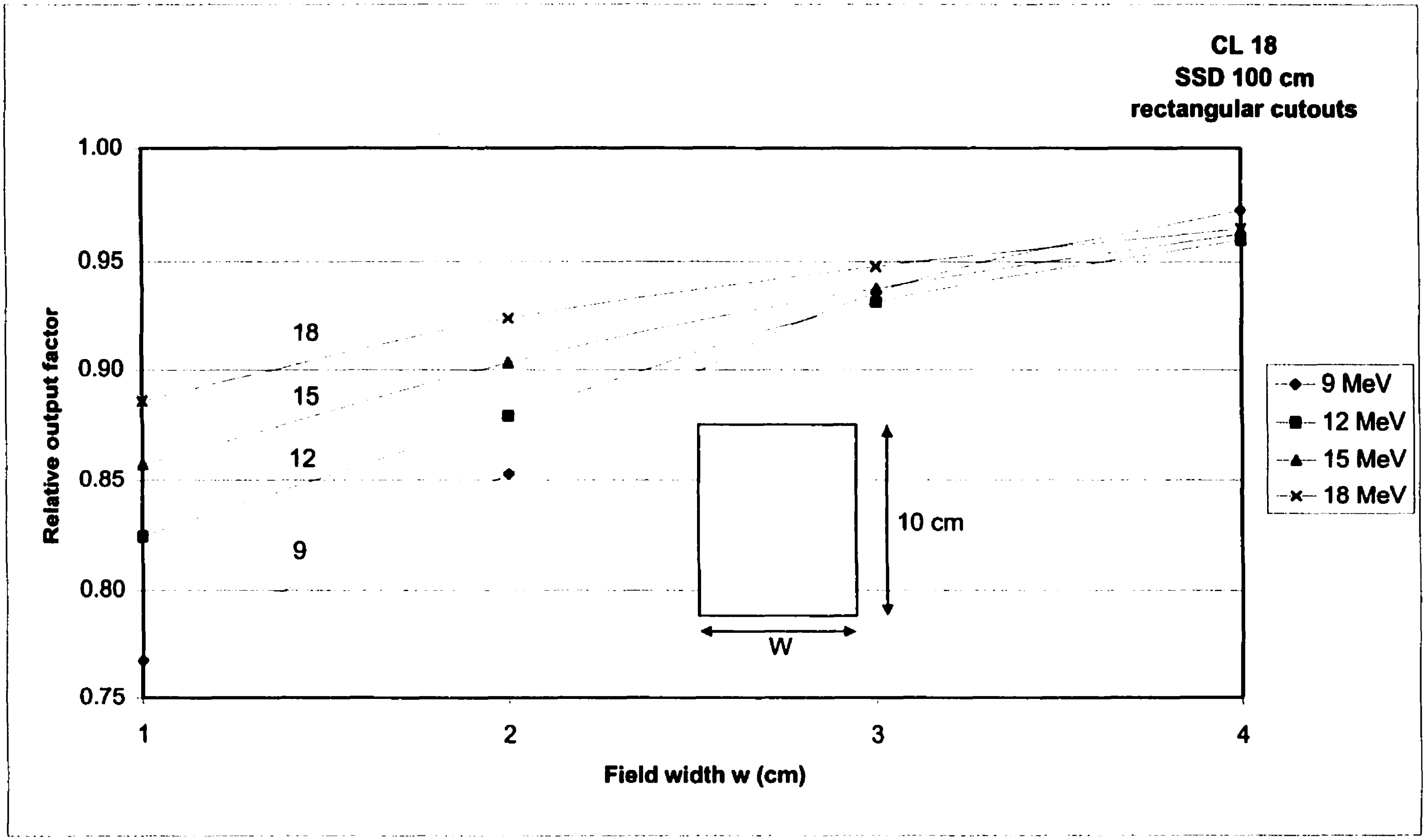

Figure 6.16: The relationship between the relative output factor and rectangular cutouts of different sizes on a CL 18.

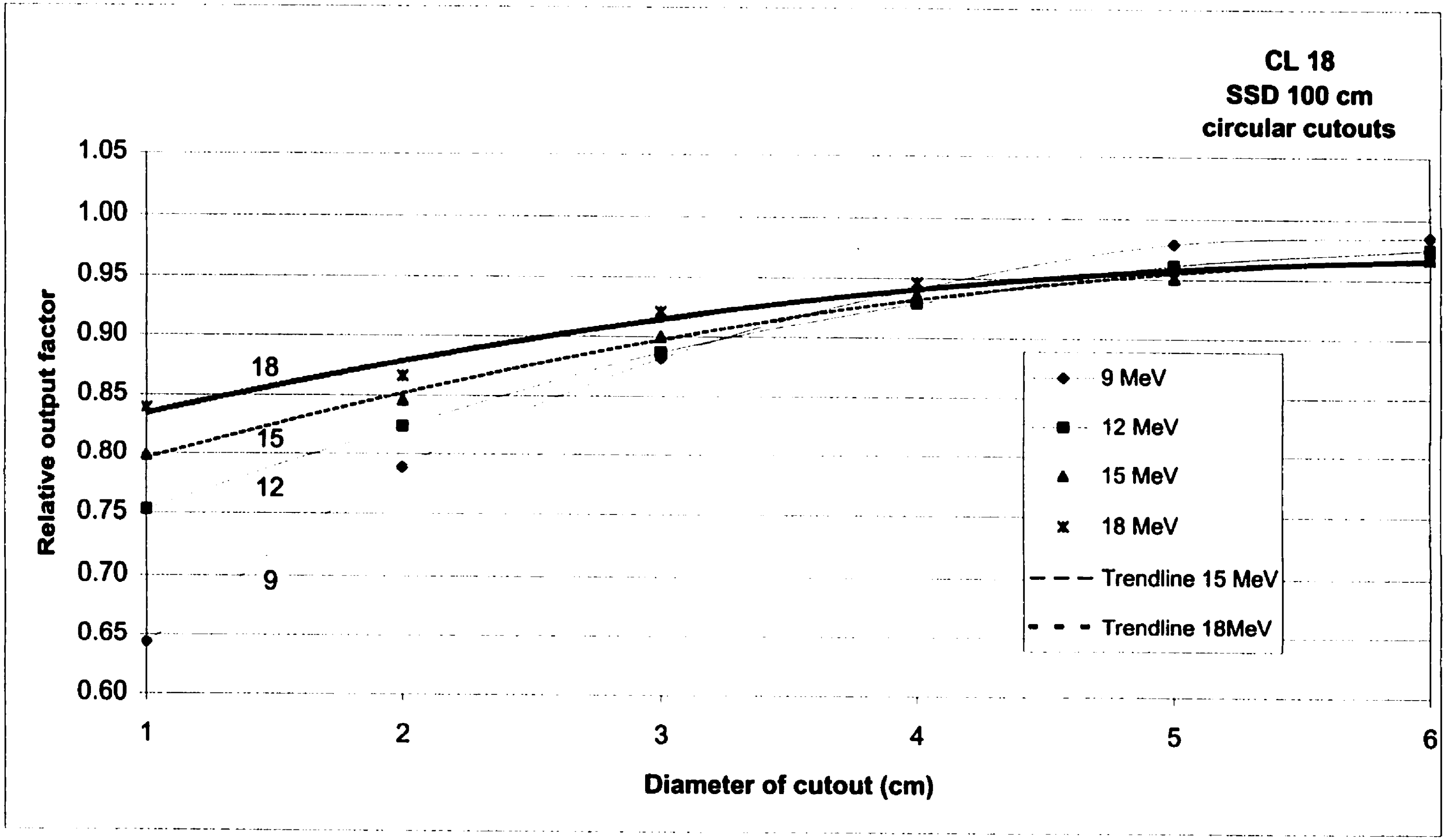

Figure 6.17: The relationship between the relative output factor and circular cutouts of different sizes on a CL 18.

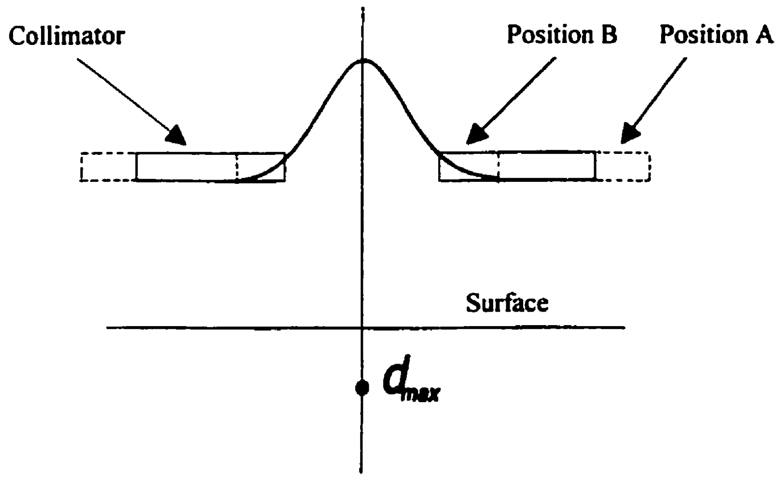

Figure 6.18: For a reference geometry (when the collimator is at position A), all the electrons are able to reach the point of d_{max}. However, when the collimator is sufficiently closed (position B), some of the electrons that could potentially have reached the point of d_{max} will strike the collimator instead.

6.3 Profiles

Profiles, or off-axis ratios, obtained using circular cutouts with diameters of 2, 3, 4, 5 and 6 cm for a 12 MeV beam in the in-plane direction with the CL 2300 C/D are shown in Fig. 6.19. Profiles for the 10x10 and 15x15 cm^2 cones are also displayed for comparison. These profiles were similar to the ones measured in the cross-plane direction, and they were all measured at their respective d_{max}. The profiles of large field sizes such as 10x10 cm^2 and 15x15 cm^2 are flat (1.8% and 2.3% respectively), as defined by AAPM[1] in chapter 3 of this thesis. However, they experience a more severe fall-off at the beam edge and subsequently become less flat when the field sizes become smaller, indicating potential lateral underdosage. With decreasing field size, the profiles become rounder in shape, and they approach a Gaussian distribution for very small cutouts, as shown for the 1 or 2 cm diameter cutout (Fig. 6.20). These trends are in agreement with Niroomand-Rad et al.[3], who reported a reduction of beam flatness for fields ranging from 1x1 to 5x5 cm^2 and an energy span of 5 to 18 MeV, measured with a diode. Kapur et al.[12] reported similar results with fields ranging from 1x1 to 4x4 cm^2, measured with both film and diode.

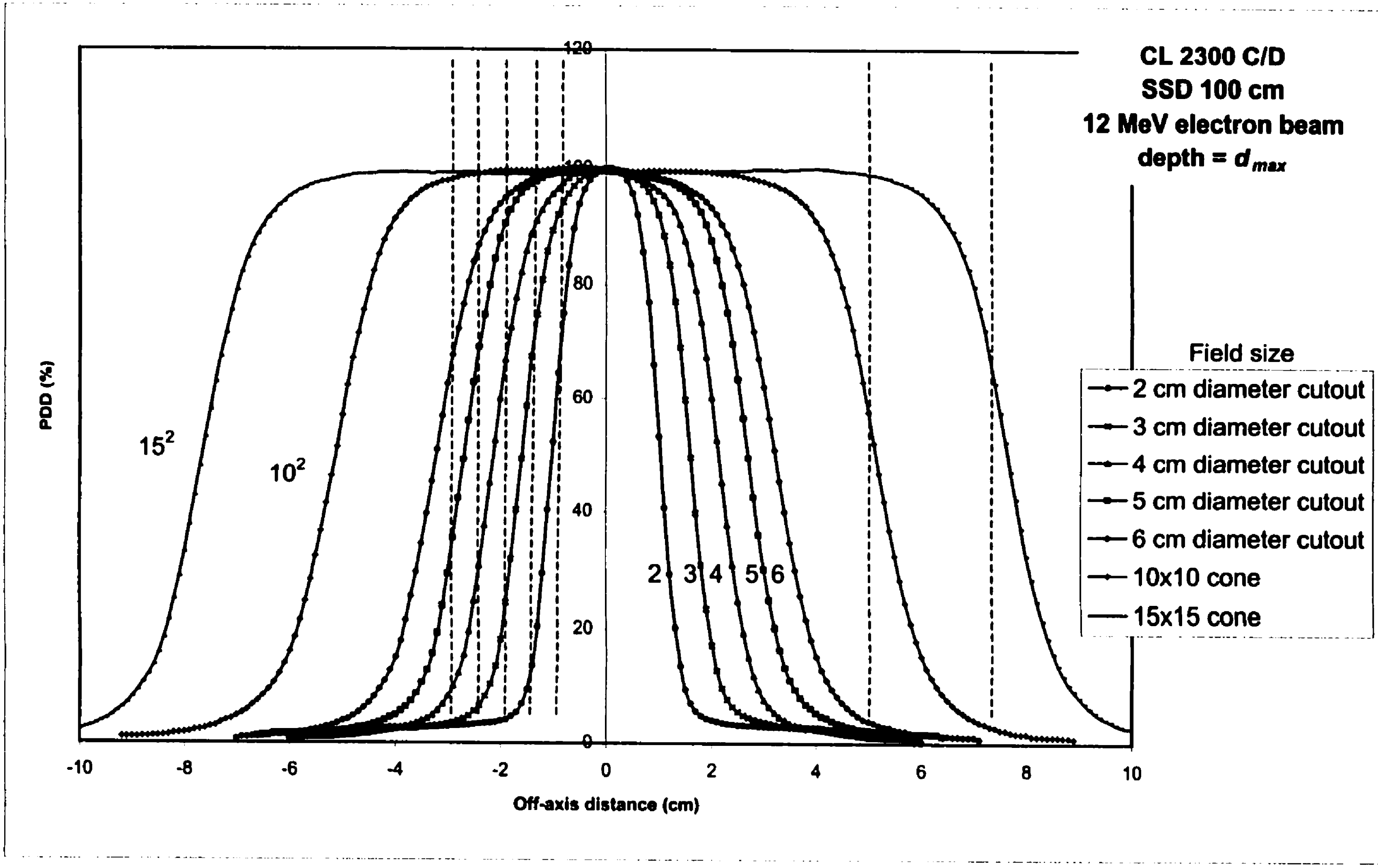

Figure 6.19: Profiles measured with circular cutouts and regular cones of various sizes for a 12 MeV electron beam on a CL 2300 C/D.

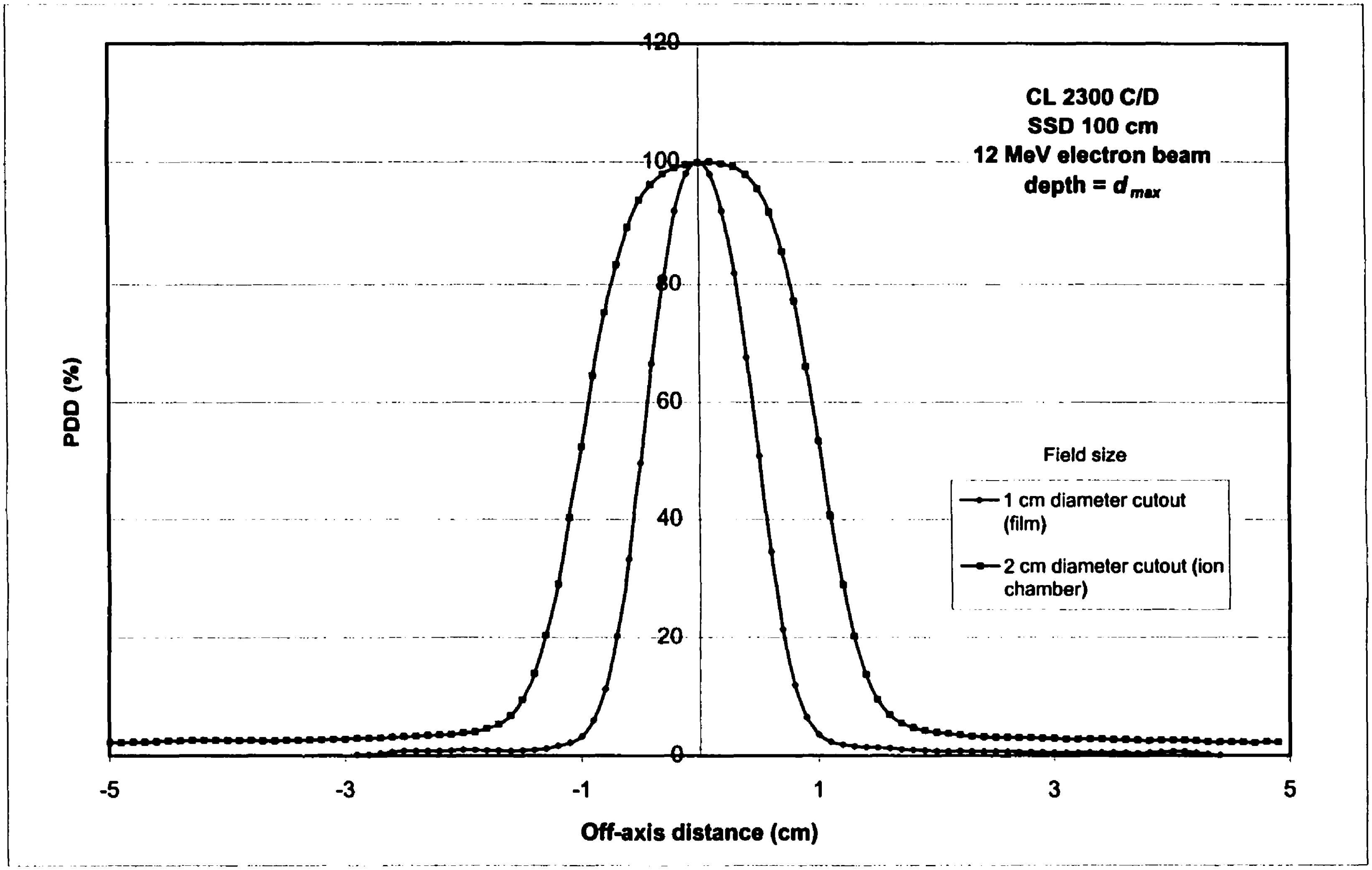

Figure 6.20: Profiles measured with 1 and 2 cm diameter circular cutouts, using film and ion chamber respectively.

The Gaussian-shaped profile of a very small cutout raises some concerns in treatment planning. In order to address this problem, special attention must be given to field placement, as a slight displacement of the beam may result in a large dose reduction. A possible solution to this problem is to place the collimation on the skin of the patient[3]. If the collimation is placed away from the patient, the electron beam would be less uniform, particularly at low energies where the beam edge is less defined. Alternately, one can also increase the field size, so that the 80% or 90% isodose line still covers the tumor.

Profiles for very small fields cannot be measured accurately with an ion chamber due to the size of the chamber relative to the cutouts. Measured profiles of beams 1 and 2 cm in diameter using an ion chamber are shown in Fig. 6.21. The percent dose transmitted through the cerrobend should be constant (about 2 to 3%), regardless of the field size. However, the transmission dose is higher for a 1 cm diameter cutout, and this discrepancy is explained as follows. For a cutout of 2 cm or larger in diameter, the entire ion chamber is in the radiation field, and the maximum dose at the central axis is measured to be 100%. However, for cutouts with diameters less than 2 cm, only a portion of the ion chamber is in the electron beam. Therefore, the maximum dose at the central axis is reduced, resulting in a seemingly larger transmission dose. Therefore, the data for 1 cm beam taken with the ion chamber is not valid.

Film has been proven to be useful in measuring profiles of small fields[16], since the only limitation is the diameter of the detector's light aperture, which is typically about 0.8 mm (p.39). Fig. 6.21 displays the profile of a 2 cm diameter field using an ion chamber and the profile of a 1 cm diameter field measured with film, since the field is too small for ion chamber measurements (Fig. 6.20 and Fig. 6.21). Therefore, all profiles obtained with a 1 cm diameter cutout were measured with film.

6.4 Calculating electron beam parameters

It is both tedious and time consuming to measure beam parameters for every cutout, therefore, it is often more desirable to calculate depth dose and relative output using either published formulas or more complicated computer algorithms. The relative output

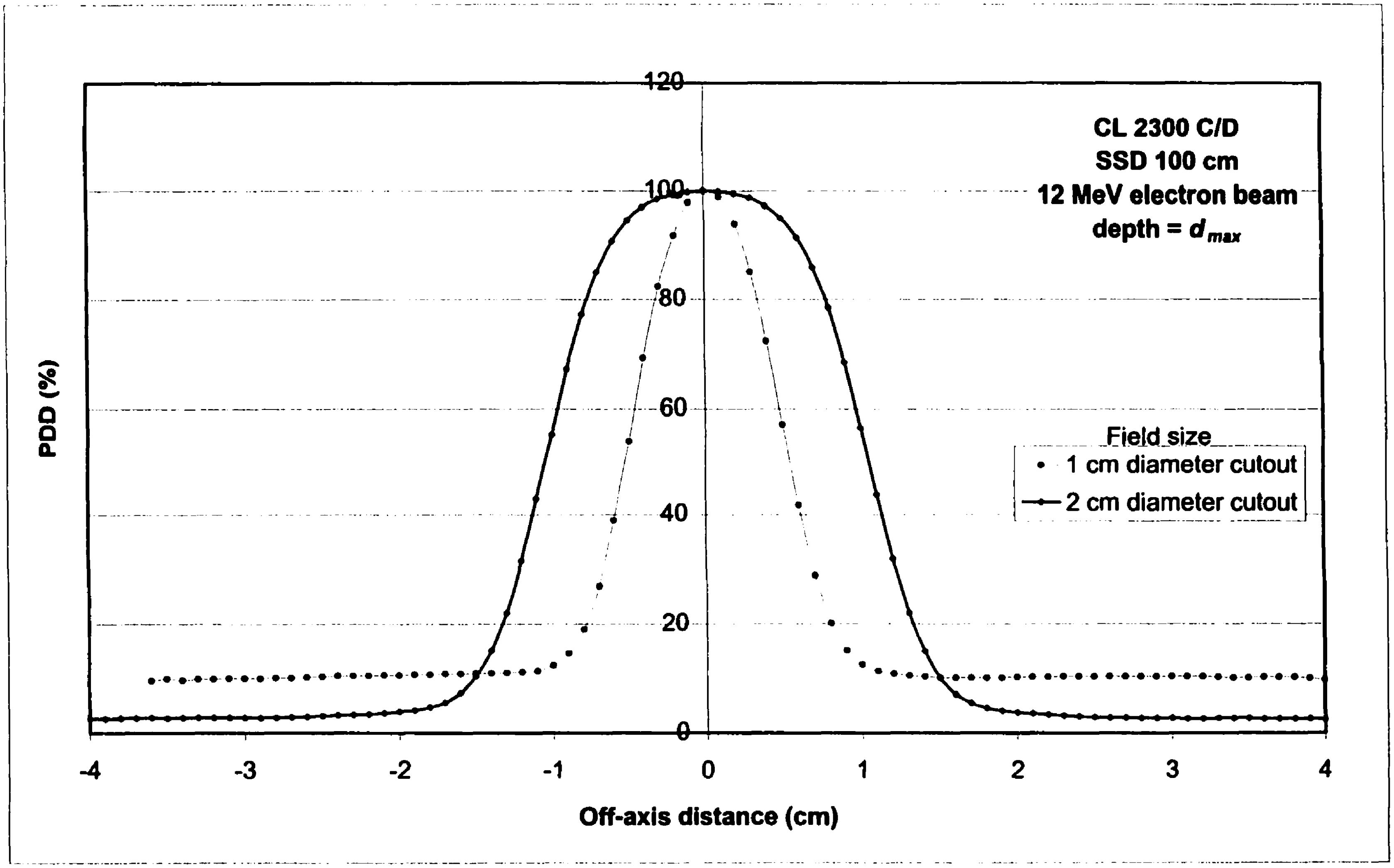

Figure 6.21: Profiles measured with 1 and 2 cm diameter circular cutouts using an ion chamber.

of an arbitrary square or rectangular field can be calculated using either the square root method[17] or the 1 dimensional (1 D) method[14].

The square root method, developed by Hogstrom et al.[17], predicts the relative output factor of a rectangular field from the relative output factors of square fields. It is given by

$$OF(X,Y) = [OF(X,X) \times OF(Y,Y)]^{1/2}, \tag{6.1}$$

where *OF* is the output factor and *X*, *Y* are the dimensions of the relevant field. This method has an error of 1% for most fields and energies between 6-20 MeV, but it increases to 3% for large fields with large aspect ratios (such as 30x10 cm^2), where the aspect ratio is defined as the length of the long side to the short side of a rectangular field.

The validity of this method can be tested by comparing the calculated results with the experimental results of this work. Using Eq. 6.1, the relative output factor for a 10x4 cm^2 field can be calculated from the output data of a 10x10 and a 4x4 cm^2 field (CL 2300 C/D, 12 MeV electron beam). For example,

$$\begin{aligned} OF(10,4) &= [OF(10,10) \times OF(4,4)]^{1/2} \\ &= [1 \times 0.944]^{1/2} \\ &= 0.972 \end{aligned}$$

The actual relative output factor measured using a 10x4 cm^2 cutout was 0.966, therefore, the percentage difference between the calculated and measured values is less than 1%.

Alternately, square field data can be estimated from measurements obtained with circular fields using Eq. 6.2[18]. In this method,

$$S = 1.792\,R, \tag{6.2}$$

where *S* represents the length of a square cutout and *R* represents the radius of a circular cutout. Therefore, the output factor of a 1x1 cm^2 square cutout is equal to the one measured using a circular cutout of 0.558 cm in radius, or 1.12 cm in diameter. The diameter equivalences for square fields 2x2 cm^2 and 3x3 cm^2 are calculated in a similar fashion and the relative output factor values are interpolated from the data in Fig. 6.16

(CL 2300 C/D, 12 MeV electron beam). Measured values compared with values predicted by the square root method are presented in Table 6.1.

Cutout Size (cm^2)	Measured relative output factor	Relative output factor calculated using the square root method	Percent difference (%)
10 x 1	0.77	0.85	10.4
10 x 2	0.88	0.94	6.8
10 x 3	0.93	0.96	3.2
10 x 4	0.97	0.97	0

Table 6.1: A comparison between relative output factors obtained from measurements and calculations using the square root method of various cutout sizes for a 12 MeV electron beam on a CL 2300 C/D.

Although the relative output factors obtained from measurements and calculations correlate highly for a 10x4 cm^2 cutout, the level of correlation decreases with increasing aspect ratio. The square root method cannot accurately calculate the output factors of these fields, and therefore alternate methods must be used.

The 1 D method calculates the relative output of a rectangular field (X, Y), and is found using the following formula:

$$OF(X,Y) = OF(X,10) \times OF(10,Y) + CF(X,Y), \tag{6.3}$$

where 10x10 cm^2 is the square reference field. For example, the relative output factor of a cutout field of 5x2 cm^2 is given by the sum of the correction factor (*CF*) and the product of the relative output factors of the 5x10 cm^2 field and the 10x2 cm^2 field. *CF* accounts for differences primarily due to the scatter off the x-ray jaws, and it is calculated using:

$$CF\,(\mathrm{X,Y}) = 0,\ \Delta \le 0, \text{ or}$$

$$CF\,(\mathrm{X,Y}) = \mathrm{C},\ \Delta > 0, \tag{6.4}$$

where C is a constant of proportionality, and Δ is defined as

$$\Delta = \frac{(X-10)(Y-10)}{[(X-10)(Y-10)]^{1/2}}. \tag{6.5}$$

According to Mills[14], this method agrees with measured data to within 1.5% for all energies and field sizes ranging from 4x4 to 30x30 cm^2.

Again, the accuracy of this method can be investigated by comparing the calculated results with the experimental results of this work. Using Eq. 6.3 to Eq. 6.5, the relative output factor for a 4x4 cm^2 field can be calculated from the output data of a 10x4 and a 4x10 cm^2 field (CL 2300 C/D, 12 MeV electron beam). For example,

$$OF\,(4\text{x}4) = OF\,(4\text{x}10) \text{ x } OF\,(10\text{x}4) + CF\,(4\text{x}4).$$

Since $\Delta = 6$, then $CF\,(4\text{x}4) = \text{C}$, where $\text{C} \cong 0.0008$ for a 12 MeV electron beam[14].

Therefore,

$$OF(4x4) = 0.97x0.97 + 0.0008$$

$$= 0.942$$

Measured data for the 4x10 cm^2 field is not available, and it is assumed that it is equal to the data obtained with the 10x4 cm^2 cutout for this comparison. The actual relative output factor measured with a 4x4 cm^2 cutout was 0.944, therefore, the percentage difference between the calculated and measured values is 0.2%. Measured values compared with values predicted by the 1D method are presented in Table 6.2.

Cutout Size (cm^2)	Measured relative output factor	Relative output factor calculated using the 1D method	Percent difference (%)
1 x 1	0.72	0.59	18.1
2 x 2	0.89	0.78	12.4
3 x 3	0.92	0.87	5.4
4 x 4	0.94	0.94	0

Table 6.2: A comparison between relative output factors obtained from measurements and calculations using the 1D method of various cutout sizes for a 12 MeV electron beam on a CL 2300 C/D.

The above results seem to suggest that the 1D method can predict the relative output factors of larger cutouts, such as the 4x4 cm^2, rather than the smaller cutouts, such as the 1x1 cm^2. It is also important to note that X and Y collimators do not affect the output equally[14]. For example, a 10x20 cm^2 field does not have the same output as a 20x10 cm^2

field, hence contributing to the error in the above relative output calculation. Since only the 1D method accounts for the difference in scatter geometry between the X and Y collimators, it is expected, and has been shown by Mills *et al.* that the 1D method correlates with measured data better than the square root method[14].

Alternately, a clinic may choose to use "BEAM", a Monte-Carlo code developed by Rogers et al.[19], which is able to simulate clinical electron beams and calculate central-axis depth dose, transverse dose profiles, and output factors for a range of square and rectangular cutouts to within 2% accuracy with measured data[12]. This study involves the acquisition of clinical dosimetric parameters and the investigation of the correlation between these properties and cutout size. However, it would be beneficial to compare these measured data with "BEAM" calculated results in the future.

A problem with these calculational methods is that since tumors are often irregularly shaped, custom cutouts must be used in order to conform the radiation field to the tumor, while sparing as much healthy tissue as possible. These irregularly shaped fields are sometimes calculated with other methods such as the Clarkson scatter integration method[20] and pencil-beam algorithm[21], although these newer techniques have not yet received extensive investigation.

6.5 Summary

This chapter discusses the correlation between *PDD*, relative outputs, and profiles with cutouts of different sizes and shapes. It has been confirmed that the effect of field size on PDD is significant for small fields, specifically when the field dimension or diameter is less than R_p. With decreasing field size, the surface dose of a *PDD* increases, while d_{max}, d_{80}, and d_{50} decrease. The bremsstrahlung dose is independent of field size, and it is a function of only the energy of the electron beam for a given linac, increasing from about 1% for low energy beams to 5% for high energy beams. The relative output was observed to increase with increasing field size, and the effect of field size on relative output is more severe for lower energy beams. Finally, it has been shown that the field profiles become less flat for small fields, and ultimately a Gaussian distribution is obtained for very small fields. It has been suggested that calculation and computational methods such as the 1 D method, the square root method, and the BEAM algorithms may serve as good alternatives to individual measurements for obtaining beam parameters.

6.6 References

1. Khan et al.,"Clinical electron beam dosimetry: Report of AAPM Radiation Therapy Committee Task Group No. 25," Med. Phys. 18, 73-109 (1991).
2. P. McGhee, T. Chu, P. Dunscombe, "The characterization of clinical electron beams of arbitrary shape in water," Proceedings of the Canadian Organization of Medical Physicists 42nd Annual Meeting, 107-110 (1996).
3. A. Niroomand-Rad, M.T. Gillin, R.W. Kline, D.F. Grimm, "Film dosimetry of small electron beams for routine radiotherapy planning," Med. Phys. 13, 416-421 (1986).
4. J. Cygler, X.A. Li, G.X. Ding, E. Lawrence, "Practical approach to electron beam dosimetry at extended SSD," Phys. Med. Biol. 42, 1505-1514 (1997).
5. J.A. Meyer, J.R. Palta, K.R. Hogstrom, "Demonstration of relatively new electron dosimetry measurement techniques on the Mevatron 80," Med. Phys. 11, 670-677 (1984).
6. S.C. Sharma, D. L. Wilson, B. Jose, "Dosimetry of small fields for Therac 20 electron beams," Med. Phys. 11, 697-702 (1984).
7. G.G. Zhang, D.W.O. Rogers, J.E. Cygler, T.R. Mackie, "Effects of changes in stopping-power ratios with field size on electron beam relative output factors," Med. Phys. 25, 1711-1716 (1998).
8. K.R. Hogstrom, "Clinical electron beam dosimetry: basic dosimetric data," in Advances in Radiation Oncology Physics, Dosimetry, Treatment Planning, and Brachytherapy, AAPM Monograph No. 19, ed. J.A. Purdy (American Institute of Physics, New York, 1992), 390-429.
9. International Commission on Radiation Units and Measurements (ICRU), Radiation Dosimetry: Electrons with Initial Energies Between 1 and 50 MeV, ICRU Report 21, Bethesda, Maryland (1972).
10 G.G. Zhang, D.W.O. Rogers, J.E. Cygler, T.R. Mackie, "Monte Carlo investigation of electron beam output factors versus size of square cutout," Med. Phys. 26, 743-750 (1999).

11. M.D. Mills, K.R. Hogstrom, P.R. Almond, "Prediction of electron beam output factors," Med. Phys. 9, 60-68 (1982).

12. A. Kapur, C-M. Ma, E.C. Mok, D.O. Findley & A.L. Boyer, "Monte Carlo calculations of electron beam output factors for a medical linear accelerator," Phys. Med. Biol. 43, 3479-3494 (1998).

13. P.J. Biggs, A.L. Boyer & K.P. Doppke, "Electron dosimetry of irregular fields on the Clinac 18," Int. J. Radiation Oncology, Biol. Phys. 5, 433-440 (1978).

14. M.D. Mills, K.R. Hogstrom & R.S. Fields, "Determination of electron beam output factors for a 20-MeV linear accelerator," Med. Phys. 12, 473-476 (1985).

15. B.J. McParland, "A method of calculating the output factors of arbitrarily shaped electron fields," Med. Phys. 16, 88-93 (1989).

16. A.S. Shiu, V.A. Otte & K.R. Hogstrom, "Measurement of dose distribution using film in therapeutic electron beams," Med. Phys. 16, 911-925 (1989).

17. K.R. Hogstrom, M.D. Mills & P.R. Almond, "Electron beam dose calculations," Phys. Med. Biol. 26, 445-459 (1981).

18. S.C. Klevenhagen, Physics and Dosimetry of Therapy Electron Beams, Medical Physics Publishing, Madison, Wisconsin, U.S.A. (1993).

19. D.W.O. Rogers, B.A. Faddegon, G.X. Ding, C-M. Ma, J. We & T.R. Mackie, "BEAM: a Monte Carlo code to simulate radiotherapy treatment units," Med. Phys. 22, 503-524 (1995).

20. A. Dutreix & E. Briot, "The development of a pencil-beam algorithm for clinical use at the Institut Gustave Roussy," in The computation of dose distributions in electron beam radiotherapy, ed. A.E. Nahum (Sweden: Umea University Press, 1985), 242-270.

21. I.A.D. Bruinvis, A. van Amstel, A.J. Elevelt & R. van der Laarse, "Calculation of electron beam dose distributions for arbitrarily shaped fields," Physics in Medicine and Biology 28, 667-683 (1983).

CHAPTER 7: CONCLUSIONS

7.1 Summary

Electron beam cutouts are used in the clinic to shape the beam used to treat small superficial lesions by conforming the shape of the radiation field to the tumor, while sparing dose to surrounding tissues and organs at risk. In this thesis, PDD, profiles and output factors have been measured for regular electron cones and small, clinically relevant cutouts of various shapes and sizes. The diameters of the circular cutouts are 1 cm, 2 cm, 3 cm, 4 cm, 5 cm, and 6 cm. The rectangular cutouts measure 10x1, 10x2, 10x3, and 10x4 cm^2, and a square cutout of 4x4 cm^2 was also used. All measurements were performed on a CL 2300 C/D and a CL 18, with energies ranging from 6 to 22 MeV and 9 to 18 MeV respectively. It has been confirmed that the effect of field size on depth dose is significant when the field dimension is less than R_p, due to the lack of side-scatter equilibrium, thus, PDD should be measured for small cutouts having a minimum field width smaller than R_p. In addition to providing a comprehensive set of electron beam data obtained with cutouts of different sizes, this thesis has also investigated the correlation of PDD, profiles and output factors with field size. It was shown that as field size decreases, a "compression" of the PDD curve is observed, whereby the surface dose increases, while the d_{max}, d_{80} and d_{50} decrease. It has been shown that the profiles for very small fields, such as the 1 cm diameter cutout, cannot be reliably measured with an ion chamber of size 0.03 cm^3, and the corresponding profiles were found to be erroneous. This is attributed to the dimensions of the ion chamber, as a portion of the chamber is not in the radiation field. The results show that the profiles lose their flatness as the field size becomes smaller, and that very small fields may be inappropriate for treatment because of underdosage to lateral tissues. This also raises some concerns in treatment planning and delivery, because a slight offset of the field will result in a large dose displacement with respect to the intended target. Finally, the relative output factor is observed to increase with cutout size, with the effect more severe for low energy beams than high energy beams. These trends agree well with published data, and they have been explained using the concept of side-scatter equilibrium.

7.2 Future Work

It has been shown that individual beam measurements are recommended for small electron beam fields. An alternative method to custom measurement would be to implement either the 1 D method, the square root method, or one of the computer algorithms to calculate depth dose and output factors for small electron beam fields, resulting in significant savings in time and labor.

It has been established that individual depth dose measurements are necessary when the field dimension is less than R_p. However, this guideline is not applicable to cutouts that are very irregular in shape, which constitute a significant fraction of clinically relevant fields in radiotherapy. A new guideline regarding highly irregular fields is needed, and warrants further study.

Most of the data collected in this study were taken with an ion chamber, but due to its large size relative to a very small cutout, it has been shown that film or diode may be a better alternative under these certain circumstances. Measurement technique improvements may be possible with an electronic portal imaging device (EPID) or radio-chromic film such as the GafChromic film (GAF Chemicals Corporation, Wayne, N.J.). Although it is more expensive compared to the radiographic films used in this thesis, GafChromic film requires no developing, as it turns blue in color after irradiation, resulting in significant time savings.

The nature of certain cancer sites such as head, neck, peritoneum and breast requires special treatment planning and setup. This is necessary due to the limitation of the electron cone as body anatomy may obstruct the positioning of the applicator. Options to overcome this problem include the use of off-centered cutouts and extended SSDs (110 to 130 cm). Since all the cutouts used in this thesis were centered on the central axis of the electron applicator, it would be necessary to establish the differences in beam parameters using off-centered cutouts and extended SSD treatments. Other cancer sites may involve oblique and irregular surfaces and tissue heterogeneities including bone, lung, and air cavities. Both of these clinical situations require further investigation. Finally, it may be worthwhile to implement the electron dosimetric data measured with cutouts into the treatment planning system, and future work could involve the development and testing of these algorithms.

Appendix

A.1 Description of content

The appendix consists of 2 main sections: PDDs measured with rectangular cutouts and profiles measured with circular and rectangular cutouts. The PDDs measured with rectangular cutouts of sizes 10x1, 10x2, 10x3, and 10x4 cm^2 are shown in Fig. A.1 – Fig. A.6 for energies ranging from 6 to 22 MeV on the CL 2300 C/D. Due to the large number of profiles measured for this thesis, only a representative set of profiles is displayed. Specifically, only profiles measured with the 6, 12, and 22 MeV electron beams on the CL 2300 C/D are illustrated. Moreover, a complete set of data is shown for extreme cutout sizes, such as the 1 and 6 cm diameter circular cutouts, or the 10x1 and 10x4 cm^2 rectangular cutouts. For these cases, profiles measured and normalized at the surface, d_{max}, d_{90}, d_{80}, d_{50}, and d_{20} are displayed. As mentioned in chapter 6, the profiles for the 1 cm circular cutout were measured with film and solid water, rather than with an ion chamber. The surface dose was measured at a depth of 0.2 cm, instead of 0.05 cm, because the minimum thickness of the solid water sheets is 0.2 cm. For the remaining cutouts, only profiles measured at d_{max} and d_{80} are shown. Lastly, the similarity between the profiles obtained with the 12 MeV electron beams on a CL 18 and a CL 2300 C/D linac is investigated by comparing the profiles measured with the 4 cm diameter circular cutout (Fig. A.25) and the 10x3 cm^2 rectangular cutout (Fig. A.50 – Fig. A.51) on both machine. Although profiles were measured in the in-plane and cross-plane directions, only in-plane profiles are illustrated for circular cutouts.

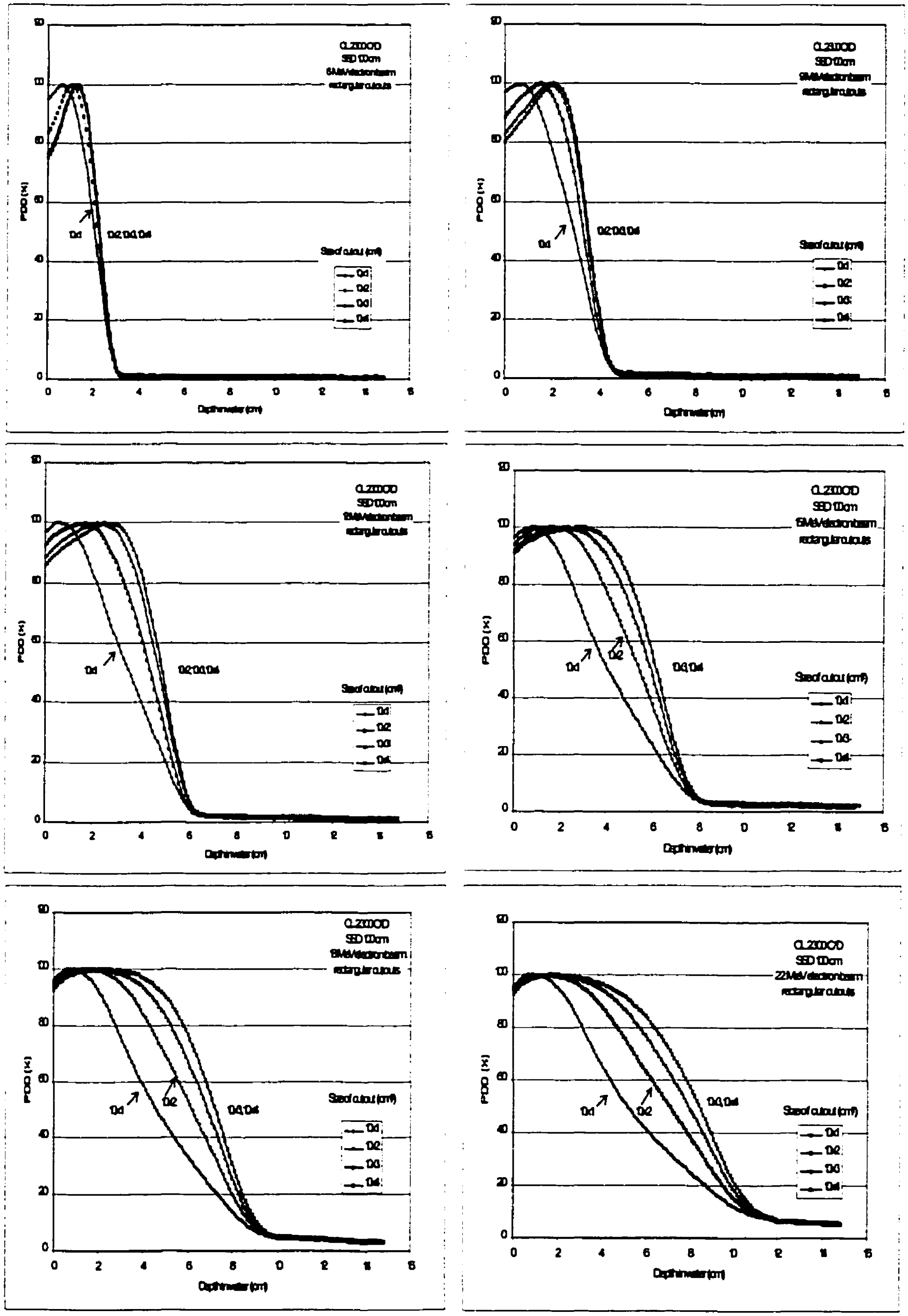

Figure A.1-6: PDDs measured with rectangular cutouts for various electron energy beams on a CL 2300 C/D.

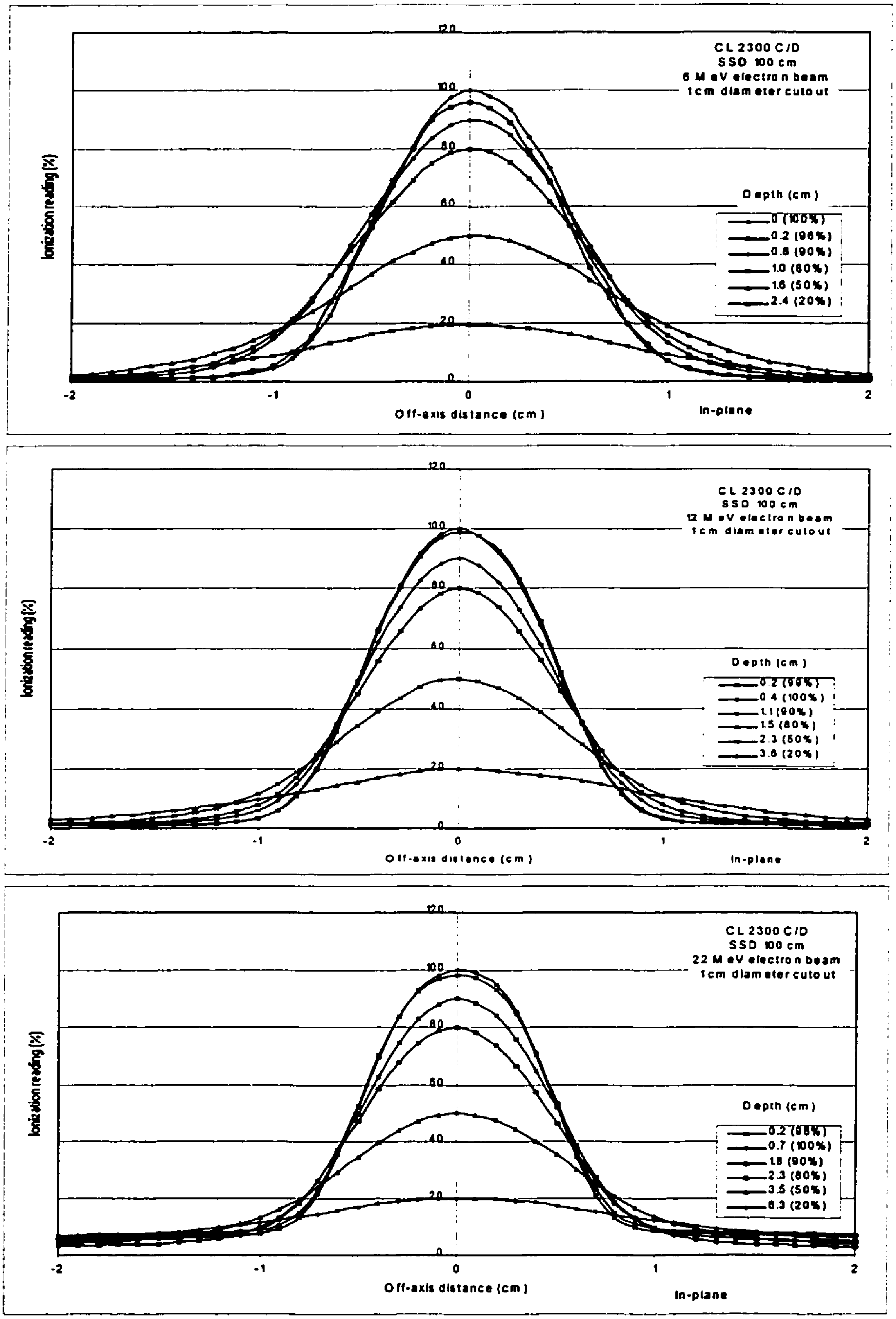

Figures A.7-9: Profiles measured with a 1 cm diameter cutout for various electron energy beams on a CL 2300 C/D.

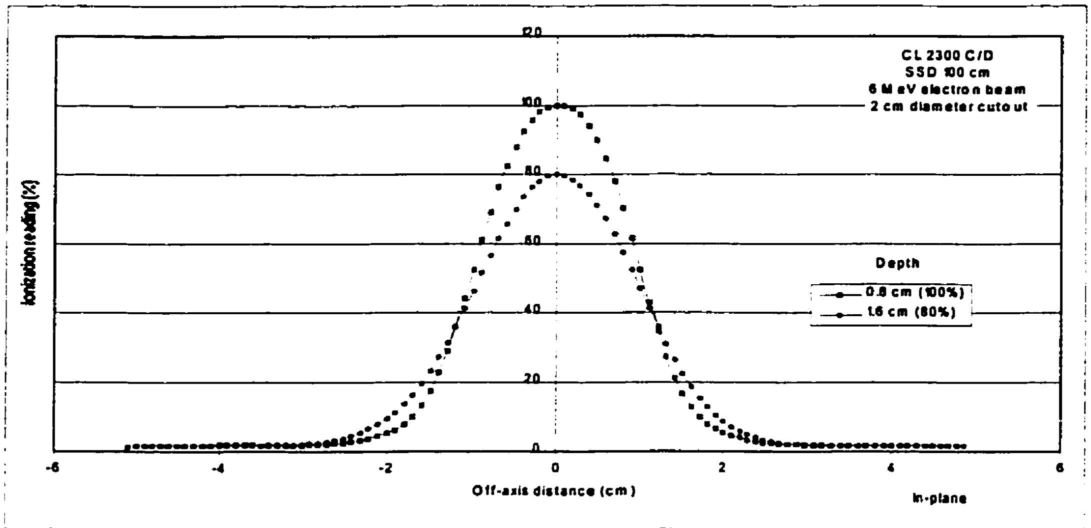

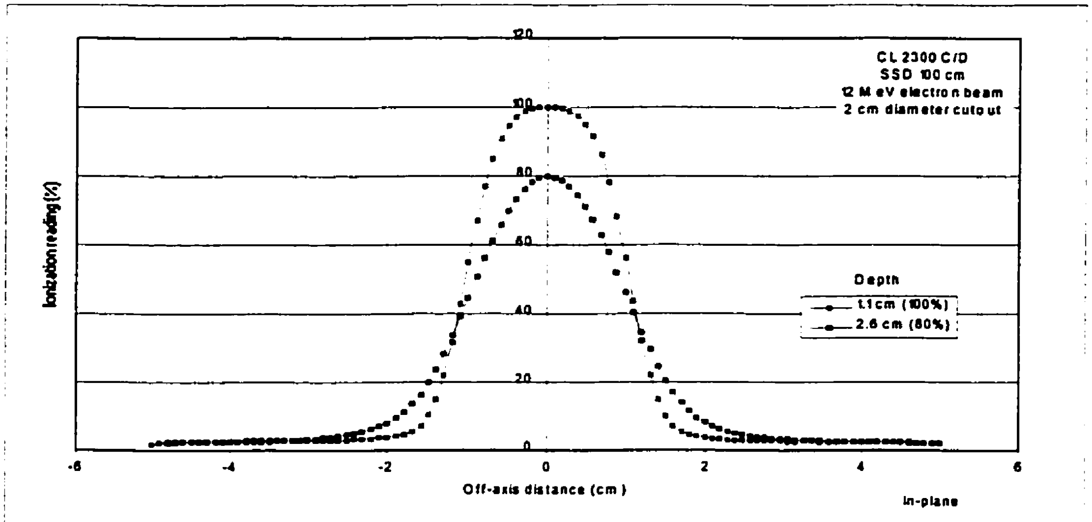

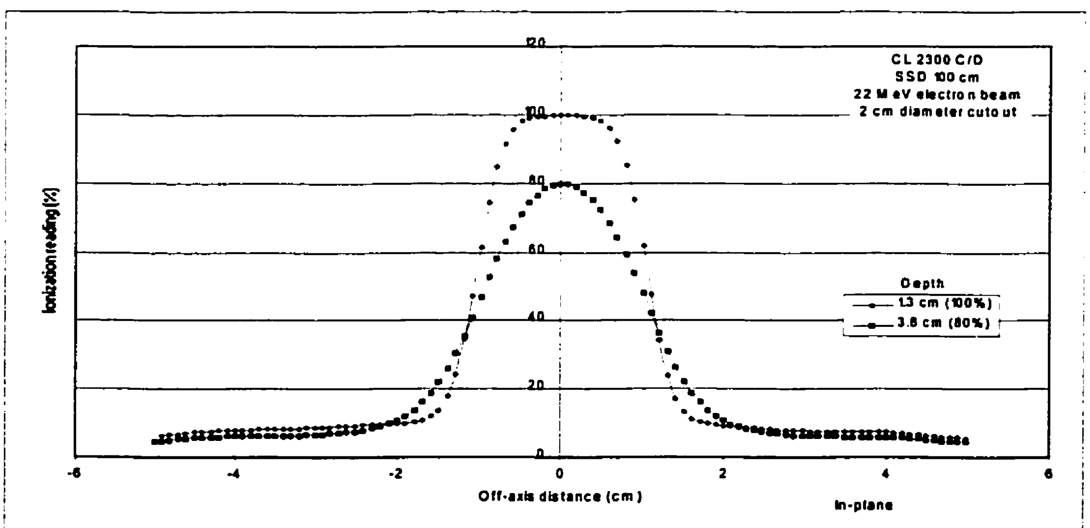

Figures A.10-12: Profiles measured with a 2 cm diameter cutout for various electron energy beams on a CL 2300 C/D.

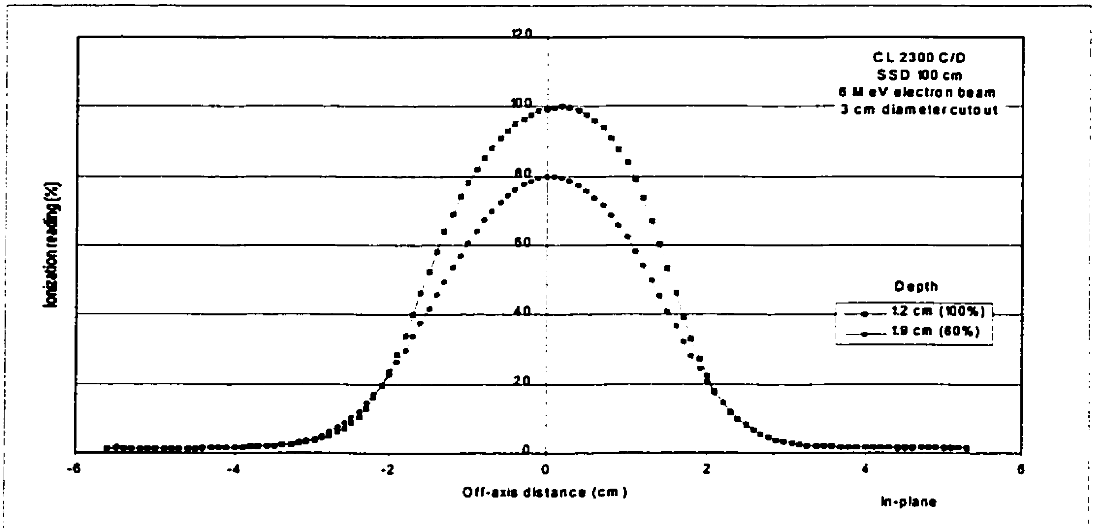

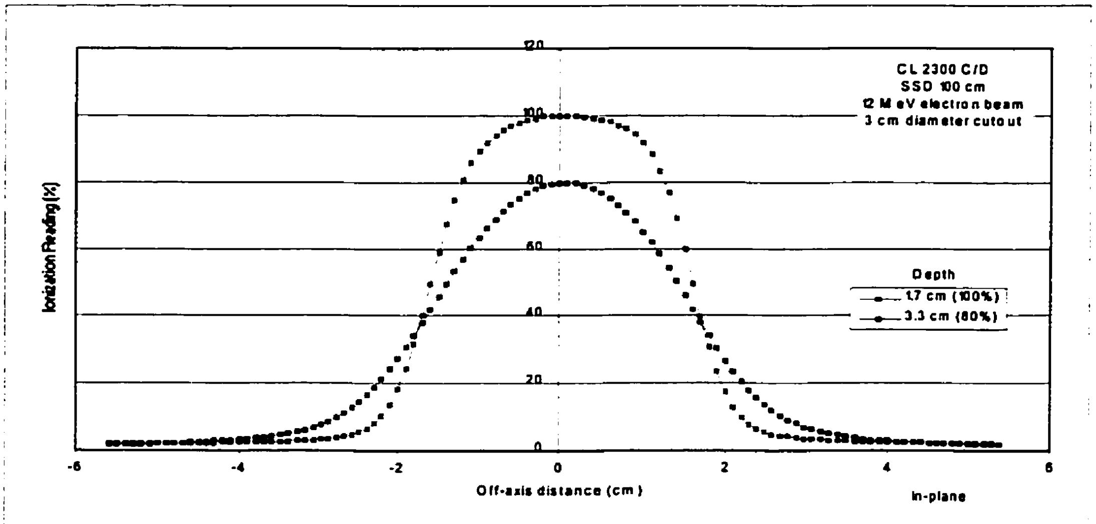

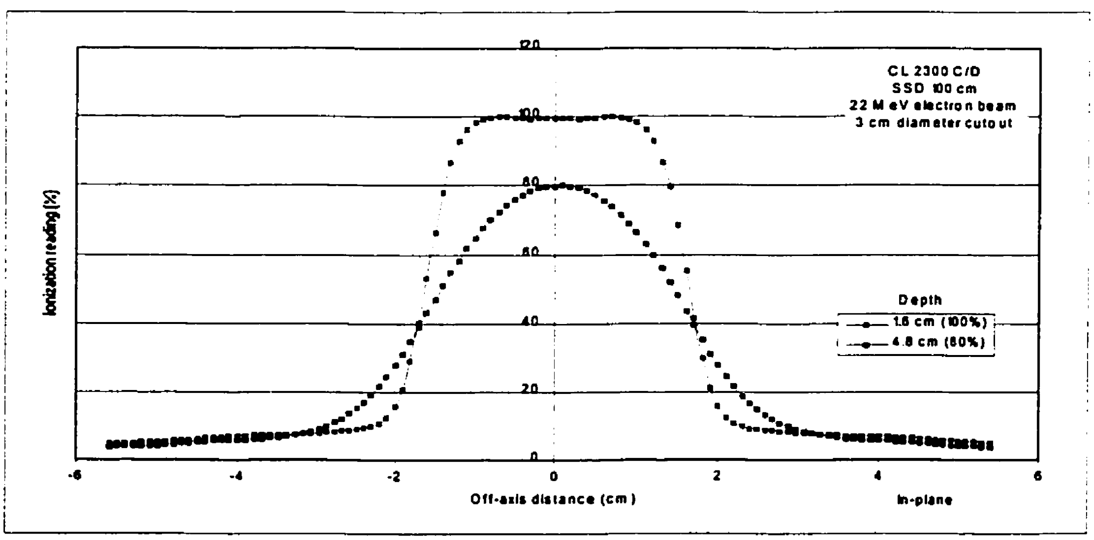

Figures A.13-15: Profiles measured with a 3 cm diameter cutout for various electron energy beams on a CL 2300 C/D.

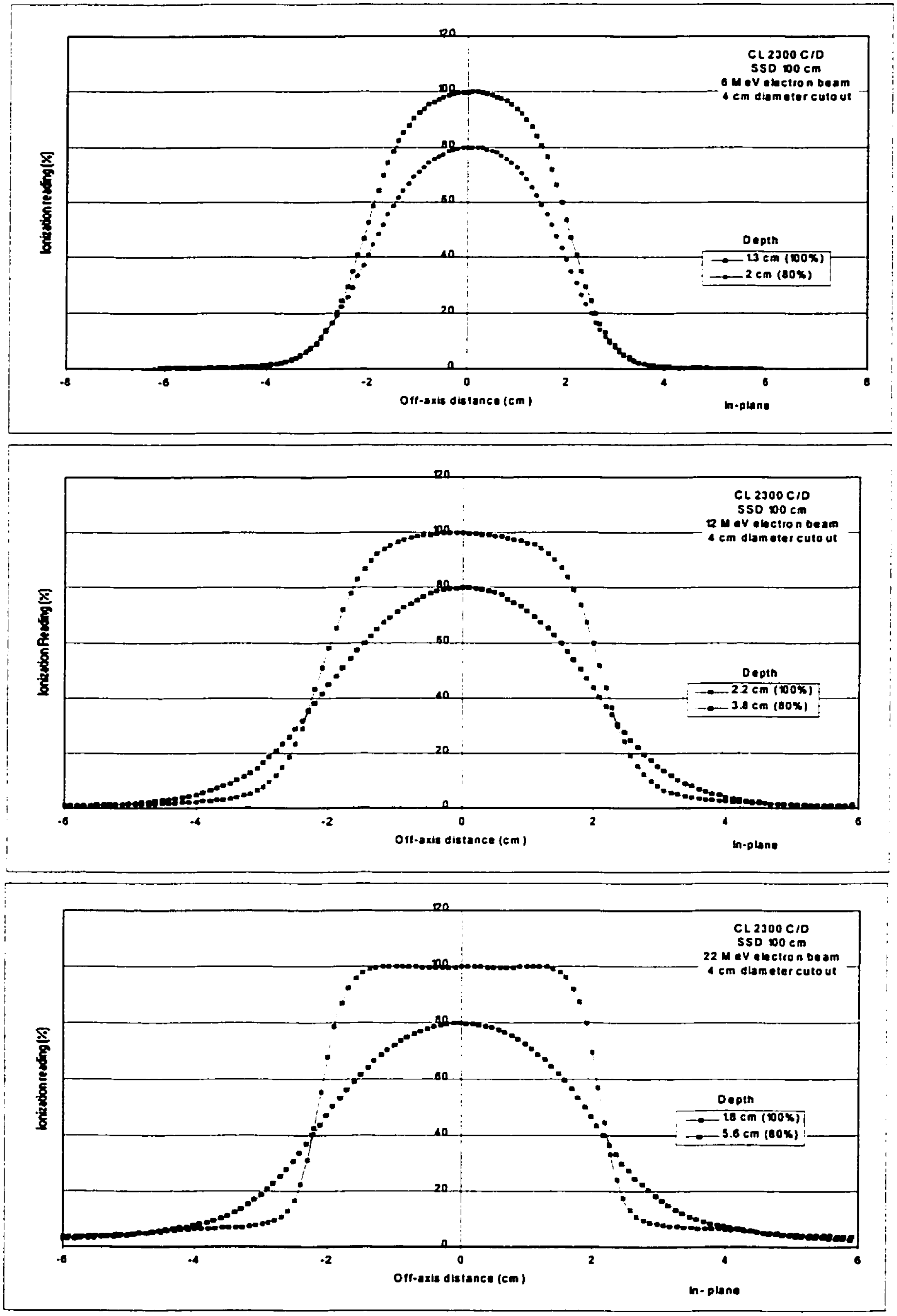

Figures A.16-18: Profiles measured with a 4 cm diameter cutout for various electron energy beams on a CL 2300 C/D.

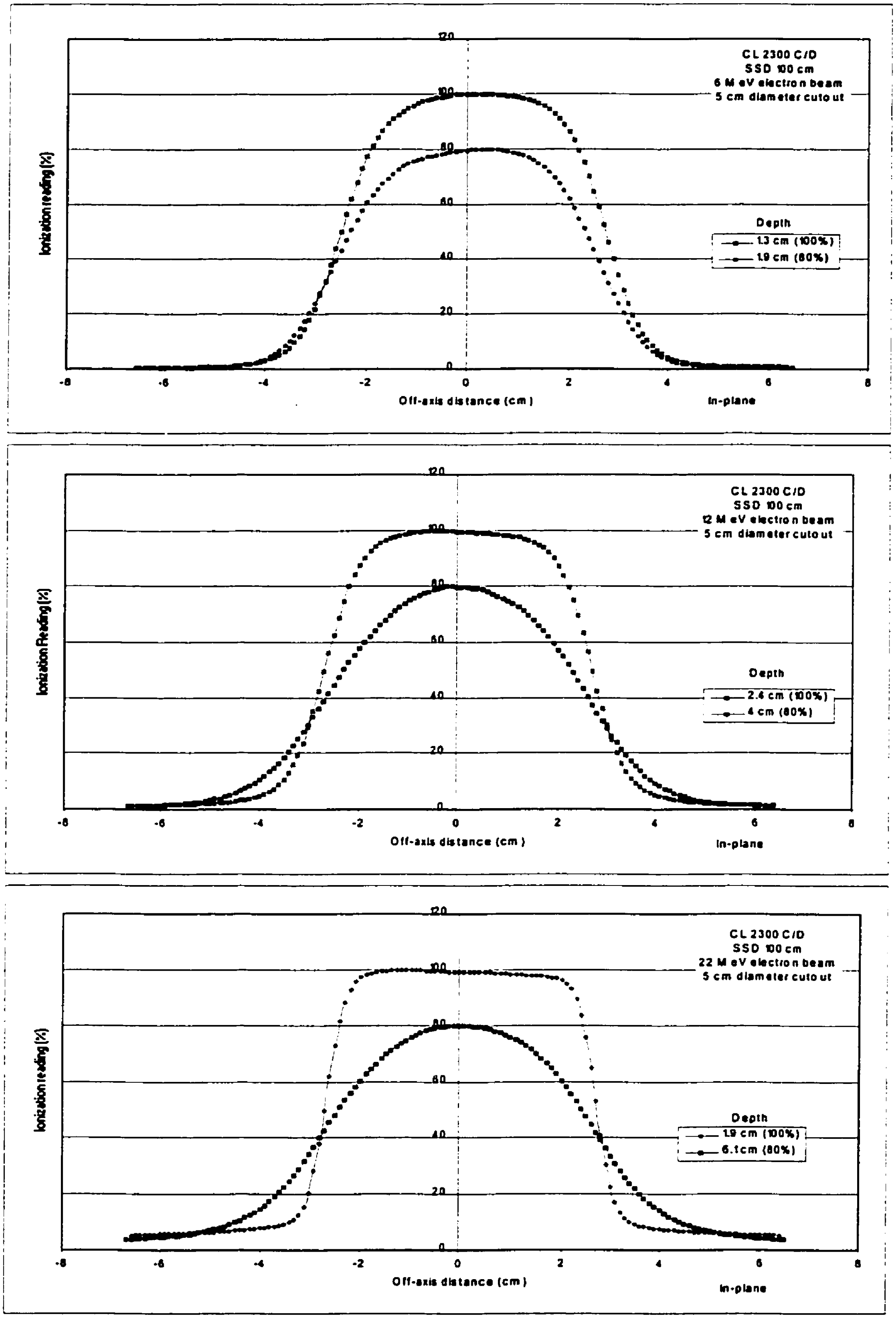

Figures A.19-21: Profiles measured with a 5 cm diameter cutout for various electron energy beams on a CL 2300 C/D.

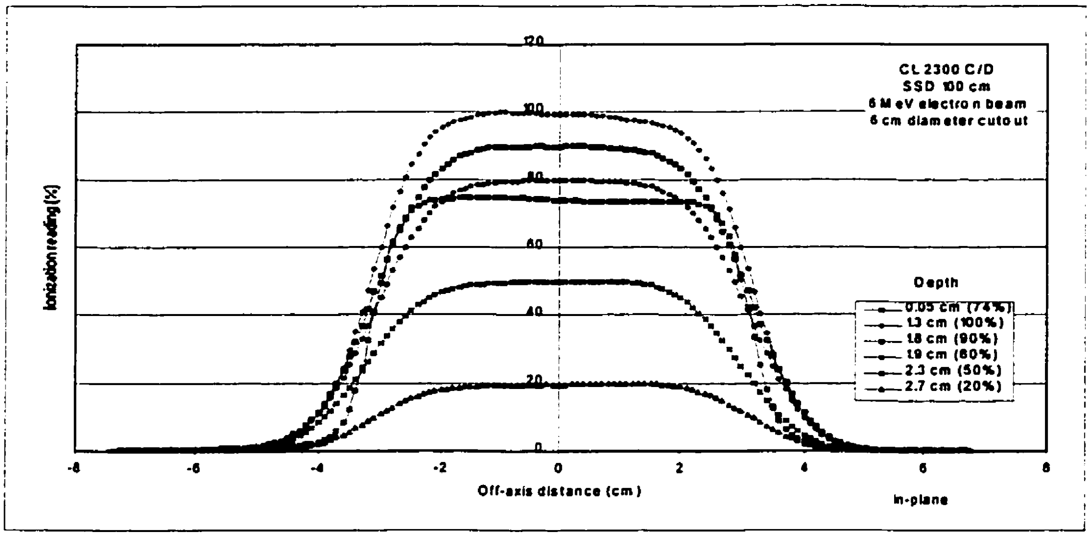

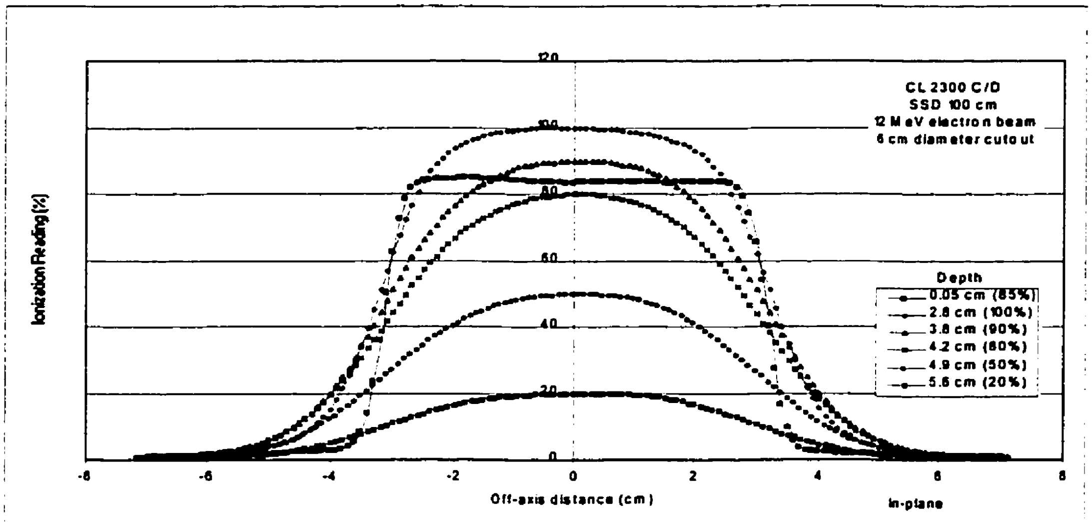

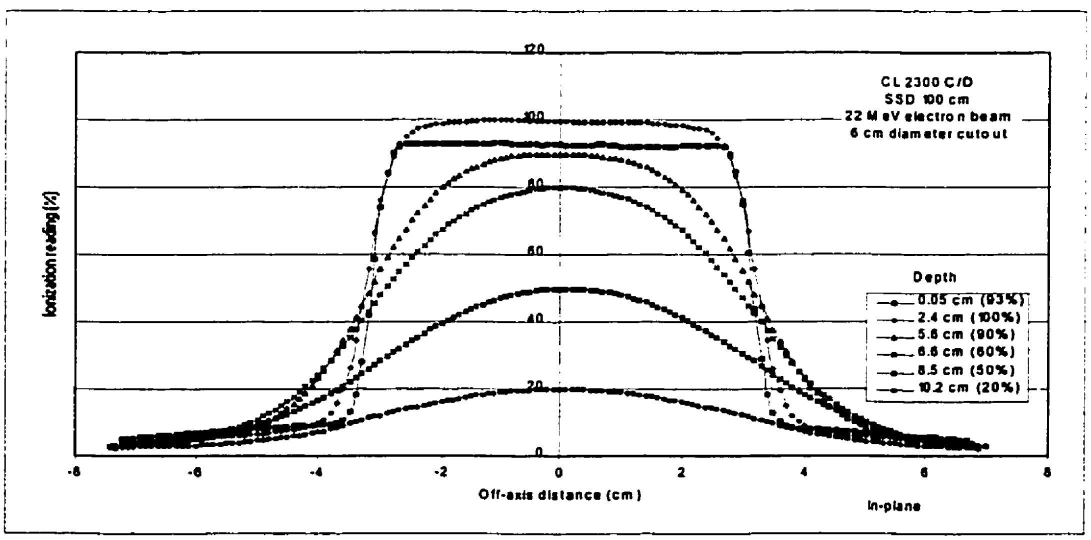

Figures A.22-24: Profiles measured with a 6 cm diameter cutout for various electron energy beams on a CL 2300 C/D.

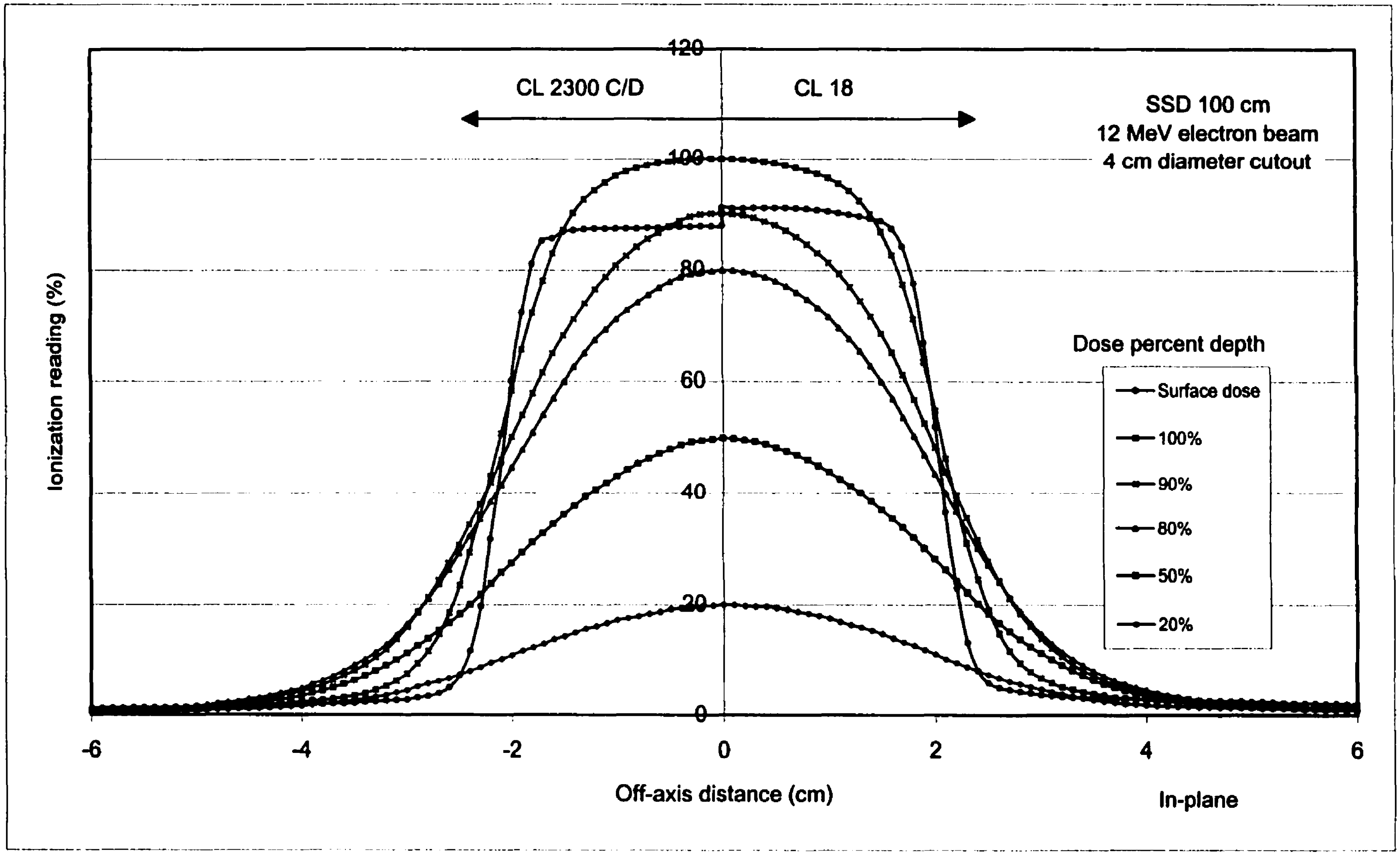

Figure A.25: A comparison between the profiles measured with the 12 MeV electron beam on a CL 2300 C/D and a CL 18 using a 4 cm diameter cutout.

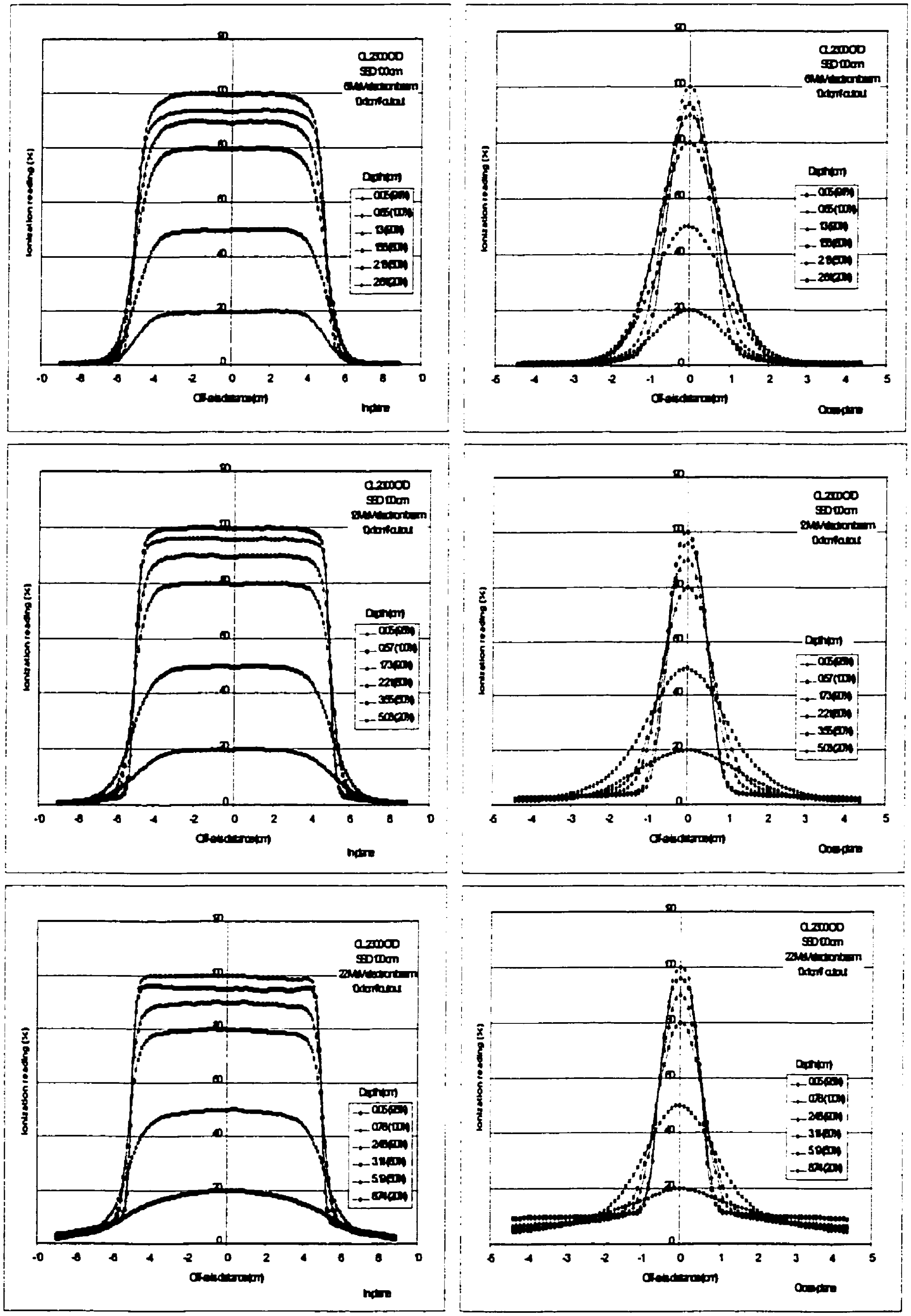

Figures A.26-31: Profiles measured with a 10x1 cm^2 cutout for various electron energy beams on a CL 2300 C/D.

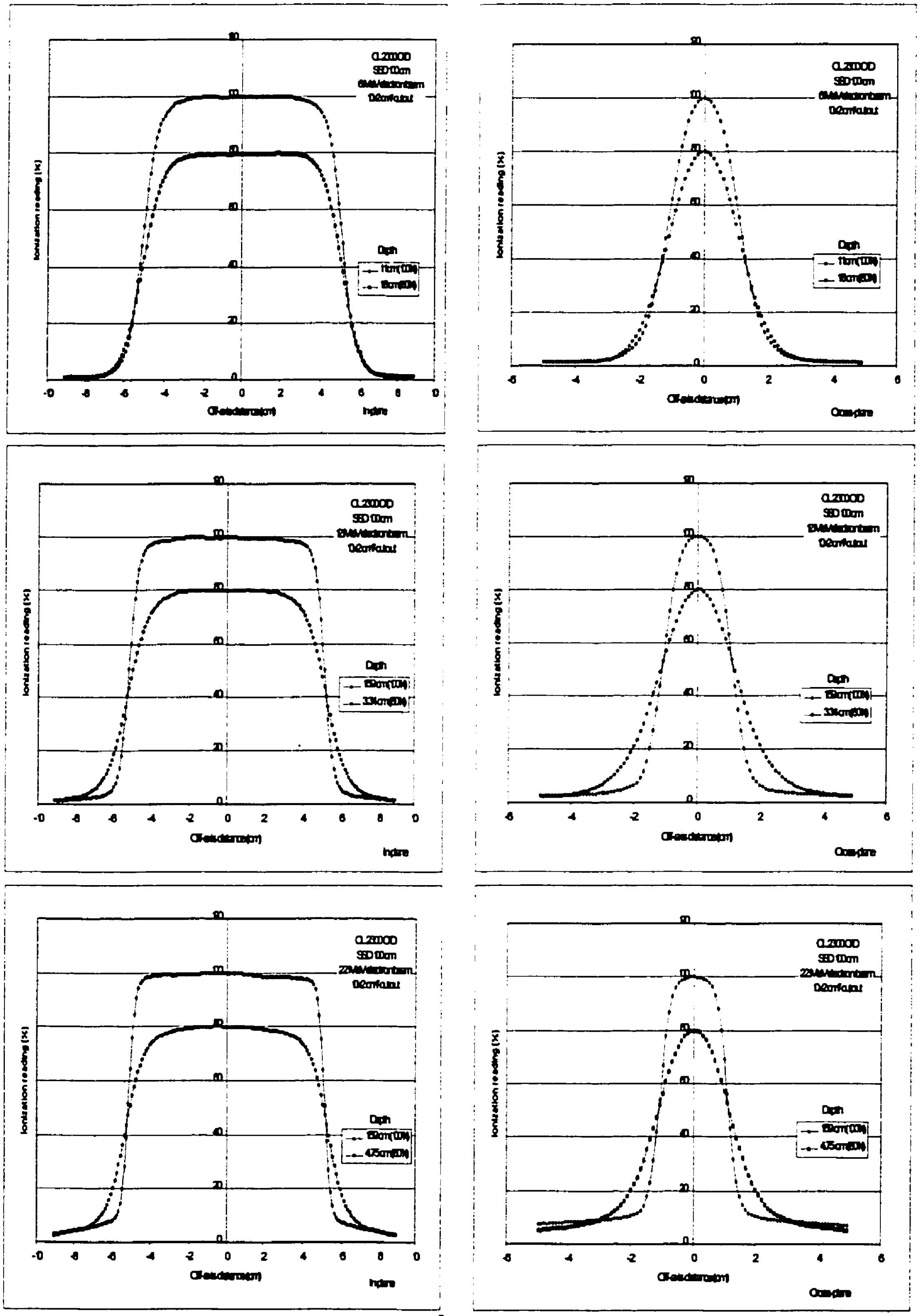

Figures A.32-37: Profiles measured with a 10x2 cm^2 cutout for various electron energy beams on a CL 2300 C/D.

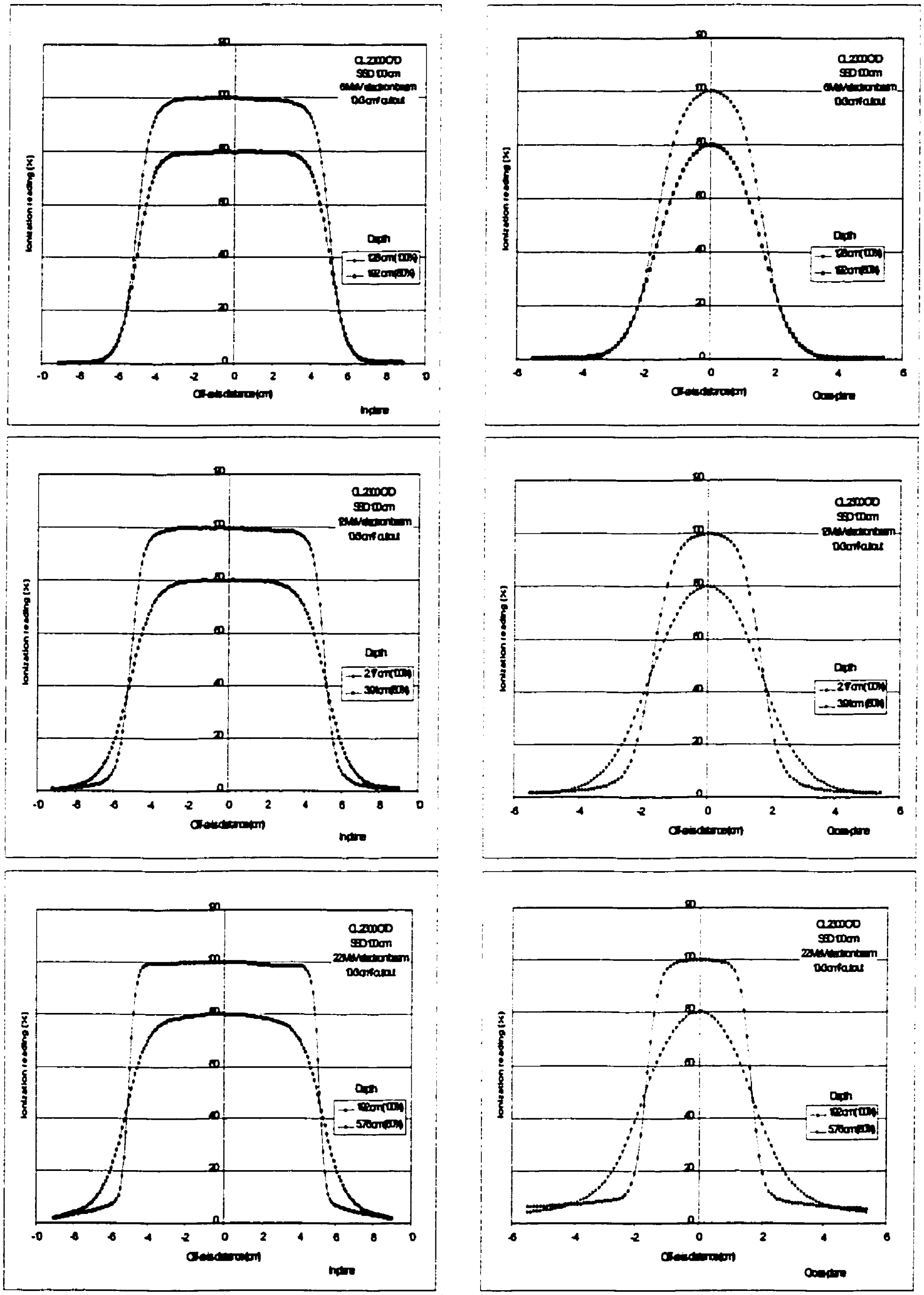

Figures A. 38-43: Profiles measured with a 10x3 cm^2 cutout for various electron energy beams on a CL 2300 C/D.

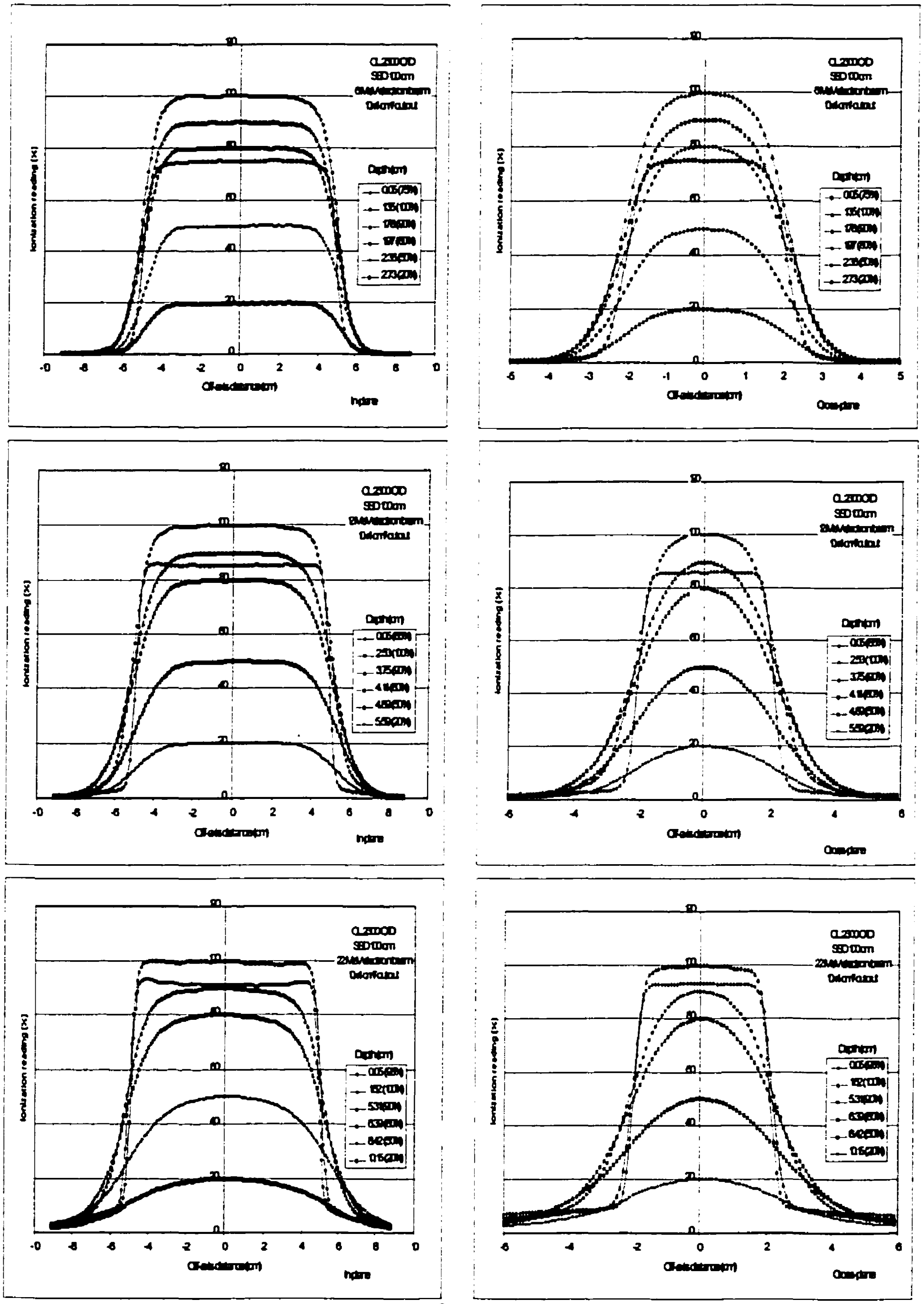

Figures A.44-49: Profiles measured with a 10x4 cm^2 cutout for various electron energy beams on a CL 2300 C/D.

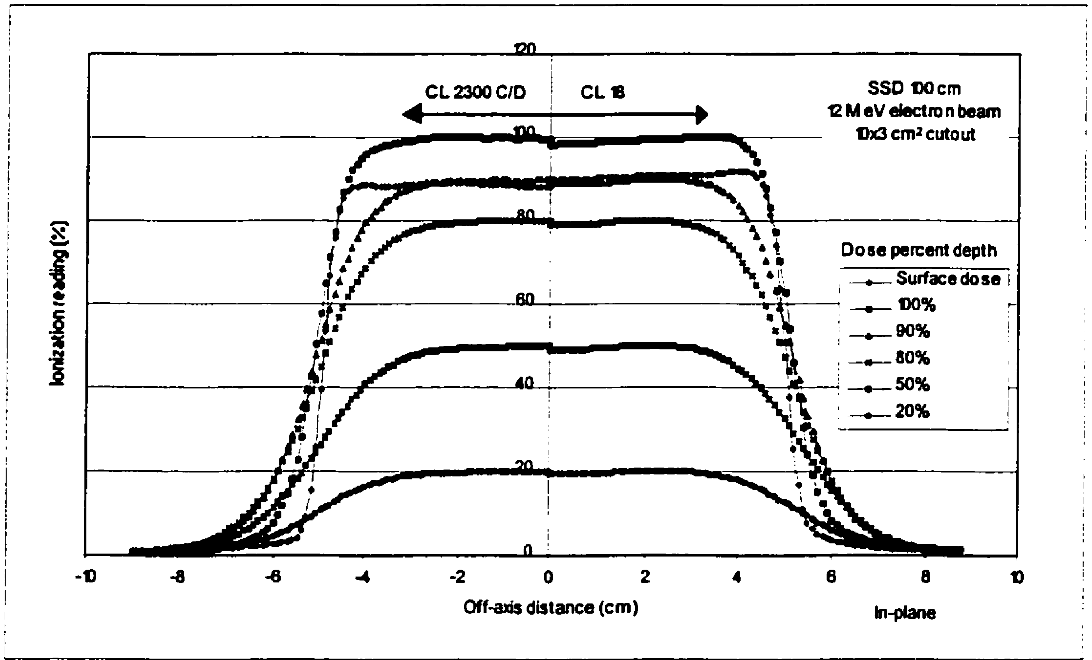

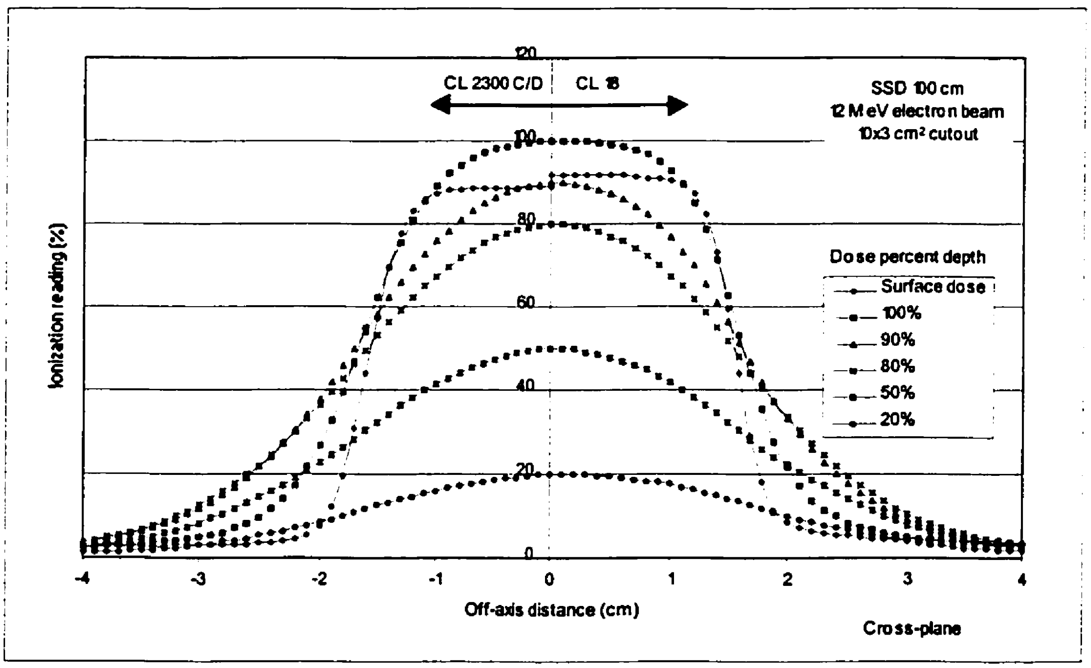

Figures A.50-51: A comparison between the profiles measured with the 12 MeV electron beam on a CL 2300 C/D and a Cl 18 using a 10x3 cm^2 cutout.

BIBLIOGRAPHY

Aget, H. & Rosenwald, J., "Polarity effect for various ionization chambers with multiple irradiation conditions in electron beams", Med. Phys. 18, 67-72 (1991)................p. 10

Almond, P.R., Biggs, P.J., Coursey, B.M., Hanson, W.F., Huq, M.S., Nath, R. & Rogers, D.W.O., "AAPM's TG-51 protocol for clinical reference dosimetry of high-energy photon and electron beams", Med. Phys. 26, 1847-1870 (1999)..........................p. 7

American Association of Physicists in Medicine (AAPM), RTC Task Group 21, "A protocol for the determination of absorbed dose from high energy photon and electron beams", Med. Phys. 10, 741-771 (1983)...................................p. 8, 10, 28-29, 33

Attix, F.H., Introduction to Radiological Physics and Radiation Dosimetry, John Wiley and Sons, Inc., New York, U.S.A. (1986)...p. 4, 9-10, 34

Biggs, P.J., Boyer, A.L. & Doppke, K.P., "Electron dosimetry of irregular fields on the Clinac 18", Int. J. Radiation Oncology, Biol. Phys. 5, 433-440 (1978)..................p. 53

Bruinvis, I.A.D., van Amstel, A., Elevelt, A.J. & van der Laarse, R., "Calculation of electron beam dose distributions for arbitrarily shaped fields", Phys. Med. Biol. 28, 667-683 (1983)..p. 59

Bureau of Vital Statistics; available from http://www.hss.state.ak.us/dph/bvs/bvs_home.htm. ; Internet..p. 1

Coia, L.R., Hanks, G.E., Martz, K., Steinfield, A., Diamond, J.J. & Kramer, S., "Practice patterns of palliative care for the United States 1984-1985", Int. J. Radiat. Oncol. Biol. Phys. 14, 261-1269 (1988)...p. 1

Constantinou, C., Attix, F.H. & Paliwal, B.R., "A solid phantom material for radiotherapy x-ray and γ-ray beam calibrations", Med. Phys. 9, 436 (1982)...........p. 34

Constantinou, C. Phone interview by Marina Olivares, 2000, Montreal, PQ............p. 35

Cygler, J., Li, X.A., Ding, G.X. & Lawrence, E., "Practical approach to electron beam dosimetry at extended SSD", Phys. Med. Biol. 42, 1505-1514 (1997)...................p. 47

Dutreix, A. & Briot, E., "The development of a pencil-beam algorithm for clinical use at the Institut Gustave Roussy", in The computation of dose distributions in electron beam radiotherapy, edited by A.E. Nahum. Umea University Press, Sweden (1985).........p. 59

Dutreix, J. & Dutreix, A., "Film dosimetry of high energy electrons", Ann. N.Y. Acad. Sci. 161, 33-43 (1969)..p. 40

Farmer, F.T., "A substandard x-ray dose-meter", Br. J. Radiol. 28, 304 (1955).........p. 33

Gelinas, D., *Commissioning a dynamic multileaf collimator on a linear accelerator*, M.Sc. Thesis, McGill University, Montreal, Canada, 1999...............................p. 33

Gerbi, B.J. & Khan, F.M., "The polarity effect for commercially available plane-parallel ionization chambers", Med. Phys. 14, 210-215 (1987)...................................p. 10

Gunn, S.R., "Radiometric calorimetry: a review", Nucl. Inst. Methods 20, 1 (1964)...p. 27

Gunn, S.R., "Radiometric calorimetry: a review", Nucl. Inst. Methods 85, 285 (1970)...p. 27

Gunn, S.R., "Radiometric calorimetry: a review", Nucl. Inst. Methods 135, 251 (1976)...p. 27

Hogstrom, K.R., "Clinical electron beam dosimetry: basic dosimetric data," in Advances in Radiation Oncology Physics, Dosimetry, Treatment Planning, and Brachytherapy, AAPM Monograph No. 19, edited by J.A. Purdy. American Institute of Physics, New York, NY (1992)..p. 47

Hogstrom, K.R., Mills, M.D. & Almond, P.R., "Electron beam dose calculations", Phys. Med. Biol. 26, 445-459 (1981)..p. 56

International Commission on Radiation Units and Measurements (ICRU), Radiation Dosimetry: Electrons with Initial Energies Between 1 and 50 MeV, ICRU Report 21, Bethesda, Maryland (1972)..p. 6, 49

International Commission on Radiation Units and Measurements (ICRU), Radiation Dosimetry: Electron Beams with Energies Between 1 and 50 MeV, ICRU Report 35, Bethesda, Maryland (1984)...p. 7, 28, 31-32

Johns, H.E. & Cunningham, J.R., The Physics of Radiology, 4th edition, Charles C. Thomas, Springfield, Illinois, U.S.A. (1983)..p. 20

Kapur, A., Ma, C-M., Mok, E.C., Findley, D.O. & Boyer, A.L., "Monte Carlo calculations of electron beam output factors for a medical linear accelerator", Phys. Med. Biol. 43, 3479-3494 (1998)..p. 53-54, 59

Karzmark, C.J., "Advances in linear accelerator design for radiotherapy", Med. Phys. 11, 105 (1984)..p. 15

Khan, F.M., The Physics of Radiation Therapy, 2nd edition, Williams & Wilkins, Baltimore, Maryland, U.S.A. (1994).. p. 1, 26, 30, 32

Khan, F.M., Doppke, K.P., Hogstrom, K.R., Kutcher, G.J., Nath, R., Prasad, S.C., Purdy, J.A., Rozenfield, M. & Werner, B.L., "Clinical electron-beam dosimetry: Report of AAPM Radiation Therapy Committee Task Group No. 25", Med Phys. 18, 73-109 (1991)..p. 7, 8, 10, 22-24, 30-31, 35, 37-38, 40, 44, 47, 54

Klevenhagen, S.C., Physics and Dosimetry of Therapy Electron Beams, Medical Physics Publishing, Madison, Wisconsin, U.S.A. (1993)..p. 7, 40-41, 56

Laughlin, J.S. & Genna, S., "Calorimetry," in Radiation Dosimetry, edited by F.H. Attix & W.C. Roesch. Academic Press, New York, NY (1967)..p. 27

Mattsson, L.O., Johansson, K.A. & Svensson, H., "Calibration and use of plane-parallel ionization chambers for the determination of absorbed dose in electron beams", Acta Radiol. Oncol. 20, 385-399 (1981)..p. 10

McGhee, P., Chu, T. & Dunscombe, P., "The characterization of clinical electron beams of arbitrary shape in water", Proceedings of the Canadian Organization of Medical Physicists 42nd Annual Meeting, 107-110 (1996)..p. 47

McParland, B.J., "A method of calculating the output factors of arbitrarily shaped electron fields", Med. Phys. 16, 88-93 (1989)..p. 53

Meyer, J.A., Palta, J.R. & Hogstrom, K.R., "Demonstration of relatively new electron dosimetry measurement techniques on the Mevatron 80", Med. Phys. 11, 670-677 (1984)..p. 47

Mills, M.D., Hogstrom, K.R. & Almond, P.R., "Prediction of electron beam output factors", Med. Phys. 9, 60-68 (1982)..p. 53

Mills, M.D., Hogstrom, K.R. & Fields, R.S., "Determination of electron beam output factors for a 20 MeV linear accelerator", Med. Phys. 12, 473 (1985).....p. 25, 53, 56, 58-9

Niroomand-Rad, A., Gillin, M.T., Kline, R.W. & Grimm, D.F., "Film dosimetry of small electron beams for routine radiotherapy planning", Med. Phys. 13, 416-421 (1986).........p. 47, 53-55

Nordic Association of Clinical Physics (NACP), "Electron beams with mean energies at the phantom surface below 15 MeV", Acta Radiol. Oncol. Rad. Phys. 20, 402-415 (1981).........p. 7

Perez, C.A. & Brady, L.W., Principle and practice of radiation oncology, JP Liddicoat, Philadelphia, U.S.A. (1987).........p. 1

Podgorsak, E.B., Metcalfe, P. & Van Dyk, J., "Medical Accelerators," in The Modern Technology of Radiation Oncology, edited by J. Van Dyk. Medical Physics Publishing, Madison, WI (1999).........p. 2, 15-17, 21

Pruitt, J.S., Calibration of beta-particle-emitting ophthalmic applicators, Natl. Bur. Stand. (U.S.), Spec. Publ. 250-9, U.S. Government Printing Office, Washington, D.C. (1987).........p. 10

Rogers, D.W.O. & Bielajew, A.F., "Differences in electron depth-dose curves calculated with EGS and ETRAN and improved energy-range relationships", Med. Phys. 13, 687-691 (1986).........p. 8

Rogers, D.W.O., Faddegon, B.A., Ding, G.X., Ma, C-M, We, J. & Mackie, T.R., "BEAM: a Monte Carlo code to simulate radiotherapy treatment units", Med. Phys. 22, 503-524 (1995).........p. 59

Sharma, S.C., Wilson, D.L. & Jose, B. "Dosimetry of small fields for Therac 20 electron beams", Med. Phys. 11, 697-702 (1984).........p. 47, 53

Shiu, A.S., Otte, V.A. & Hogstrom, K.R., "Measurement of dose distribution using film in therapeutic electron beams", Med. Phys.16, 911-925 (1989).........p. 55

Wellhöfer Dosimetrie, Film Densitometer WP 102 Operating Instructions, Schwarzenbruk, Germany. (1992).........p. 39

Zhang, G.G., Rogers, D.W.O., Cygler, J.E. & Mackie, T.R., "Effects of changes in stopping-power ratios with field size on electron beam relative output factors", Med. Phys. 25, 1711-1716 (1998).........p. 47

Zhang, G.G., Rogers, D.W.O, Cygler, J.E.& Mackie, T.R., "Monte Carlo investigation of electron beam output factors versus size of square cutout", Med. Phys. 26, 743-750 (1999).........p. 53